Jana Joeressen, BSc

Influence of process parameters on the mechanical resistance of additively manufactured hybrid joints

MASTER’S THESIS

to achieve the university degree of
Diplom-Ingenieurin

Master's degree programme:
Advanced Materials Science

submitted to

Graz University of Technology

Supervisor

Univ.-Prof. Dr.-Ing. Sergio Amancio
Institute of Materials Science, Joining and Forming
Co-supervisor: Carlos Belei, Bach. Mestr.

Graz, June 2021

AFFIDAVIT

I declare that I have authored this thesis independently, that I have not used other than the declared sources/resources, and that I have explicitly indicated all material which has been quoted either literally or by content from the sources used. The text document uploaded to TUGRAZonline is identical to the present master's thesis.

Date, Signature

Acknowledgements

First of all, I would like to express my gratitude to my academic adviser Prof. Dr. Sergio Amancio for introducing me to the topic and for his constructive feedback in the process of writing this master thesis.

I would also like to thank my scientific adviser Carlos Belei, Bach. Mestr. for supporting me the whole way through this project. His door was always open when I had any questions. Thank you for the guidance and the input!

Furthermore, thank you to all the staff of the IMAT institute for always being helpful.

Thank you to my parents Olaf and Stefanie Joeressen for always being there for me and supporting me in everything I do!

Abstract

AddJoining is a novel technology to produce layered metal-polymer hybrid structures by combining additive manufacturing and joining process principles. In this study, the influence of process parameters on the mechanical performance of addjoined metal-polymer hybrid joints was investigated. As a substrate, sandblasted Ti-6Al-4V titanium plates were used. For the coating layer (i.e. the one directly printed onto the substrate), unreinforced polyamide (PA) was used and for the composite part (i.e. all other subsequently printed layers), a reinforced technical grade polyamide with 15 wt.% of short carbon fibres (PA-CF).

The study was split into two sections: the first one dedicated to the composite part optimisation (PA-CF) and the second to the coating layer optimisation (PA). In both sections, the goal was to optimise the printing parameters in order to maximize the mechanical performance of the samples and the investigated printing parameters were printing speed, nozzle temperature, heated bed temperature and layer height.

In the composite part optimisation, a design of experiment (DoE) with a 2k-full factorial design was carried out. After printing, the ultimate tensile strength (UTS) of the samples was measured. Then, using the condition which led to the highest UTS, the influence of the printing bed material on the UTS was evaluated, as well. In the coating layer optimisation, a one-factor-at-a-time (OFAT) approach was used. For the mechanical testing, i.e. the measurement of the ultimate lap-shear strength (ULSS), dimensions and other relevant details were based on the conventional single-lap shear test for adhesives.

For both experimental sections, the influence of each process parameter on the mechanical performance of manufactured samples was determined by Analysis of Variance (ANOVA). Furthermore, an IR camera was used for a thermographic analysis of the print process, while microstructural and fractography analysis were carried out using optical as well as electron microscopy.

In the composite part optimisation, a UTS value of 117.1 ± 6.1 MPa was achieved when using the optimised parameter set, a 13.5 % gain over the value provided by the filament manufacturer. The layer height has the strongest influence on the performance. While the printing speed did not have a significant influence, a higher bed temperature as well as a higher nozzle temperature also lead to an increased UTS. In the investigation of the printing bed material, the UTS of the samples printed on glass was 41 % higher than of those printed on aluminium.

In the coating layer optimisation, a ULSS of 17.8 ± 0.7 MPa was achieved when applying the optimised parameter set. The coating layer height as well as the printing speed were considered statistically significant according to the ANOVA analysis. A necessary minimum bed temperature of 140°C was found in order to produce testable samples. Above that value, no further statistically significant variation was observed. The failure types could be related to the coating layer height, while a clear tendency of higher ULSS for higher extrusion rates was identified.

Kurzfassung

AddJoining ist eine neuartige Technologie zur Herstellung von geschichteten Metall-Polymer-Hybridstrukturen durch Kombination von Prinzipien der additiven Fertigung und der Fügetechnik. In dieser Studie wurde der Einfluss von Prozessparametern auf die mechanischen Eigenschaften von Metall-Polymer-Hybridverbindungen untersucht. Als Träger wurden sandgestrahlte Ti-6Al-4V-Titanplatten verwendet. Für die ”coating layer” (d. h. die direkt auf den Träger gedruckte Schicht) wurde unverstärktes Polyamid-6 (PA) und für den ”composite part” (d. h. alle anderen nachfolgend gedruckten Schichten) ein verstärktes Polyamid-6 mit 15 % kurzen Kohlenstofffasern (PA-CF) verwendet.

Die Studie wurde in zwei Abschnitte unterteilt: im ersten steht der ”composite part” (PA-CF) im Fokus und im zweiten die ”coating layer” (PA). In beiden Abschnitten bestand das Ziel darin, die Druckparameter zu optimieren, um die mechanischen Festigkeit der Proben zu maximieren. Die untersuchten Druckparameter waren Druckgeschwindigkeit, Düsentemperatur, Heizbetttemperatur und Schichthöhe.

In der ”composite part optimisation” wurde ein Design of experiment (DoE) mit einem 2k-full factorial design durchgeführt. Nach dem Drucken wurde die Zugfestigkeit (UTS) der Proben gemessen. Dann wurde unter Verwendung der Parameter, die zur höchsten UTS führten, auch der Einfluss des Druckbettmaterials auf die UTS bewertet. Bei der Optimierung der ”coating layer” wurde ein OFAT-Ansatz (One-Factor-at-a-Time) verwendet. Für die mechanische Prüfung, d. h. die Messung der maximalen Zugscherfestigkeit (ULSS), basierte die Geometrie und andere relevante Details auf dem herkömmlichen Zugscherversuch für Klebstoffe.

Für beide experimentellen Abschnitte wurde der Einfluss jedes Prozessparameters auf die mechanische Festigkeit der hergestellten Proben durch Analysis of Variance (ANOVA) bestimmt. Darüber hinaus wurde eine IR-Kamera zur thermografischen Analyse des Druckprozesses verwendet. Zur Mikrostruktur- und Fraktografieanalyse wurden sowohl ein optisches Mikroskop als auch ein Elektronenmikroskop verwendet.

In der ”composite part optimisation” wurde bei Verwendung des optimierten Parametersatzes ein UTS-Wert von 117.1 ± 6.1 MPa erreicht, was einer Steigerung von 13,5 % gegenüber dem vom Filamenthersteller bereitgestellten Wert entspricht. Die Schichthöhe hat den stärksten Einfluss auf die Festigkeit. Während die Druckgeschwindigkeit keinen signifikanten Einfluss hatte, führten eine höhere Heizbetttemperatur sowie eine höhere Düsentemperatur auch zu einer erhöhten UTS. Bei der Untersuchung des Druckbettmaterials war die UTS der auf Glas gedruckten Proben um 41 % höher als die der auf Aluminium gedruckten.

In der ”coating layer optimisation” wurde bei Anwendung des optimierten Parametersatzes eine ULSS von 17.8 ± 0.7 MPa erreicht. Die Schichthöhe der ”coating layer” sowie die Druckgeschwindigkeit wurden gemäß der ANOVA-Analyse als statistisch signifikant angesehen. Eine notwendige Mindestheizbetttemperatur von 140°C wurde gefunden, um testbare Proben herzustellen. Oberhalb dieses Wertes wurde keine weitere Änderung der statistischen Signifikanz beobachtet. Die Fehlertypen konnten mit der Höhe der ”coating layer” in Beziehung gesetzt werden, während eine deutliche Tendenz einer höheren ULSS für höhere Extrusionsraten festgestellt wurde.

List of abbreviations

A-M	Adhesive failure between the metallic substrate and the coating layer
A-P	Adhesive failure between the coating layer and the composite part
ABS	Acrylonitrile Butadiene Styrene
ANOVA	Analysis of Variance
ASTM	American Society for Testing and Materials
bcc	body centred cubic
CF	Carbon fibre
CLO	Coating layer optimization
CPO	Composite part optimization
DaB	Deformation at Break
DoE	Design of Experiment
DSC	Differential scanning calorimetry
FFF	Fused-Filament Fabrication
GF	Glass fibre
hcp	hexagonal close packed
IR	Infrared
NT	Net-tension failure
OFAT	One-factor-at-a-time
PA	Polyamide
PEEK	Polyether ether ketone
PEI	Polyethyleneimine
PI	Polyimide
SaB	Strain at Break
SEM	Scanning electron microscopy
ULSF	Ultimate Lap Shear Force
ULSS	Ultimate Lap Shear Strength
UTS	Ultimate tensile strength

Contents

1 Introduction

As pointed out by the United Nations [1], one of the world's largest and most important challenges of our time is climate change due to global warming. This is directly linked to the increasing amount of greenhouse gases in the atmosphere, of which CO_2 is the most abundant [1]. One of the largest CO_2 emission sources is the transport sector (i.e. vehicles, ships, airplanes) where the amount of emitted CO_2 is proportional to the amount of consumed fuel [2]. Since the fuel consumption increases with the weight of the vehicle, reducing the weight is one of the most efficient ways to lower the CO_2 emissions [2].

As introduced and described by Falck *et al.* [3, 4], AddJoining is a novel technology to produce layered metal-polymer hybrid structures by combining additive manufacturing and joining process principles. To produce AddJoining hybrid parts, the metal part is secured in a slot on the heated bed of a 3D-printer. Then, the polymer is printed on the metal using fused-filament fabrication (FFF). Showing a large potential regarding complex geometries and efficient joining of different materials, the Addjoining is especially attractive for the aerospace and automotive industries, where lightweight structures are needed in an effort to reduce CO_2-emissions. Moreover, AddJoining works with thermoplastic materials, which are repairable and recyclable polymers. As a result, the new process has the potential to simultaneously increase sustainability and support the efforts towards a future circular economy in lightweight manufacturing [3, 4].

However, there are still several knowledge gaps concerning the AddJoining process, such as the influence of certain process parameters on the mechanical performance of the manufactured part. In order to fill those gaps, the influence of printing speed, nozzle temperature, bed temperature and layer height was evaluated for a new material combination in this thesis. Additionally, the polymer was printed directly onto the metal plate without using pre-application of liquid coating layers in the metal (e.g. as the use of high-concentrated polymer solutions to form the coating layer, see [4]) or machine adaptations (such as adding a closed insulating chamber, see [5]), which represented an improvement over the state of the art for the technique.

2 Objectives and Outline

2.1 Objectives

The objective of this work was to investigate the influence of different AddJoining process parameters on the resulting quasi-static mechanical performance of hybrid joints made of a titanium substrate (Ti-6Al-4V) and a technical grade polyamide reinforced with 15 wt.% of short carbon fibres (PA-CF) and to optimise them in order to obtain strong single-lap joints.

2.2 Outline

Ti-6Al-4V titanium plates were used as the metallic substrate. For the Fused Filament Fabrication (FFF) of the coating layer (i.e. the one directly printed onto the metal), an unreinforced polyamide6/66 copolymer (PA) filament was used. For the composite part, a technical grade polyamide filament reinforced with 15 wt.% of short carbon fibres (PA-CF) was used.

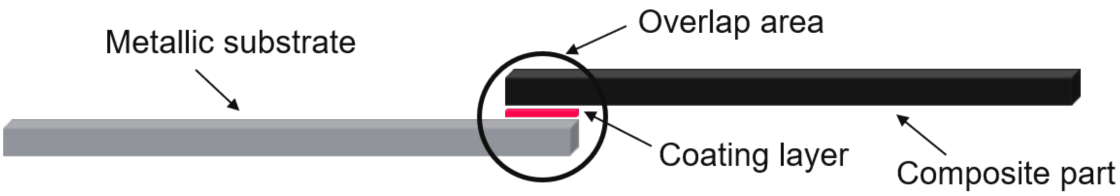

Figure 1: Nomenclature of the tested AddJoining samples. The black circle highlights the overlap area.

As the process at this point is discontinuous, the experimental part was split into two. One was dedicated to optimising the printing parameters for the PA-CF (composite part optimisation) and the other to optimising them for the coating layer (PA). The investigated printing parameters for both experimental parts were printing speed, nozzle temperature, heated bed temperature and layer height.

For the composite part optimisation (CPO), a design of experiment with a 2k-full factorial design was carried out. After printing, the ultimate tensile strength (UTS) of the samples was measured, the obtained values were statistically evaluated and thereby the optimal parameter set was determined.

For the coating layer optimisation, a one-factor-at-a-time (OFAT) approach was used to optimise the parameters regarding the ultimate lap-shear strength (ULSS) of the single-lap joints. The same process parameters as in the CPO were evaluated, but only during the printing of the coating layer (PA). The rest of a given specimen was then printed with PA-CF, using the optimised parameter set obtained in the previous experimental section (CPO). The mechanical testing was carried out using dimensions and other relevant details based on the conventional single-lap shear test standard for adhesives.

After testing, the experimental results were analysed by applying Analysis of Variance (ANOVA) to determine the statistical significance of each process parameter. To understand the effect of different heat-cooling cycles on the printed parts, the temperatures during the process were measured with an IR camera for selected printing conditions. The sample interfaces were characterized using optical microscopy and scanning electron microscopy (SEM) was used for the analysis of the fracture surfaces.

3 Literature Review

In this chapter, the theoretical background is discussed. First, the AddJoining process is described and already existing studies on material properties and influencing parameters in AddJoining are reviewed. Then, a review of publications regarding the temperature distribution and its role in fused filament fabrication follows. Furthermore, the main bonding mechanisms, the necessary surface preparation of the metal plate and the lap shear testing method are explained. Lastly, the characteristics of the used materials are presented.

3.1 AddJoining Process

AddJoining is a new technique to produce layered metal-polymer hybrid structures, introduced by Falck *et al.* in 2018 [3]. It combines polymer additive manufacturing and metal-polymer hybrid joining process principles [3]. Unlike conventional joining methods (e.g. adhesive bonding), AddJoining shows a large potential regarding complex geometries, efficient joining of different materials and lightweight structures. It is especially attractive for the aerospace industry where weight reduction is closely linked to reducing CO_2-emissions [3].

In Figure 2, the process is shown for a single-lap joint. First, the metallic substrate is secured in a slot on the platform of the 3D-printer (a) [3]. Then, the polymer is printed using Fused Filament Fabrication (FFF) principles, i.e. the filament is softened (in the case of amorphous thermoplastics) or melted (for semi-crystalline thermoplastics) within a heated copper block, and then deposited on the metallic substrate by extrusion through a heated nozzle, until a complete layer is formed (b) [3, 6]. After deposition, the material cools quickly and changes from its semi-liquid into a solid state while bonding with the neighbouring deposited roads. This first layer, which is called ”coating layer”, is especially important for the adhesion between the metallic substrate and the rest of the printed part. On top of the coating layer, printing is continued until the required thickness of the manufactured part is obtained [3]. During printing, it is possible to use different filaments for the different layers (e.g. reinforced and unreinforced polymers), which is important for manufacturing layered hybrid structures [3]. This also allows the selection of a different material for the coating layer than for the rest of the printed part. This enables one to use a polymer with lower viscosity for the coating layer, which facilitates material flow around surface irregularities present on the metallic substrate, possibly increasing adhesion between the metallic substrate and the printed part as a result. Afterwards, the now-joint structure is removed from the platform (c) and, if necessary, post-treatment (e.g. thermo-mechanical treatment) can be applied [3].

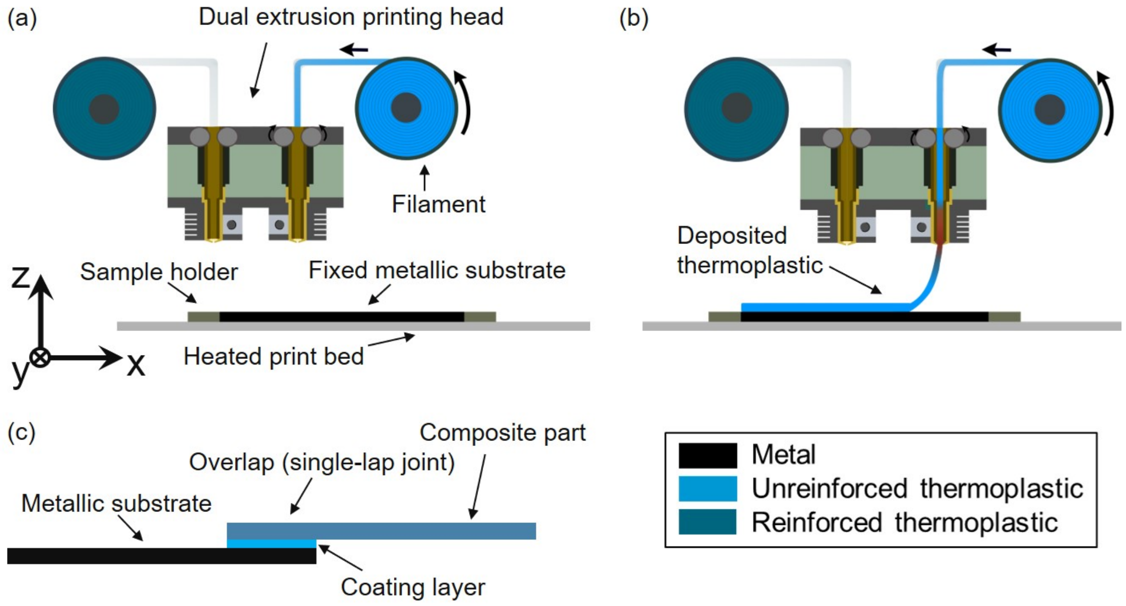

Figure 2: AddJoining process. Adapted from Reference [3].

3.1.1 Previous studies on influencing process parameters in AddJoining

After introducing the Addjoining technique, Falck *et al.* [3] also studied the mechanical properties as well as the microstructure obtained for a single-lap joint for two different material combinations. In both cases, Al 2024-T3 was used for the metal part, while for the polymer part, acrylonitrile butadiene styrene (ABS) was used in one part of the study and alternating layers of PA and carbon fibre reinforced PA in the other. The samples further differed in the process of applying the coating layer. While the ABS coating layer was not printed but laid up manually with an ABS-acetone solution, the PA coating layer was printed and then remelted with a hot plate to promote homogeneity. According to the authors, the analysis of the microstructure indicated a good contact and strong bond at both material interfaces. The absence of a visible bond line between the coating layer and the deposited polymer indicated the presence of intermolecular diffusion at this particular interface. Falck *et al.* [3] observed voids in the ABS case and assumed that their presence was ascribed to residual acetone that evaporated during the printing stage.

For comparison, the same material combinations were also adhesively bonded and tested in this study [3]. A comparison between addjoinined and adhesively bonded specimens in terms of mechanical performance is displayed in Table 1. All investigated samples showed a relatively low strain at break (SaB) and therefore brittle behaviour, as is common for adhesively bonded joints. However, the ultimate lap shear strength (ULSS) reached considerably higher values for the addjoined samples compared to the adhesively bonded ones [3].

Table 1: Ultimate lap shear strength (ULSS) and Strain at Break (SaB) of metal-polymer hybrid joints [3].

Material combination [Joining process]	ULSS [MPa]	SaB [%]
Al 2024-T3/ABS [AddJoining]	5.3 ± 0.3	1.5 ± 0.1
Al 2024-T3/ABS [Adhesive Bonding]	2.8 ± 0.2	0.6 ± 0.1
Al 2024-T3/PA/CF-PA [AddJoining]	21.9 ± 1.1	1.6 ± 0.1
Al 2024-T3/PA/CF-PA [Adhesive Bonding]	17.7 ± 0.9	1.4 ± 0.1
Al 5083/GFRP [State-of-the-art Adhesive Bonding]	8.3	-
$AlMg_3$/CF-PA6 [Induction Heating Bonding]	11	-

Moreover, Falck *et al.* [4] studied the influence of different process parameters on the mechanical behaviour of Al 2024-T3 - ABS hybrid single lap joints made by AddJoining and compared it with fully polymeric samples. Five parameters were varied in their study: the printing temperature, the road thickness, the deposition speed, the number of contours and the ABS coating concentration. Since the findings of Falck *et al.* [4] are relevant as a starting point for understanding the influence of the different parameters in AddJoining, the results of their study are summarized in the remaining paragraphs of this chapter.

The best mechanical and microstructural properties were obtained for the highest applied printing temperature of 280°C. Increasing the printing temperature from 230°C to 280°C led to smaller and fewer pores in the polymer. The void area decreased approximately 76 % from 1314 µm² to 314 µm². The bonding was stronger since the higher temperatures promoted chain diffusion and polymer entanglement between the layers. The amount of average pore volume size was reduced by almost 40 % from 230°C to 255°C and then remained constant when the printing temperature was further increased to 280°C [4].

An increasing deposition speed also led to a better mechanical performance. For a deposition speed of 20 mm/s, gaps between the roads were observed and the average surface roughness of the printed polymer was 302 µm. Increasing the deposition speed to 60 mm/s resulted in a smooth surface (70 µm) and a low concentration of pores in the volume edge. While the pore volume stayed constant for all samples, for higher deposition speeds, a large reduction of the number of pores was observed due to the short time for the road to consolidate before the next road was deposited. Thus, the road could stay softened which promoted intermolecular diffusion and caused a better interlayer bonding as well as less microvoids [4].

Furthermore, decreasing the road thickness from 0.3 mm to 0.1 mm led to a smaller surface roughness, better interlayer bonding and less pores. According to the authors, pores in between the layers may lead to stress concentration and starting points for crack formation. Therefore, the mechanical performance increased with decreasing road thickness [4].

A large ABS coating concentration (25 wt.%) and coating thickness increased the mechanical properties in the case of the Al 2024-T3/ABS hybrid joint. The authors suggested that this was due to the larger amount of mass (compared to thinner coating layers) that could be plastically deformed and lead to low shear and peel stresses. Increasing the coating concentration also reduced the amount of cavities and decreased the surface roughness [4].

The infill road orientations +45°/-45° and 0° (parallel to the direction of the tensile force applied in the lap shear test) increased the mechanical performance as opposed to road orientations of 90° (perpendicular to applied force). Especially in the overlap area, a high fraction of 90° oriented roads can decrease the mechanical performance [4].

3.2 Adhesive Bonding and Mechanical Interlocking

The main bonding mechanisms in AddJoining are adhesive bonding and mechanical interlocking [4] (see Figure 3).

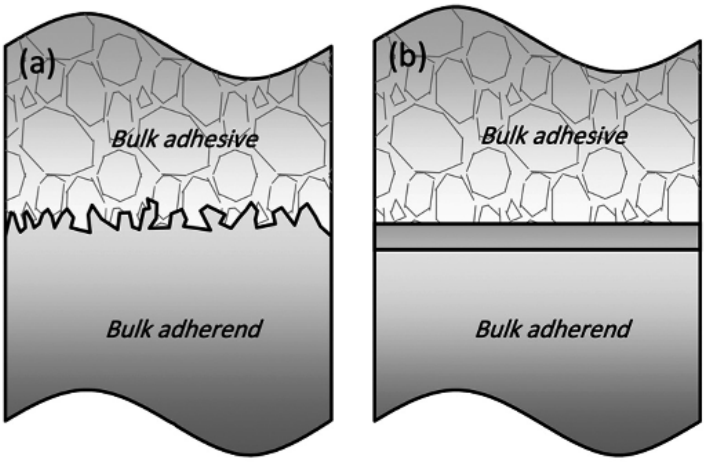

Mechanical interlocking introduced by; *hills, valleys, pores and crevices, etc*

Adsorption (contact adhesion); *Lifshitz–van der Waals interactions*, which include *London dispersion, Keesom polar, Debye induced polar*

Figure 3: Schematic representations of the main bonding mechanisms in AddJoining: Mechanical interlocking (a) and Adhesive bonding (b). Reproduced from [7].

The mechanical interlocking is the mechanical anchoring of one material (normally the adhesive or melted material for adhesively-bonded interfaces [8]; for the AddJoining, the polymer from the coating layer) in the pores and undercuts of the other (solid) material. It can occur on a macroscopic scale (e.g. rubber and textile fabrics) as well as on a microscopic scale (adhesive and substrate) where a composite-like interphase is obtained [9]. While there are various types of surface irregularities (see Figure 4), mechanical interlocking can only be achieved by type 'b' [9]. This is especially true for load in the normal direction with respect to the substrate (failure mode I) and has less impact when applying load in a parallel direction (failure mode II / shear loading) as is predominantly present in lap-shear tests. The degree of interlocking depends on the roughness of the solid, the wetting properties of the liquid, the pressure, the temperature and the humidity [8]. The achieved surface wetting has to be good to obtain a large contact area. If the wetting is poor, the adhesion might even be decreased by the surface irregularities due to the resulting smaller contact area [9]. Lastly, mechanical interlocking is not related to physical-chemical forces [8].

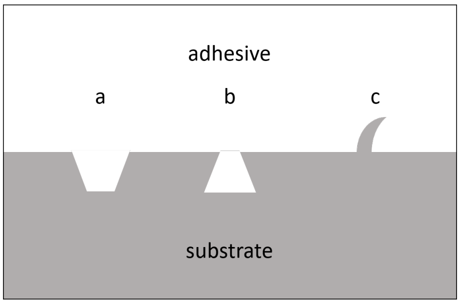

Figure 4: Different types of surface irregularities. Based on [9].

Adhesive bonding is the bonding between two surfaces (similar or dissimilar materials) and adhesion forces exist at all interfaces of solids [8]. However, since they only reach as far as 0.1 µm, which is below the usual roughness of technical surfaces, surface preparation is crucial to obtain adhesive bonding [8]. Causes for adhesive bonding are physisorption as well as chemisorption between the atoms and molecules of both sides [8]. Physisorption is a type of adsorption and is due to the van der Waals forces which are intermolecular forces and have a low selectivity (i.e. exist between all molecules) [10]. Chemisorption is due to chemical bonding and therefore has a higher selectivity [10]. If the adhesion is only due to physical attractive forces, it is generally weaker than if it is due to chemical interaction [8].

3.3 Mechanical surface preparation

To achieve a clean surface with a particular surface roughness, the mechanical surface preparation is crucial [8]. While sandblasting removes material (including the oxide layers that are formed on a titanium surface, see Section 3.6.3), it also leads to a larger surface area which is beneficial for obtaining a strong bond [8]. The abrasives can be metallic, mineral or organic compounds (the word sandblasting only refers to the process nowadays, not to the abrasive) and normally, the mean particle sizes are 0.2 - 2.0 mm [8]. However, due to abrasion, deformation and fragmentation during the sandblasting, the size and shape of the particles change and the distribution shifts towards smaller particle sizes [8].

Lower roughness values are achieved by using finer particles. Depending on the duration of sandblasting and the grain size and hardness of the sample material, a rugged surface with undercuts (like type ’b’ in Figure 4) can be obtained which is beneficial for a stronger mechanical interlocking [8].

The compressed air, which is needed, is generated in compressors. Therefore, small amounts of oil may be present on the surface after sandblasting as well as residual abrasives [8]. Also, impurities that were already on the surface beforehand may be pressed into the surface structure by the abrasives. Therefore, the surface should be degreased before as well as after the sandblasting process [8]. Special care should be taken when handling thin sheet metals, since they can bend due to the compression of the material on the sandblasted side [11]. The bending can be reduced by clamping the sample onto a thick and stiff support. This resulting bending can also be reversed by sandblasting the other side of the metal sheet [8].

3.4 Temperature distribution during Fused-Filament Fabrication

Temperature history and distribution are crucial factors in FFF of polymers regarding mechanical properties, surface quality and dimensional accuracy [12–14]. This is explained by better sintering/interface healing/bonding, which happens if the deposited (adjacent) road remains above glass transition temperature (T_g) for a longer period of time [5, 6, 13, 14]. Lepoivre *et al.* [5] found that low mechanical properties are attributed to macro-pores due to the circular road shape as well as to bad adhesion between neighbouring roads. Both reasons are highly dependent on the temperature. The authors additionally remarked that the temperature also should not be excessively high due to the thermal degradation/chemical ageing and the risk of low viscosity leading to the collapse of the part. To understand the influence of the temperature parameters, the different heat exchange phenomena are important [14]. Costa *et al.* [13] investigated six different heat exchange phenomena:

- Convection with environment: Significant, especially when the road first starts to cool down after being deposited.
- Conduction between adjacent roads: Significant. The temperature of the cooler one increases due to the heating caused by the warmer one, the temperature variation being larger the higher the temperature difference between both. Axial and radial conduction in the road was deemed irrelevant due to its small dimensions.
- Conduction between the first layer and the printing bed: in case of circular roads, there is only a minimal contact area and therefore a small heat exchange. Minor impact for circular roads.
- Radiation between adjacent roads: Minor impact.
- Radiation with environment: Negligible for heat transfer coefficients h(conv) $\geq$ 60W/m².
- Convection with entrapped air: Negligible.

The importance of the conduction between adjacent roads and the negligibility of the temperature gradients in axial and radial direction were already found by Sun *et al.* in 2008 [12]. In their study, with the deposition of each new layer, the temperature of the bottom layer rose above T_g and then quickly decreased again when the nozzle moved away. The minimum temperature in the bottom layer for each of these cycles increased with the deposition of each new layer. Sun *et al.* [12] stated that the temperature of the roads was above T_g throughout a significant time of the process. They also observed that the temperature in the bottom layers remained above T_g for longer than in the upper layers which led to better sintering in the first layers of the part [12].

Costa *et al.* [13] observed that the temperatures across the cross-section of a road are almost uniform except when the thermal contacts are perfect. With an increasing degree of conduction, the uniformity decreases according to them. Axial conduction could be neglected because the temperatures were uniform along small road lengths [13]. The neglection of the axial conduction was also confirmed by Lepoivre *et al.* [5]. Pais [14] reported that the most important heat transfer mechanisms for sintering are the convection with the environment and the conduction between the print bed and deposited roads. According to them, the sintering is not affected much by the heat that is dissipated by the nozzle itself and the surrounding air. The authors explain this with the fast cooling of the road after deposition, which leads to only a very short time span where the deposited road is at a temperature above the critical sintering temperature [14].

Additionally, to controlling the bed and the nozzle temperature, the envelope or environment temperature should be controlled to achieve optimal sintering conditions [12, 14]. To achieve a minimum of residual stresses and distortions, the material should be maintained close to T_g after deposition [14]. To control the envelope temperature, Pais [14] also suggested to control air circulation within the thermally insulated chamber. The authors said that this reduces temperature gradients which cause warping and sometimes even cracks in the printed parts. Furthermore, the authors reported that the temperature gradient develops along the road length due to the fast cooling of the road after deposition and increases when the part becomes higher. The warping decreased linearly with an increasing envelope temperature. However, Pais [14] also remarked that even considering all of this, they did not manage to obtain a uniform temperature in the deposited roads. Furthermore, they stated that besides the envelope temperature, warping is also influenced by the number of deposited layers, their length and the shrinking coefficient of the material.

According to Spoerk *et al.* [15], another important factor is the adhesion between the first layer of the printed part and the printing bed, since it acts as the foundation for the whole part. The authors stated that a good adhesion during the FFF process is desirable while after printing, however, it should be low enough to allow the removal of the part. The authors gave eight recommendations for improving the adhesion [15]:

- Clean printing surface,
- Level the printing bed to promote close contact between first layer and printing bed,
- Cover printing surface with polymeric tapes,
- Sand polymeric tape to slightly increase its surface roughness,
- Apply water-soluble glues, hair sprays or special coatings,
- Print on a plate or film of the same material as the one being printed,
- Print on well-fixed surfaces,
- Increase bed temperature to a recommended value (depending on the material).

To avoid problems such as bubbles when printing on (sanded) polymeric tapes, Spoerk *et al.* [15] suggested to increase the bed temperature. However, this may make it more difficult to remove the part after printing. In this case, they recommended to cool down the printing bed before part removal to lower the adhesion forces. During printing, they found optimal adhesion for bed temperatures slightly above T_g. This is due to the decrease of surface tension between the deposited road and the bed and therefore a larger contact area [15].

Some studies found that the position of the part on the building platform also influences the quality of the obtained part due to differences in the temperature distribution [6, 12, 14]. Sun *et al.* [12] observed a higher sintering percentage as well as a better surface in parts produced in the middle of the platform than in those produced in the corners. They ascribed this to an inhomogeneous air flow in the building chamber which led to different temperature profiles depending on the building location. Pais [14] found that the position on the platform influenced the amount of warping of the printed parts and suggested that this was due to the non-uniform temperature distribution.

3.5 Lap shear testing

Lap shear testing is a standard destructive test method (ASTM D3165) which is used to compare the shear strength of adhesive joints. There are several possible configurations and its trivial test procedure allows for a quick acquisition of results [16]. In the single lap shear test, tension forces are applied to two adhesively joined rectangular plates (see Figure 5) [16].

In this work, the polymer is printed directly onto the metal part. Therefore, there is no adhesive present. All other test parameters remain the same as for adhesively bonded joints.

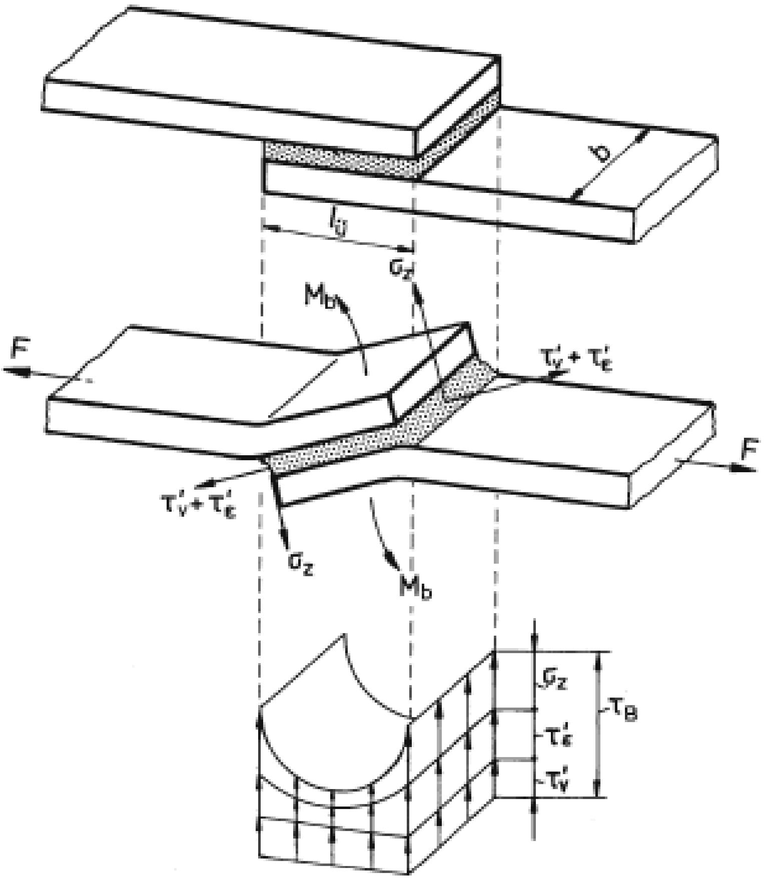

Figure 5: Lap shear test. Reproduced from [8].

The overall stress condition in the adhesive bond of a single lap joint is composed of several shear and tensile stresses [8]. This is due to the bending of the sample during testing in addition to the tensile force that is applied (see Figure 5). As the applied force increases, the equivalent stress increases as well, especially in the overlapping ends [8].

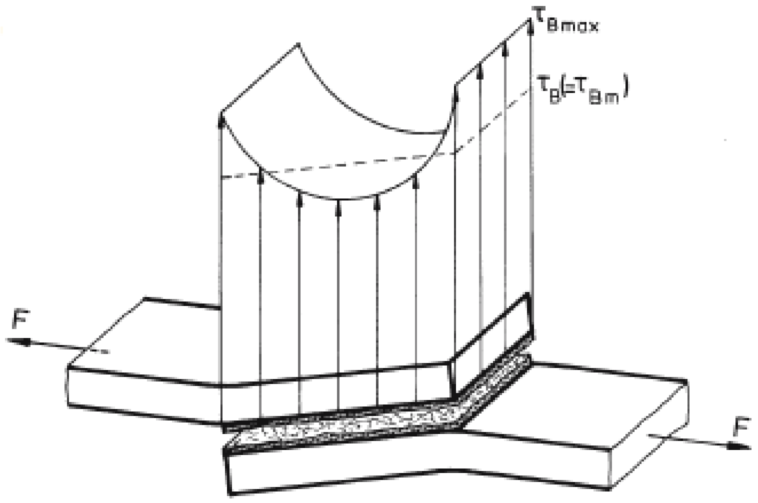

Figure 6: Occurring stresses in a lap shear test (simplified for ideally elastic adhesive). Reproduced from [8].

Due to the superposition of the stresses, no pure shear stresses can be determined with single lap shear tests [8]. Instead, the resulting overall stress is called lap shear stress and as a result of the test we obtain the intermediate lap shear strength at failure τ_B (see Equation 3.1) [8]. This is not to be confused with the maximum lap shear stress τ_{Bmax} at the overlapping ends at failure. Figure 6 represents the stress distribution at break for an ideally elastic behaviour of the adhesive. Therefore, the stress peaks are lower in reality [8]. Failure starts when the resulting local stress at the overlapping ends τ_{max} reaches τ_{Bmax} [8]. It begins at those overlapping ends and proceeds from there through the whole bonding [8].

$$\tau_B = \frac{F_{max}}{A} = \frac{F_{max}}{l_o * w} \tag{3.1}$$

where

- τ_B [MPa] is the intermediate lap shear strength at failure
- F_{max} [N] is the maximum force
- A [mm²] is the bonding area
- l_o [mm] is the overlapping length
- w [mm] is the width of the sample

For the failure of a single lap joint, the local stress condition τ_{Bmax} at the end of the overlap (most stressed region) is crucial, not the intermediate failure shear strength τ_B [8]. Therefore, the validity of τ_B is very limited and τ_B can not be related directly to the failure of the adhesive bond, since it does not take into account crucial factors like geometry, material parameters, load cases, surface condition and maximum stresses [8]. Hence, τ_B is no specific parameter of an adhesive but only valid in combination with a certain material of the adherend [8].
With an increasing overlapping length l_o, the sample bends less and therefore, τ_B decreases to a certain extent which is dependent on the deformability of the adhesive [8]. Therefore, an adhesive that is stronger than another one for a given overlapping length might become the weaker one when the overlapping length is increased [8]. In this case, both adhesives will be weaker, but τ_B

may decrease at a different rate [8]. This observation can be attributed to the larger deformability of an adhesive leading to a smaller τ_{Bmax} at the overlapping ends [8].

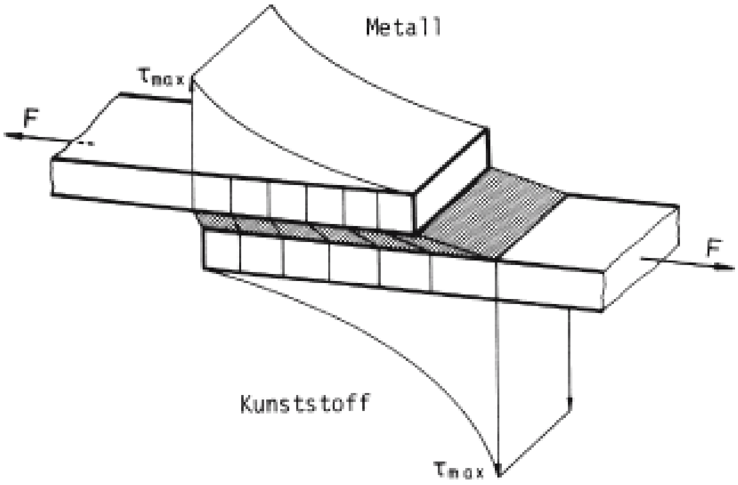

Figure 7: Stress distribution during a lap shear test of a metal-polymer adhesive joint. Reproduced from [8].

The stress distribution of a metal-metal adhesive joint is inhomogeneous but symmetrical (see Figure 6), which leads to mostly cohesive failure in the lap shear test [8]. However, for metal-polymer addjoints, this is not the case due to their different mechanical properties: polymers have a much smaller elastic modulus and a much larger elongation than metals [8]. The firmly bonded joint leads to hindrance of deformation (see Figure 7) and therefore to internal stresses. These may cause multiaxial stresses, which lead to a brittle behaviour [8]. This is also the reason why, in metal-polymer adhesive joints, often the polymer part breaks close to the overlapping area [8]. If no cohesive failure occurs, the significance of the lap shear test regarding the lap shear strength of the adhesive is very limited [8]. To prevent failing due to fracture in the polymer part itself, the thickness of the polymer part can be increased to increase the stiffness and the overlapping length can be decreased to obtain a more symmetrical stress distribution [8].
Even if the obtained lap shear strength is not a specific material parameter, the test results provide valuable information in comparative studies such as the present one: based on the test results, process parameters can be evaluated and more specific investigations can be planned [8].

3.6 Materials

3.6.1 Unreinforced Polymer - PA

A PA6/66 copolymer consists of polyamide-6 and polyamide-6,6. Polyamide-6 (also known as nylon-6 and polycaprolactam) is a semi-crystalline thermoplastic polymer with high tensile and impact strength. Some of the physical and mechanical properties are shown in Table 2.

Table 2: Selected physical and mechanical properties of PA6 [17, 18].

Density [g/cm³]	1.14
Humidity absorption [%]	9.5
Tensile strength [MPa]	64
Yield strength [MPa]	27.8
Tensile elongation at break [%]	220
Melting temperature [°C]	185 - 195
Glass transition temperature [°C]	50

Polyamides (compared to other polymers) generally have a high tensile strength, stiffness and hardness [18]. They also show a good shape stability even at high temperatures, which, with respect to the FFF process, leads to a fairly high printing temperature (240 - 260 °C) [18, 19]. Furthermore, polyamides display a high abrasion resistance and damping ability as well as a high resistance against solvents, lubricants and fuel [18].

PA6 belongs to the aliphatic (non-aromatic) polyamides and is synthesized via anionic or hydrolytic ring-opening polymerisation of the cyclic ϵ-caprolactam [18]. The reaction for the hydrolytic polymerization is shown in Figure 8.

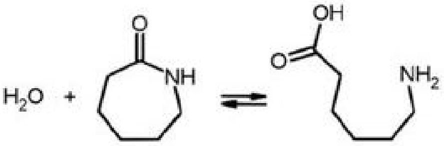

Figure 8: Hydrolytic ring-opening polymerization of ϵ-caprolactam to obtain PA6. Reproduced from [20].

The number 6 in PA6 declares that there are six carbon atoms in each monomer [18]. If there are two numbers (e.g. PA6,6), the first one is the number of carbon atoms in the diamin and the second one states the number of carbon atoms in the dicarbon-acid [18]. Both PA6 and PA6,6 have the chemical formula $(C_6H_{11}ON)_n$ but differ in their structural set-up: while in PA6,6, the NHCO-groups of the neighbouring polyamide molecules are always facing each other and form hydrogen (bridge) bonds, in PA6 this only occurs for every second NHCO-group (see Figure 9) [18]. The hydrogen (bridge) bonds lead to bonds that are two to three times stronger than the usual intermolecular forces [18]. Therefore, PA6 has a lower melting temperature than PA6,6, which has T_m = 255°C [18]. If more carbon atoms are present in the monomer (e.g. PA11), the distance between the NHCO-groups increases and therefore, the melting temperature decreases (T_m = 180°C) [18]. The degree of crystallisation of PA6 is directly proportional to the mechanical properties and varies with the cooling rate: 10 % is achieved at fast cooling and 50 - 60 % at slow cooling [18].

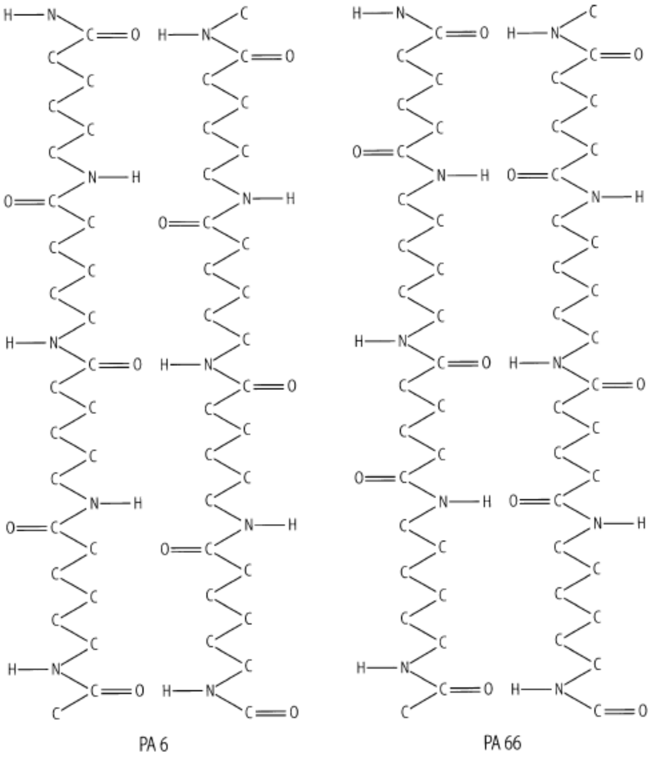

Figure 9: Molecule structure of PA6 and PA6,6. Reproduced from [18].

3.6.2 Reinforced Polymer - PA-CF

The technical grade polyamide reinforced with 15 wt.% of short carbon fibres (PA-CF) has a higher tensile strength and much lower elongation at break than PA6 (see Table 3). Its melting and glass transition temperature are slightly higher than those of PA6 [21].

Table 3: Selected physical and mechanical properties of (dry specimen, print direction XY) PA-CF [21].

Density [g/cm³]	1.23
Humidity absorption [%] (23°C, 50 % RH)	<2.0
Tensile strength [MPa]	103.2
Tensile elongation at break [%]	1.8
Crystallisation temperature [°C]	180
Melting temperature [°C]	234
Glass transition temperature [°C]	70

Van de Werken *et al.* [22] described that during the filament production of carbon-fibre reinforced polymers, pores are introduced in the material due to the poor adhesion at the interface between the thermoplastic and the carbon fibres. Many other short fibre reinforced filaments (PA, PEEK, ABS, PLA) show a similar behaviour [22–25].

Verdejo de Toro *et al.* [26] conducted a study about how the mechanical properties of 20 % short carbon fibre-reinforced polyamide are affected by the printing parameters in an FFF process. The samples were thermally and mechanically tested. The executed mechanical tests included a tensile test, bending test, Charpy test and a hardness test. In that study, the overall mechanical properties improved with a high infill density (100 %), a low layer height (0.2 mm), a concentric printing pattern (opposed to a linear ±45°C pattern) and a nozzle diameter of 0.8 mm.

3.6.3 Metal - Ti-6Al-4V (Grade 5)

Titanium is known for its high specific strength and good corrosion resistance [8]. It undergoes an allotropic transformation at a certain temperature, namely the β-transus temperature T_β [27]. Due to the microstructure change at T_β, a resulting change of the physical and mechanical properties occurs [28]. Below T_β, the microstructure is named α-phase and assumes a hexagonal closed packed (hcp) lattice, having therefore less slip systems and a worse formability [28]. Above T_β, the microstructure is named β-phase and it assumes a body-centred cubic (bcc) lattice with more slip systems and thus a better formability. The β-phase has also a larger volume due to the lower packing density [28]. Depending on the alloying elements, the transition temperature can be shifted: α-stabilizers shift T_β to higher temperatures, whereas β-stabilizers shift them to lower ones (see Figure 10) [28].

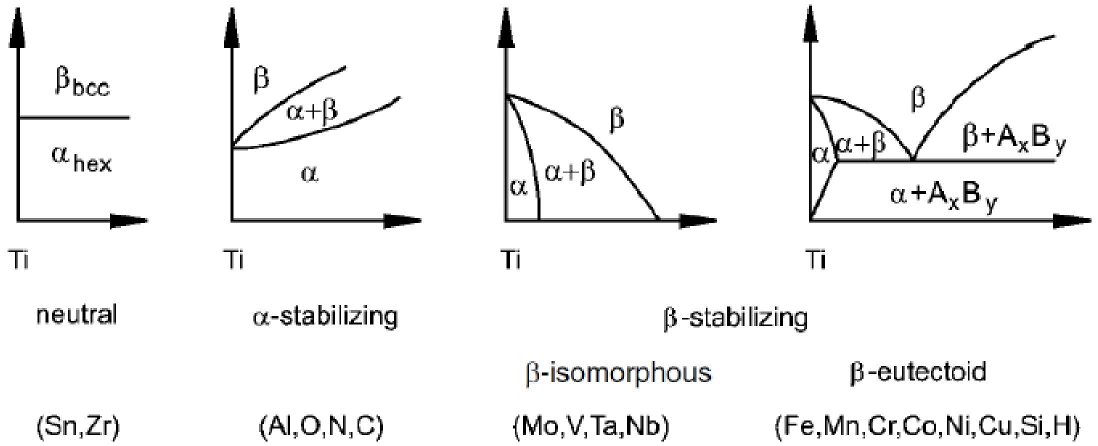

Figure 10: α- and β-stabilizing alloying elements in titanium. Reproduced from [28].

Ti-6Al-4V is an α+β titanium alloy and the most used of all titanium alloys, especially in the aerospace industry, where it is widely applied [28]. The combination of both, the α- and the β-phase at room temperature improves the formability and strength of the material [27]. Aluminium (α-stabilizer) and vanadium (β-stabilizer) lead to solid solution strengthening [28]. Selected physical and mechanical properties of Ti-6Al-4V are shown in Table 4.

Table 4: Selected physical and mechanical properties of Ti-6Al-4V [28, 29].

T_β [°C]	995
Hardness [HV]	300 - 400
E-modulus [GPa]	100 - 140
Yield strength [MPa]	800 - 1100
Tensile strength [MPa]	900 - 1200
Elongation [%]	13 - 18
K_{IC} [MPam$^{1/2}$]	33 - 110

The chemical composition of Ti-6Al-4V, Grade 5 according to ASTM B348 Grade 5 is shown in Table 5.

Table 5: Chemical composition of Ti-6Al-4V (Grade 5) [29].

Weight (%)	N	C	H	Fe	O	Al	V
Min	-	-	-	-	-	5.5	3.5
Max	0.05	0.08	0.015	0.40	0.20	6.75	4.5

An example of the microstructure of a Ti-6Al-4V plate with an α-volume fraction of 93-94 % is shown in Figure 11. While the α-phase appears in white, the β-phase appears in black. In the equiaxed microstructure, primary α grains can be identified. Furthermore, needle-shaped α is present within the β-matrix which has been transformed [30].

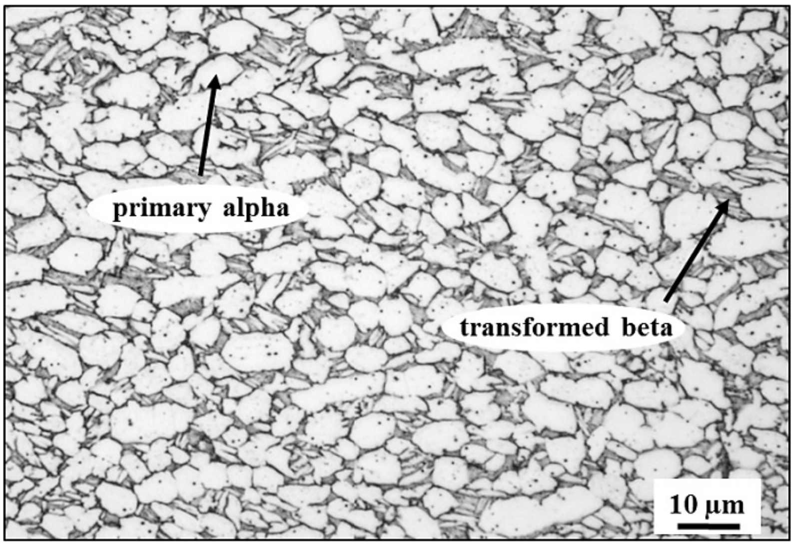

Figure 11: Example of the microstructure of a Ti-6Al-4V plate. Reproduced from [30].

The surface structure of titanium is complex: it consists of different oxide structures (chemically and morphologically) which is crucial for the shear strength of the adhesive joint [8]. Therefore, the surface preparation methods before adhesive bonding depend on the type of titanium alloy used [8]. Different combinations of mechanical and chemical treatments are possible. Generally, oxide layers that formed during production and storage should be removed and, after removal, the workpiece should be adhesively joined directly or a primer should be applied due to the high reactivity of titanium with oxygen [8]. If the requirements of the adhesive joint are not too high regarding ageing, mechanical surface treatments like sandblasting can replace a chemical pre-treatment (see also Section 3.3) [8].

4 Materials and Methods

4.1 Materials

The metallic substrate for the AddJoining consisted in rolled, sandblasted Ti-6Al-4V sheets (sandblasting parameters are presented in Section 4.2.1. The first layer of polymer that was printed onto the metallic substrate is referred to as coating layer and was made from an Ultimaker Transparent PA filament consisting of unreinforced polyamide-6/66 copolymer (PA). The rest of the AddJoining sample, referred to as composite part, was printed with a BASF Ultrafuse PAHT CF15 filament, consisting of technical grade polyamide with a fibre fraction of 15 wt.% short carbon fibres as reinforcement (PA-CF). Both filaments had a diameter of 2.85 mm. The data sheets for all the materials used can be found in Annex I for the reinforced PA-CF, and Annex II for the PA and Annex III for the metal).

4.2 Methods

4.2.1 FFF additive manufacturing

For all experiments, an Ultimaker S5 FFF-printer (Netherlands) was used to 3D-print the polymers. The polymer filaments were kept in heated filament storage boxes to avoid moisture absorption which would lead to worse mechanical properties.

For the unreinforced PA, a standard nozzle with a diameter of 0.4 mm was used. However, in the case of the PA-CF filament, regular copper nozzles would have to be changed regularly due to wear, which results in clogging of the material. To avoid having to change the nozzle regularly, a reinforced nozzle with a diameter of 0.6 mm was used for the carbon fibre reinforced polymer. It has a ruby cone tip which leads to a high wear-resistance [31]. Therefore, it is suitable especially for printing abrasive materials [31].

The dimensions of the Ti-6Al-4V plates, which were used as substrate, were 25.4 mm x 100 mm x 0.6 mm. Before printing the polymer onto the Ti-6Al-4V plates, the latter were sandblasted, as a means of increasing surface irregularities and therefore the possibilities for mechanical interlocking between polymer and metal, as explained earlier. The applied sandblasting parameters are shown in Table 6.

Table 6: Sandblasting parameters.

Pressure	4.5 bar
Particles	Corundum
Particle size (average)	34 μm
Angle	approx. 60°
Distance Nozzle - sample	10 cm
Nozzle diameter	3 mm

The dimensions of the sample holder that was used for fixing the Ti-6Al-4V plates during the AddJoining can be seen in Figure 12. It was cut from an aluminium sheet using a water jet cutter, according to the dimensions of the Ti-6Al-4V plates used as a substrate.

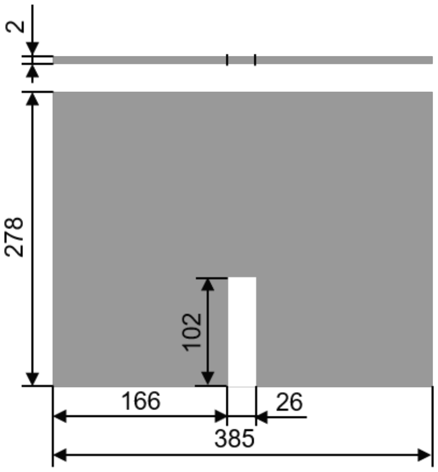

Figure 12: Aluminium sample holder (all dimensions in mm).

4.2.2 Mechanical testing

For the tensile testing of the composite part optimisation samples as well as for the lap shear testing of the coating layer optimisation samples, a ZwickRoell Z100 (ZwickRoell, Germany) test machine was used, which includes a load cell of 150 kN/mm. The transverse speed was 1mm/s and the tests were performed at room temperature. Tensile tests were conducted with the samples from the composite part optimisation to compare their UTS. The sample geometry was based on the ISO 527-IBA (see Figure 13).

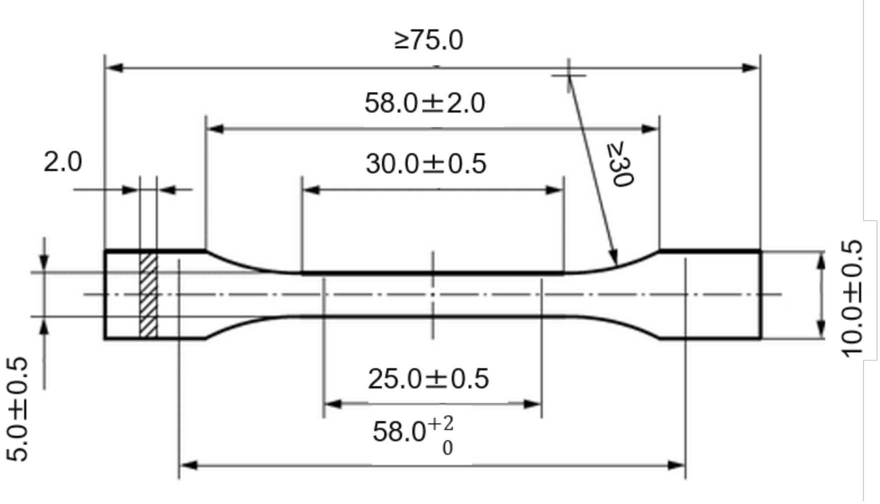

Figure 13: Tensile specimen geometry (ISO 527-IBA). Adapted from [32].

With the samples from the coating layer optimisation, lap-shear tests were conducted to compare their ultimate lap shear strength (ULSS). Concerning the sample geometry (Figure 14), the ASTM D1002 standard was adapted which defines the geometry of lap-shear test samples of adhesively joint metals.

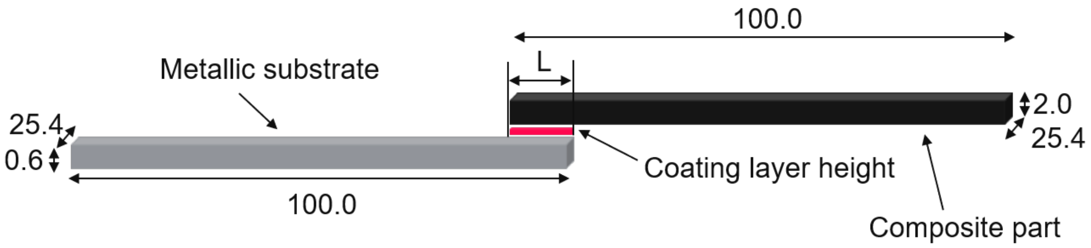

Figure 14: Geometry of the single-lap joint coating layer optimisation samples (all dimensions in mm). L is the overlap length.

4.2.3 Composite part optimisation (CPO) - DoE

The goal of the composite part optimisation was to establish the best process parameters in order to maximize the tensile strength of the composite part, so that in the coating layer optimisation, strong lap shear specimens could be produced. In the course of this, the influence of different process parameters on the mechanical performance of the printed composite part samples were evaluated. The parameters taken into account were the printing speed v [mm/s], the nozzle temperature T_{ext} [°C], the bed temperature T_{bed} [°C] and the layer height h [mm]. Their values were varied within the range that was recommended by the manufacturer (as of March 2020), see Table 7.

Table 7: Recommended values for the printing parameters [21].

Parameter	Value
Printing speed v [mm/s]	30 - 80
Nozzle temperature T_{ext} [°C]	240 - 280
Bed temperature T_{bed} [°C]	100 - 120
Layer height h [mm]	0.2 - 0.4
Nozzle diameter [mm]	0.6 (constant)
Road width [mm]	0.4 (constant)
Air gap [mm]	0.4 (constant)
Stacking sequence	0° / 90°

A Design of Experiments (DoE) was carried out according to a 2k-full factorial design with four factors and one centre point. Two extra conditions were added to improve the fit of the model. Therefore, the total number of test conditions in this DoE was 19 (see Figure 15). Four replicas (samples) were printed for each of Conditions 1 to 19 (see Table 8) in a random order. For the printing bed, the standard glass plate which came with the printer was used.

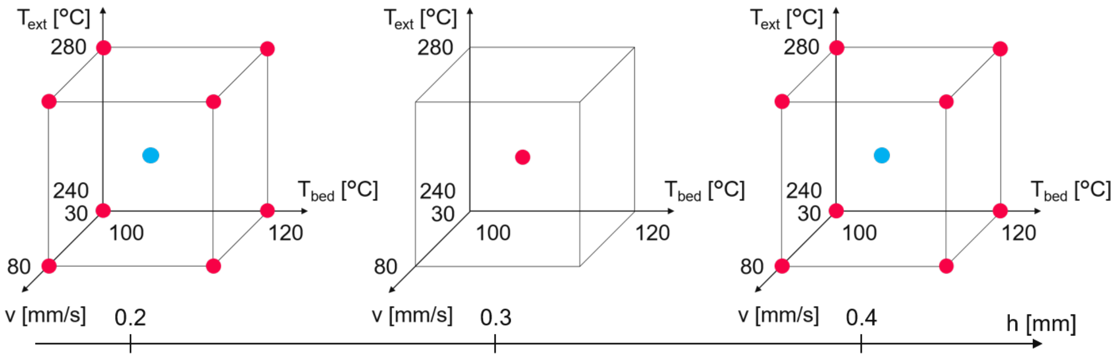

Figure 15: Graphic representation of the DoE conditions. Each point represents one of the conditions. The two extra conditions are marked in blue.

After the mechanical testing, for each of the two best fitting solutions (optimised conditions) according to the statistical analysis, eight samples were printed. The calculation of the optimised parameters is explained in more detail in Section 4.2.5.

Table 8: Printing parameters of the tested conditions during CPO.

Condition	Printing speed	Bed temperature	Nozzle temperature	Layer height
	v [mm/s]	T_{bed} [C°]	T_{ext} [C°]	h [mm]
C1	30	100	240	0.4
C2	30	120	240	0.4
C3	80	100	240	0.4
C4	80	120	240	0.4
C5	30	100	280	0.4
C6	30	120	280	0.4
C7	80	100	280	0.4
C8	80	120	280	0.4
C9 (Extra condition)	55	110	260	0.4
C10	30	100	240	0.2
C11	30	120	240	0.2
C12	80	100	240	0.2
C13	80	120	240	0.2
C14	30	100	280	0.2
C15	30	120	280	0.2
C16	80	100	280	0.2
C17	80	120	280	0.2
C18 (Extra condition)	55	110	260	0.2
C19 (Center point)	55	110	260	0.3

4.2.3.1 Printing bed material study

As the sample holder for the coating layer optimisation samples is not made of glass (like the original printing bed) but of aluminium, additional samples were also printed on an aluminium plate, which was placed on the built-in heated metal plate. For the printing parameters, the optimised condition based on the previous tests was used, allowing for a comparison between the resulting mechanical performance of the part 3D-printed on different printing bed materials. The same tests were also conducted with one, two, three and four layers of polyimide (PI) tape on the aluminium printing bed for further comparable results. Materials and dimensions of the different printing bed surfaces along with the sample ID (condition) are presented in Figure 16.

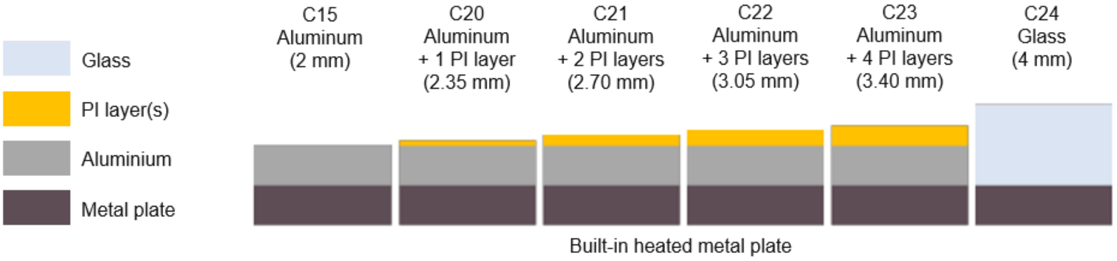

Figure 16: Materials and dimensions of the different printing bed surfaces.

Adding layers of PI tape can help to avoid problems regarding the removal of the CLO samples from the sample holder as well as providing a smoother surface to print on. All printed samples were taken out of the printer after they cooled down for 5 minutes and tested with the tensile test machine at room temperature.

4.2.4 Coating layer optimisation (CLO) - OFAT

The goal of the coating layer optimisation was to find the most suitable AddJoining process parameters for printing the coating layer (unreinforced PA). Based on the results obtained from Section 4.2.3.1, the aluminium sample holder was covered with two layers of PI tape in the printing area. A graphic representation of this set-up can be seen in Figure 17.

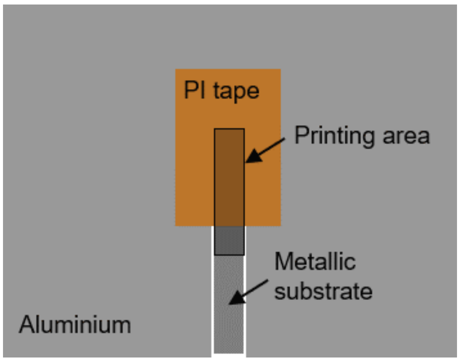

Figure 17: Aluminium sample holder with PI tape.

The printing parameters were analysed using the one-factor-at-a-time (OFAT) approach. Therefore, only one parameter was changed at a time, then the one which gave the best results was fixed and in the next stage the next parameter was varied. The investigated parameters were the printing speed v [mm/s], the nozzle temperature T_{ext} [°C], the bed temperature T_{bed} [°C] and the coating layer height h [mm]. Their values were varied within the ranges shown in Table 9, which were selected based on literature research and experimental experience. In Table 10 the values of each tested condition are displayed.

Table 9: Printing parameters of the coating layer.

Parameter	Value
Printing speed v [mm/s]	5 - 50
Nozzle temperature T_{ext} [°C]	240 - 280
Bed temperature T_{bed} [°C]	100 - 150
Coating layer height h [mm]	0.1 - 0.3
Nozzle diameter [mm]	0.4 (constant)
Road width [mm]	0.4 (constant)
Air gap [mm]	0.4 (constant)
Stacking sequence	0°

Table 10: Printing parameters of the tested conditions with an overlap length of 12.5 mm.

Condition	Printing speed	Nozzle temperature	Bed temperature	Coating layer height
	v [mm/s]	T_{ext} [°C]	T_{bed} [°C]	h [mm]
C1	5	280	150	0.1
C2	20	280	150	0.1
C3	50	280	150	0.1
C4	50	240	150	0.1
C5	50	260	150	0.1
C6	50	260	120	0.1
C7	50	260	100	0.1
C8	50	260	140	0.1
C9	50	260	150	0.2
C10	50	260	150	0.3

After printing the coating layer, the sample was left to cool down until the bed temperature was at 60 °C (25 minutes after the print job). Then, the rest of the sample (composite part) was printed with the PA-CF filament applying the optimised printing parameters based on the results of the composite part optimisation (see Table 11). After this second printing stage, the sample was taken out after the printing bed cooled down to 70 °C (15 minutes after the print job).

Table 11: Printing parameters of printing stage 2 based on results of composite part optimisation.

Printing speed	Nozzle temperature	Bed temperature	Layer height	Printing bed material
v [mm/s]	T_{ext} [C°]	T_{bed} [C°]	h [mm]	-
30	280	120	0.2	Al + 2 PI layers

Subsequently, lap-shear tests were conducted with the obtained single-lap joint samples to compare their ultimate lap shear strength (ULSS).

For Conditions C3, C5, C8, C9 and C10, the samples did not break due to adhesive failure near the interface but due to net-tension failure in the composite part (see Section 5.3). Therefore, the strength of the interface could not be assessed for these conditions. Thus, to prevent this undesired net-tension failure (at least for testing purposes), these samples were reprinted and retested with a reduced overlap length of 6 mm (as opposed to the overlap length of 12.5 mm used previously) in an effort to induce a failure at the polymer/metal interface (see Section 3.5). This way, a comparison of the bonding strength between different conditions could be made.

Table 12: Printing parameters of the tested conditions with the reduced overlap length of 6mm.

Condition	Printing speed	Nozzle temperature	Bed temperature	Coating layer height
	v [mm/s]	T_{ext} [C°]	T_{bed} [C°]	h [mm]
C11	50	280	150	0.1
C12	50	260	150	0.1
C13	50	280	140	0.1
C14	50	280	150	0.2
C15	50	280	150	0.3

4.2.5 Statistical Analysis

For the CPO, Minitab (Minitab, USA) was used to find the optimised parameter set and to analyse the influence of the parameters that were varied. The Minitab optimizer finds the maxima of the regression equation within the tested intervals by setting the partial derivatives of the equation (with respect to each one of the four parameters) equal to zero and then solving the ensuing system of equations. If the maximum is located at the edge of the interval, the regression equation would need to be solved for all 16 vertices of the hypercube and subsequently the results would have to be compared with each other.

For all test results (composite part optimisation and coating layer optimisation), an Analysis of Variance (ANOVA) (via Microsoft Excel data analysis) with a confidence interval of 95 % (α = 0.05) was executed to determine the statistical significance of each parameter. That means that all parameters with a p-value < 0.05 are statistically significant within the confidence interval according to this analysis.

4.2.6 Microscopical analysis

For the microstructural analysis, additional samples were prepared in the same way as the CLO samples but were not tested. Instead, they were cut in the joint area along their width and cold embedded with epoxy resin. To prepare the embedded samples, they were ground with sandpaper (conditions displayed in Table 13). Then, their cross-sectional surface was microscopically documented and analysed with a Zeiss AX10 Observer.Z1m optical microscope (Germany).

Table 13: Grinding conditions.

Rotation speed	100 rpm
Force	5 N
Time	5 min
Average particle diameter	21.8, 10.3, 5.0 μm

A Zeiss SteREO Discovery.V20 stereo microscope (Germany) was used to analyse the fracture surface of the samples macroscopically. For the microscopic analysis of the fracture surfaces, a Tescan Mira 3 secondary electron microscope (SEM) (Czech Republic) was utilized. As the samples themselves are not conductive, they were coated with carbon using a Bal-Tec SCD 050 sputter coater (Germany) beforehand. Concerning the SEM analysis, mainly the secondary electron detector was used. In that case the signal depends on the topology of the sample and areas facing towards the detector appear brighter than those facing backwards [33]. However, for some areas, the signal of the back-scattered electron detector was used to be able to better distinguish between the polymer and the metal. Due to the higher atomic number of titanium (22) compared to carbon (6), titanium generated more back-scattered electrons and appeared lighter than the polymer [33].

4.2.7 Thermographic Analysis

In the CPO, the printing process was analysed thermographically with the infrared (IR) camera ”VarioCAM HD” (Germany) for seven conditions (C6, C11, C14, C15, C17, C20, C21). This was done in an effort to better understand the temperature distribution during the printing process and how it was influenced by the printing direction and the printing bed material. The IR camera was held at a distance of 200 mm from the sample during the printing process. The selected emissivity factor ϵ was 0.95 and the incidence angle was 0°.

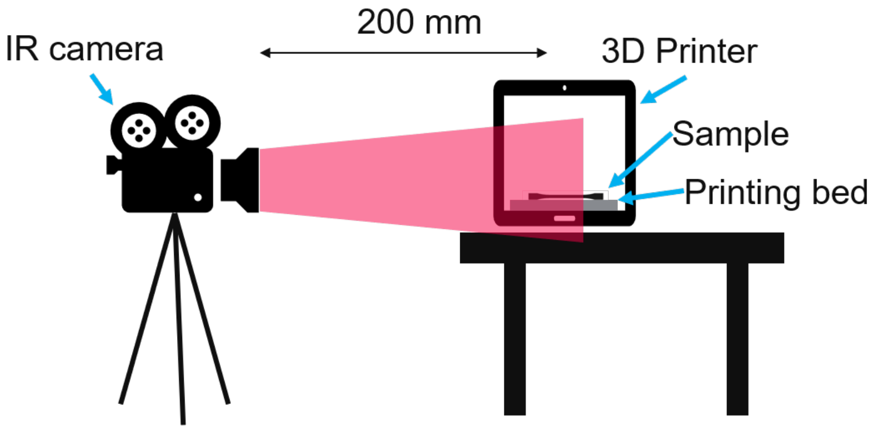

Figure 18: Sketch of the measurement set-up for the thermographic analysis.

4.2.8 Metal Characterisation

For better understanding of the influence of the sandblasting, the roughness of the non-treated as well as of the treated (sandblasted) Ti-6Al-4V plates was measured with a Keyence VHX-6000 digital microscope (Japan). The magnification was 200x and the measured areas were 5 mm x 5 mm each. For image filtering, the gaussian type was chosen with an S-filter of 25 µm and an L-filter of 2 mm.

Furthermore, the plates were cut and embedded, so that the cross-section could be investigated. After preparing the samples using standard metallography procedures for titanium alloys, they were microscopically analysed.

5 Results and Discussion

5.1 Metal characterization

The sandblasted Ti-6Al-4V plates appeared more homogeneous as opposed to the non-treated plates, which are generally sleeker but feature many scratches. However, overall, there was no difference between the measured roughness of the sandblasted plates (S_a = 1.39 ± 0.1 µm) and the roughness of the non-treated ones (S_a = 1.30 ± 0.06 µm). The real surface area for both conditions is on average 25 % higher than the nominal one.

Nonetheless, differences at the surface profiles for both conditions could be observed. This reflects the obvious differences that were already pointed out (i.e. the fact that non-treated samples presented scratches distributed inhomogeneously across their surfaces). The profiles of the sandblasted plates are rougher and offer therefore more possibilities for mechanical interlocking. An example of a roughness profile of each condition can be seen in Figure 19.

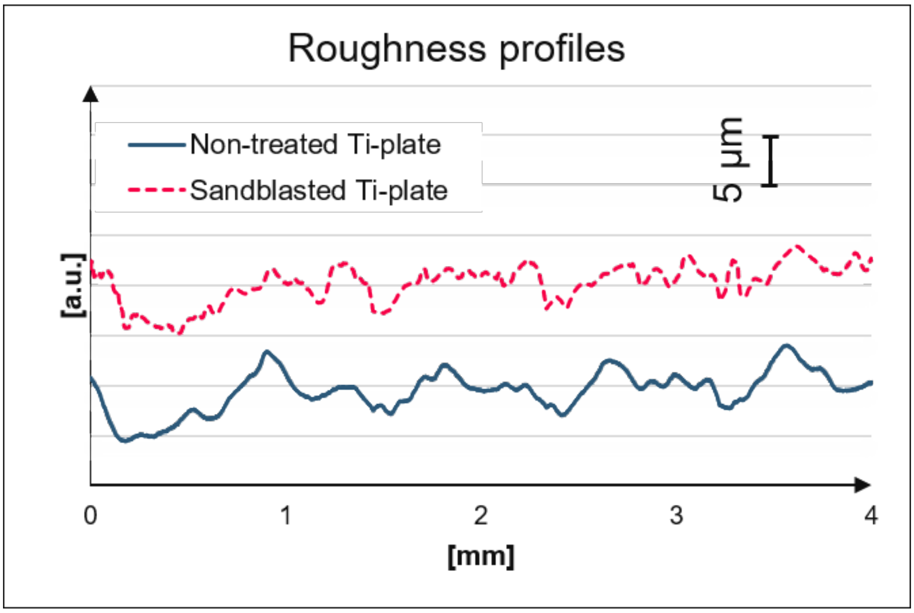

Figure 19: Roughness profiles of a sandblasted Ti-6Al-4V (blue line) and a non-treated Ti-6Al-4V substrate (red dotted line). The distance between two lines on the vertical scale is 5 µm.

No microstructural differences between both conditions (i.e. the treated (sandblasted) and the non-treated Ti-6Al-4V plates) could be observed (see Figure 20). The α-phase (dark grey) and the β-phase (light grey) could be identified. The microstructure is equiaxed and consists mostly of large primary α-grains [34, 35]. This is typical for an α+β-titanium alloy that has experienced a hot rolling process followed by slow cooling, since a slow cooling rate promotes the nucleation as well as the growth of those grains [34, 35].

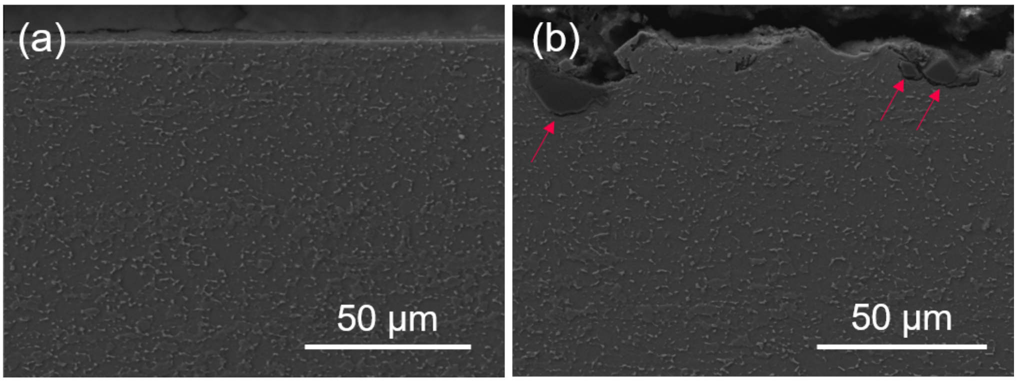

Figure 20: SEM micrograph of the Ti-6Al-4V substrate. (a) is a micrograph of a non-treated sample, (b) is a micrograph of a sandblasted sample. Pink arrows indicate corundum particles introduced by the sandblasting.

The surface of the sandblasted samples is less smooth than the surface of the non-treated ones. This is probably a consequence of plastic deformation during the sandblasting. Corundum particles which must have been introduced during the sandblasting process could be identified and are indicated in Figure 20 by pink arrows. Figure 21 shows an area of plastic deformation of a sandblasted sample. For Figure 21 (a), a back-scattered electron detector was used. Therefore, the corundum particles appear very dark and the deformation of the Ti-6Al-4V substrate is more apparent.

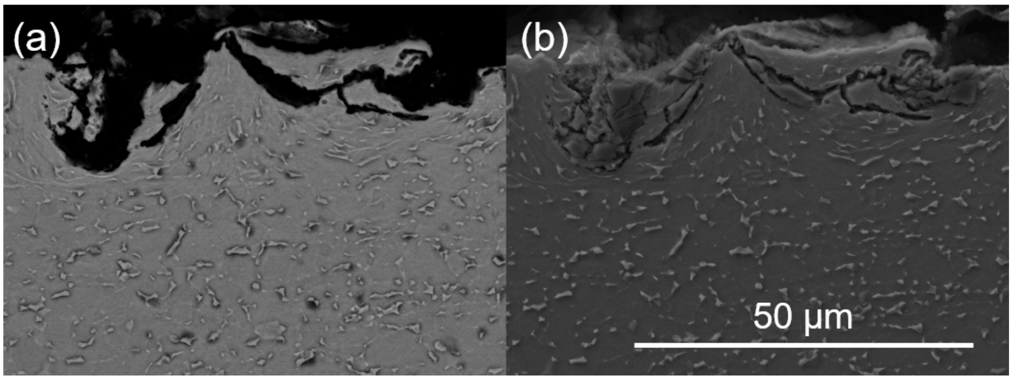

Figure 21: SEM micrograph of the sandblasted Ti-6Al-4V substrate. For micrograph (a), a back-scattered electron detector was used. For micrograph (b), a secondary electron detector was used.

5.2 Composite part optimisation - DoE

The UTS values of the tested samples varied between 89.2 ± 2.9 and 117.1 ± 6.1 MPa (see Table 14) and depended highly on the process parameters. Based on those results, a regression model was obtained with the Minitab software. The regression equation, as well as the model summary, are presented in Table 15.

Table 14: Printing parameters and results of the tested conditions.

Condition	Printing Speed	Bed temperature	Nozzle temperature	Layer height	UTS
	v [mm/s]	T_{bed} [C°]	T_{ext} [C°]	h [mm]	R_m [MPa]
C1	30	100	240	0.4	97.0 $\pm$ 6.2
C2	30	120	240	0.4	102.8 $\pm$ 2.2
C3	80	100	240	0.4	91.0 $\pm$ 4.1
C4	80	120	240	0.4	92.3 $\pm$ 5.9
C5	30	100	280	0.4	89.3 $\pm$ 2.9
C6	30	120	280	0.4	89.5 $\pm$ 6.6
C7	80	100	280	0.4	100.3 $\pm$ 3.8
C8	80	120	280	0.4	102.8 $\pm$ 5.6
C9	55	110	260	0.4	99.9 $\pm$ 3.2
C10	30	100	240	0.2	111.0 $\pm$ 5.4
C11	30	120	240	0.2	112.0 $\pm$ 8.1
C12	80	100	240	0.2	95.3 $\pm$ 8.2
C13	80	120	240	0.2	105.8 $\pm$ 8.5
C14	30	100	280	0.2	112.3 $\pm$ 4.0
C15	30	120	280	0.2	117.0 $\pm$ 4.1
C16	80	100	280	0.2	107.5 $\pm$ 4.4
C17	80	120	280	0.2	114.3 $\pm$ 4.9
C18	55	110	260	0.2	112.8 $\pm$ 5.7
C19	55	110	260	0.3	102.5 $\pm$ 4.5

Table 15: Regression model based on the CPO results.

Regression equation				
UTS [MPa] = -12.4 + 0.507T_{ext} + 0.2047T_{bed} + 0.43v + 580h - 0.00294T_{ext}v - 2.687T_{ext}h - 7.60vh + 0.0328T_{ext}vh				
S [MPa]	R-sq	R-sq(adj)	R-sq(pred)	Lack-of-fit (p-value)
5.410	71.26 %	68.35 %	63.92 %	0.193

Based on the regression equation presented in Table 15, the two maxima of the function given by the regression equation (and therefore the points of highest predicted UTS according to the model) were used to create two sets of parameters, with which extra samples were 3D-printed and tested. The results from the tensile tests performed with the samples printed with these two parameter sets are presented in Table 16. It was confirmed that C_{opt1} leads to the highest tensile strength values with an average of 117.1 ± 6.1 MPa as opposed to 112.1 ± 3.6 MPa for C_{opt2} (cf. Table 16). Therefore, the parameter values of C_{opt1} were used for all further experiments as well as for the comparison of the influence of the different printing bed materials.

Table 16: Printing parameters and results of the optimised conditions.

Condition	Printing Speed	Bed temperature	Nozzle temperature	Layer height	Predicted UTS	Experimental UTS
	v [mm/s]	T_{bed} [°C]	T_{ext} [°C]	h [mm]	R_m [MPa]	R_m [MPa]
C_{opt1}	30	120	280	0.2	117.36	117.1 $\pm$ 6.1
C_{opt2}	80	120	280	0.2	113.54	112.1 $\pm$ 3.6

For the optimised condition C_{opt1}, the values were consistently 13.5 % higher than the average UTS of 103.2 MPa of 3D-printed parts that the filament supplier reports [21]. The distribution of the results that were achieved with the samples printed at that optimised condition is shown in Figure 22 as well as the confidence and prediction intervals, which were calculated with Minitab in the optimisation process.

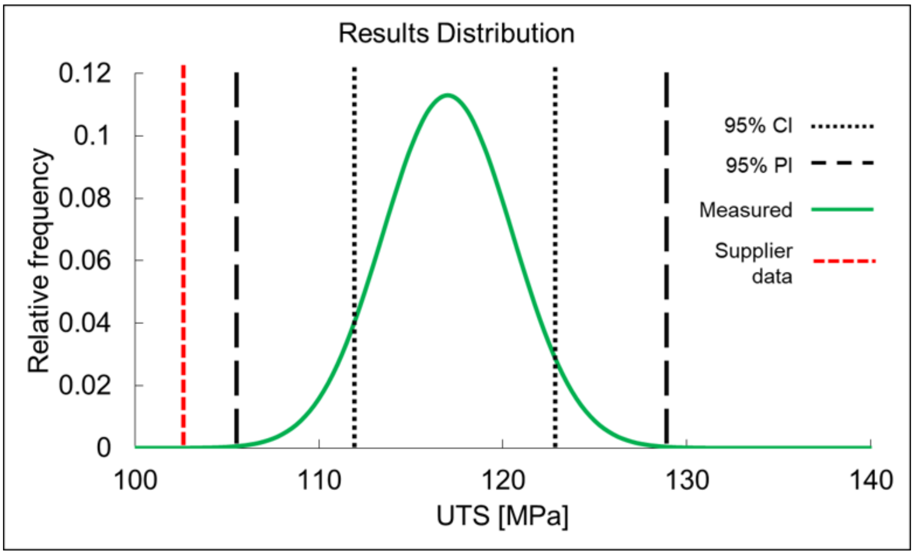

Figure 22: Distribution of the results that were achieved with the samples printed at the optimised condition C_{opt1} (green curve) as opposed to the guaranteed value by the manufacturer when applying the recommended printing parameters/parameter ranges (red line). CI = confidence interval; PI = Prediction interval.

5.2.1 General aspects

From a general observation, the samples showed a brittle behaviour. Although the values were different, the shape of the force-displacement-curve was similar for all of them. A representative curve is shown in Figure 23, the remaining curves can be found in the appendix (Appendix I). However, evidence of crazing could be found at the fracture surfaces of CPO samples. Crazing happens prior to failure in polymers when tensile stress is applied and leads to the formation of microvoids [36]. Fibrils (marked by yellow arrows in Figure 24) of plastically deformed polymer chains form between the faces of the microvoid [36]. Therefore, they indicate that some ductile deformation took place as well. The fibrils are formed in the direction of the applied stress and stabilise the microvoids [37]. A schematic illustration of crazing is shown in Figure 25.

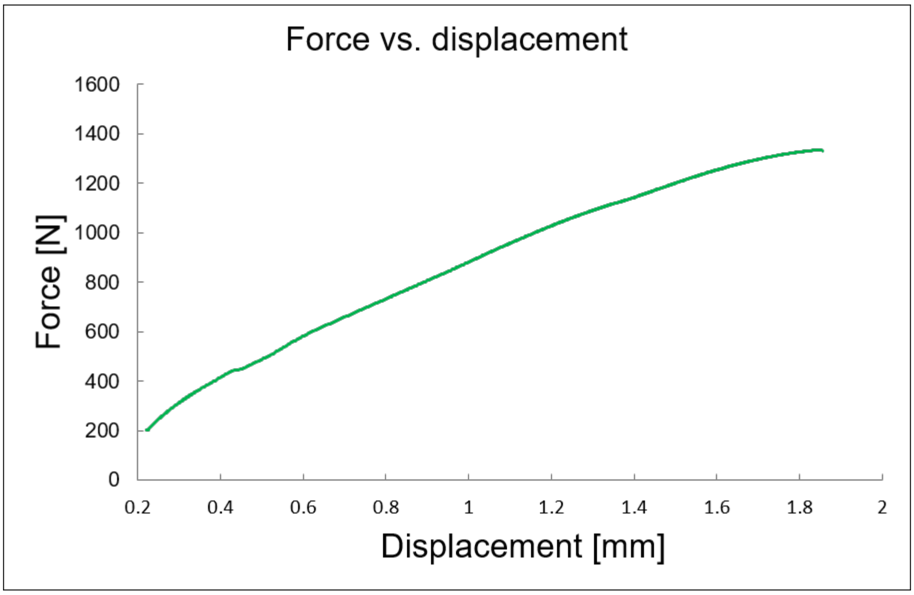

Figure 23: Force-displacement curve of a C16 sample.

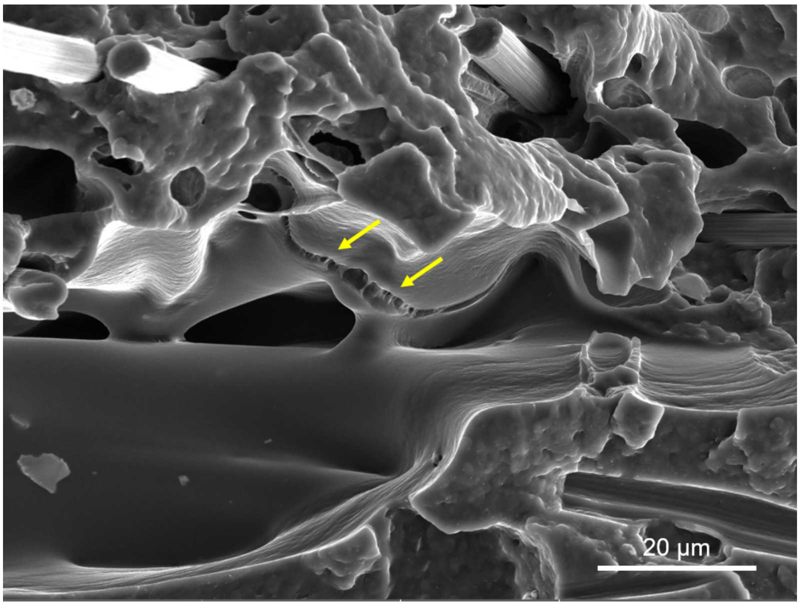

Figure 24: SEM micrograph of a CPO sample, the yellow arrows mark fibrils.

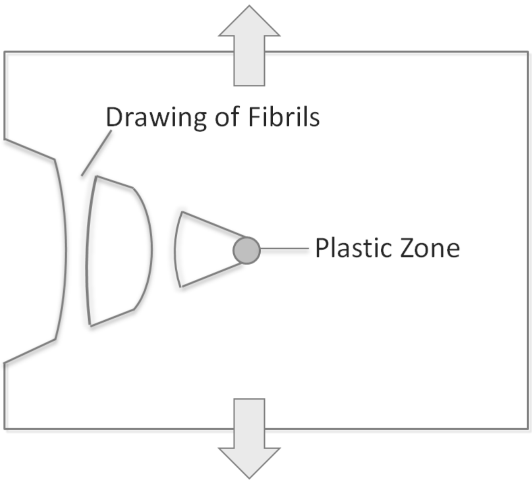

Figure 25: Schematic illustration of crazing. Reproduced from [37].

Several aspects that were generally observed help to understand the behaviour that the tensile test samples of the composite part optimisation showed. For instance, after printing, the fibres appear aligned along the printing direction and hence, the material is anisotropic within a layer. Therefore, when looking at the fracture surface, most fibres of the 0°-layers appear perpendicular to the view plane while the fibres of the 90°-layer lie mostly horizontally in the view plane. The same applies to pores within the roads, which were already present in the filament prior to printing (see Section 3.6.2) and after printing also appear aligned along the printing direction (see Figure 26).

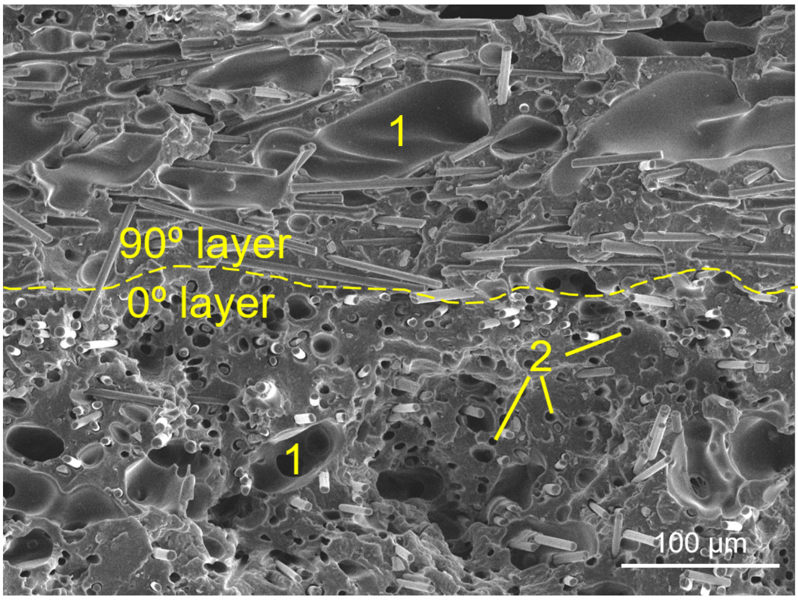

Figure 26: Representative image of the fracture surface of a CPO tensile sample. The yellow dashed line marks the interface between a 0°- and a 90°-layer. ”1” indicates pores that originate from filament fabrication. Voids due to fibre pull-out are shown by ”2”.

Additionally, voids (smaller than the pores mentioned before) can be identified when looking at the fracture surface (see Figure 26). They were produced by fibre pull-outs that happened during the tensile test and are especially noticeable in the 0°-layers, since in those layers the fibres were aligned along the tensile stress direction. As in this case, the crack propagation occurred perpendicularly to the fibre orientation, the fibres either broke or debonded from the matrix and were pulled out.

According to the Cook-Gordon model for longitudinal splitting, there are three main mechanisms which can occur [36]. The dominating mechanism depends on the interaction between fibre and matrix [36]. If the interaction is very strong, the fibre will not debond from the matrix and break instead (Figure 27(a)) [36]. If the interaction is weaker, the fibre will still break but only after partly debonding (Figure 27(b)) [36]. If the interaction is very weak, no fibre breakage will occur and after considerably debonding, the fibre pulls out instead (Figure 27(c)) [36]. For of all three mechanisms, evidence can be found when inspecting the fracture surface of the 0° layers (see Figure 27). However, the fibre pull-outs appear predominantly and therefore indicate a weak fibre/matrix interaction. This is probably due to the chemically inert surface of carbon fibres which makes it hard for the thermoplastic matrix to impregnate the fibres [38, 39]. The weak carbon fibre/PA matrix interaction has been reported by many other studies as well [40–42].

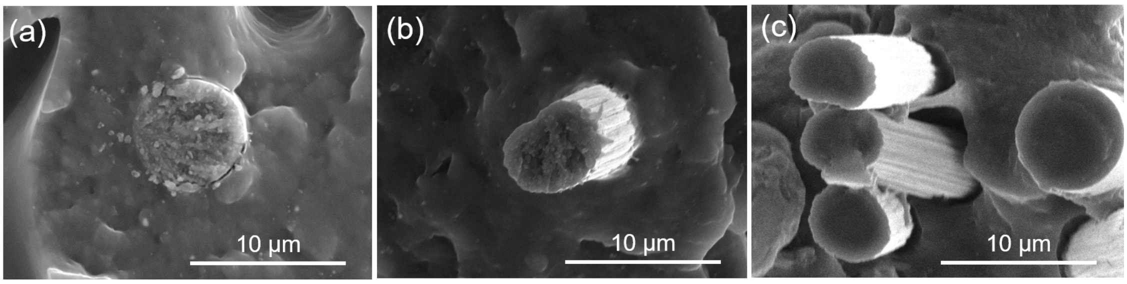

Figure 27: Failure mechanisms observed in 0º-layers. (a) Fibre breakage; (b) Limited debonding leading to breakage; (c) Extensive debonding leading to fibre pull-out.

In the case of the 90° layers, the fracture surface appears more plain which indicates a crack propagation at lower energies than in the 0° layers [36]. This is a reasonable assumption, since the crack propagation occurred parallel to the fibre orientation in this case. Due to the weak fibre/matrix interaction, (semi-)debonded fibres as well as remaining imprints from detached fibres could be identified also in the case of the 90° layers (see Figure 28).

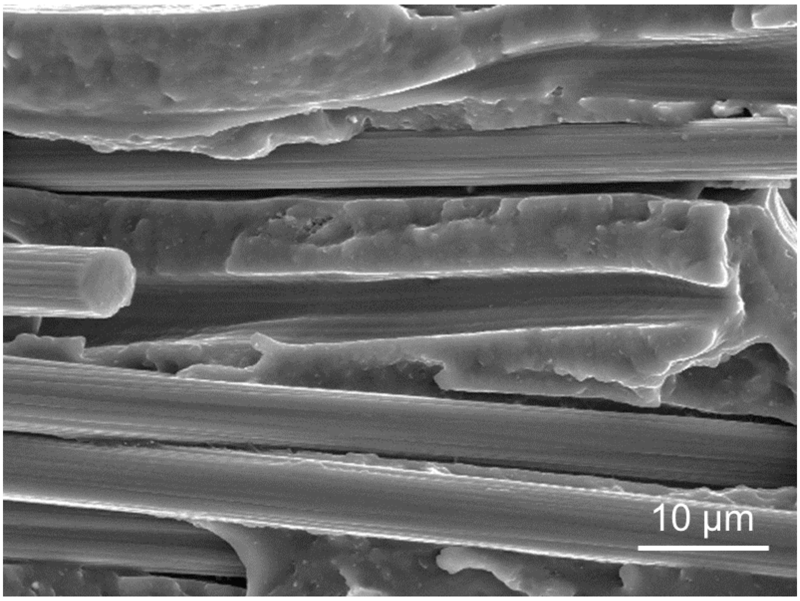

Figure 28: Debonding fibres and remaining imprints observed in 90º-layers.

5.2.2 Influence of the process parameters on the mechanical performance

The influence of the different printing parameters regarding the mechanical properties of the samples is illustrated in Figure 29.

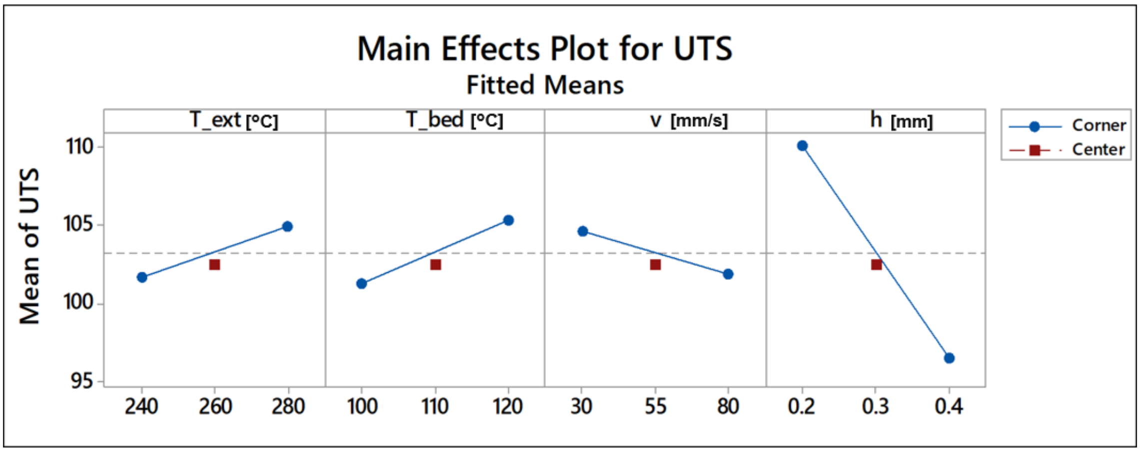

Figure 29: Main effect plot of the influence of the investigated process parameters on the UTS.

The effects of the different process parameters and their significance are summarized in the normal plot of the standardized effects (see Figure 30). In this diagram, the diagonal line represents a distribution fit line for the case the when the effects are zero. The factor is considered statistically significant if it is placed within a certain distance from this line. This distance is based on a significance level (α) of 0.05. In order to facilitate the results interpretation, only the parameters and parameter combinations which have a significant effect on the ultimate tensile strength are labeled, being represented by black squares in the diagram. Points to the left of the distribution fit line denote negative effect on the UTS, whereas points to the right denote positive effect. The further the point is away from the fit line, the stronger is the effect on the response. These last two remarks can be also observed in a Main Effects plot, see Figure 29.

From the normal plot of standardized effects, it can be observed that the printing speed is the only parameter which does not have a statistically significant effect as a main effect. However, it is significant in combination with other parameters (two- and three-way interactions). For the bed temperature, the opposite is true: it is the only independent parameter, meaning that is not involved in any two- or three-way interactions. This seems reasonable considering that it is the only parameter that is neither related to the nozzle temperature nor to its position. Moreover, the layer height has the largest influence on the UTS. The effects of the different parameters on the UTS are explained in more detail in the following sections.

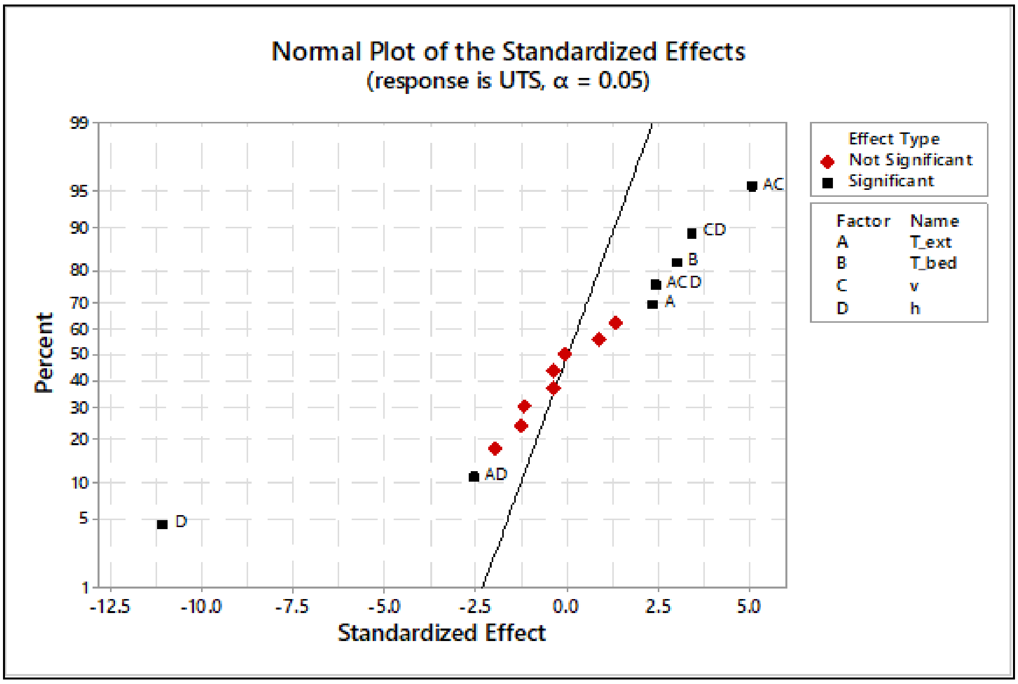

Figure 30: Normalized plot of standardised effects of the composite part optimisation.

5.2.2.1 Layer height, *h*

As the standardized effect of the layer height is negative, a higher layer height leads to a lower UTS. When decreasing the layer height from 0.4 mm (C6) to 0.2 mm (C15), while all other parameters remain the same, the ultimate tensile strength increases by 30.8 % from 89.5 ± 6.6 MPa to 117.1 ± 6.1 MPa. The tensile strength is probably related to the presence of pores in the sample: the more pores there are, the weaker the material becomes. On the macroscopic photos (Figure 31), one can see that the void content is increasing with an increasing layer height. This is in agreement with the literature [43–47]. Garzon-Hernandez *et al.* [44] found a 14 % decrease of maximum stress and an increasing void content when increasing the layer height from 0.1 mm to 0.2 mm for ABS. Wang *et al.* [45] found that for CF- and GF-reinforced PEEK, the flexural strength decreases by 14 % with the layer thickness increasing from 0.1 mm to 0.3 mm. For a layer thickness of 0.3 mm they found more pores and clear layer interfaces which led to a worse bonding. They also observed a squeeze effect by the nozzle for layer thicknesses of 0.1 mm which led to stronger bonding [45]. Additionally, the diameter of an extruded polymer is usually larger than the diameter of the extruder, i.e. the nozzle due to the die swell effect [48]. This phenomenon might further increase any squeezing effect taking place [48].

Nomani *et al.* [46] also found that for ABS, an increasing layer thickness leads to a decrease in the tensile strength. They correlated this behaviour to a larger observed amount of micro-porosity and a weaker interlayer bond strength in the samples with a larger layer thickness. Due to the brittle failure modes of the samples, Nomani *et al.* [46] suspected that the present porosity functioned as a starting point for crazing failure followed by layer delamination upon loading. They suggested the combination of three effects to contribute mainly to the influence of the layer height: porosity, number of deposited layers and strain hardening [46].

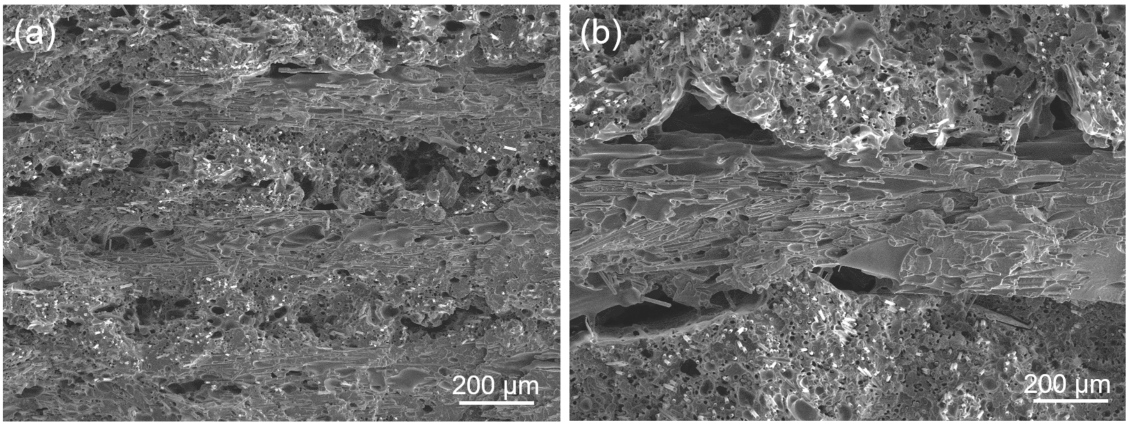

Figure 31: SEM Micrographs of C15 (h = 0.2 mm) (a) and C6 (h = 0.4 mm) (b).

Moreover, the resulting pores are generally much more pronounced in the bottom of each 0° layer than in their top. This is especially noticeable in the samples with a layer height of 0.4 mm (see Figure 32).

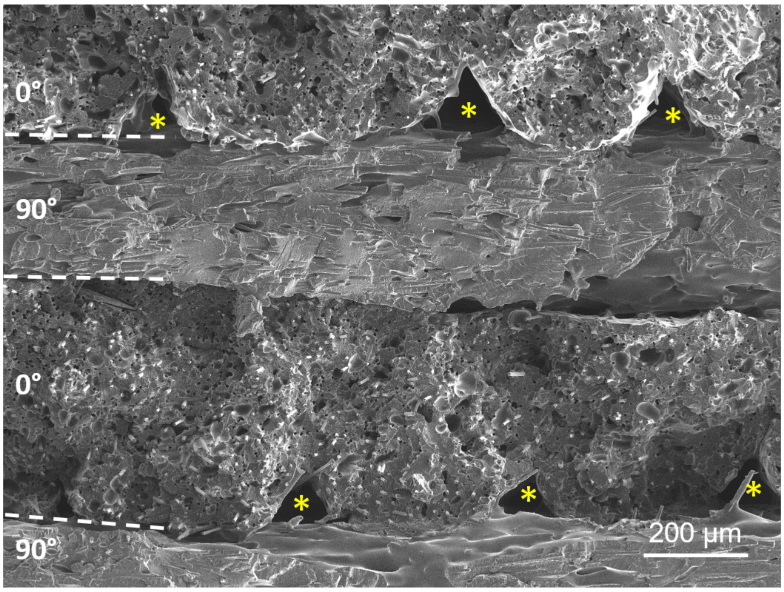

Figure 32: SEM Micrograph of a sample with a layer height of 0.4 mm, yellow stars mark gaps between the roads.

An explanation for the effect could be the reheating effect of the nozzle when it passes nearby again, e.g. during the deposition of the next layer (called ”Heat build-up”, see Figure 33). Naturally, larger roads (i.e. with a higher layer height) experience less reheating in the bottom than smaller ones (i.e. with a smaller layer height) since there is more material between the heat source and the bottom of the road. Consequently, layers with a larger layer height might solidify faster at the bottom and have therefore less time to fill the gaps. As the bottom part of the layers with a layer height of 0.2 mm is much closer to a recurring nozzle, those layers experience a larger heat build-up all the way down to the bottom of that layer and even the interface below might still be affected. This would then not only reduce the number and size of the pores but also enhance the interlayer bonding directly.

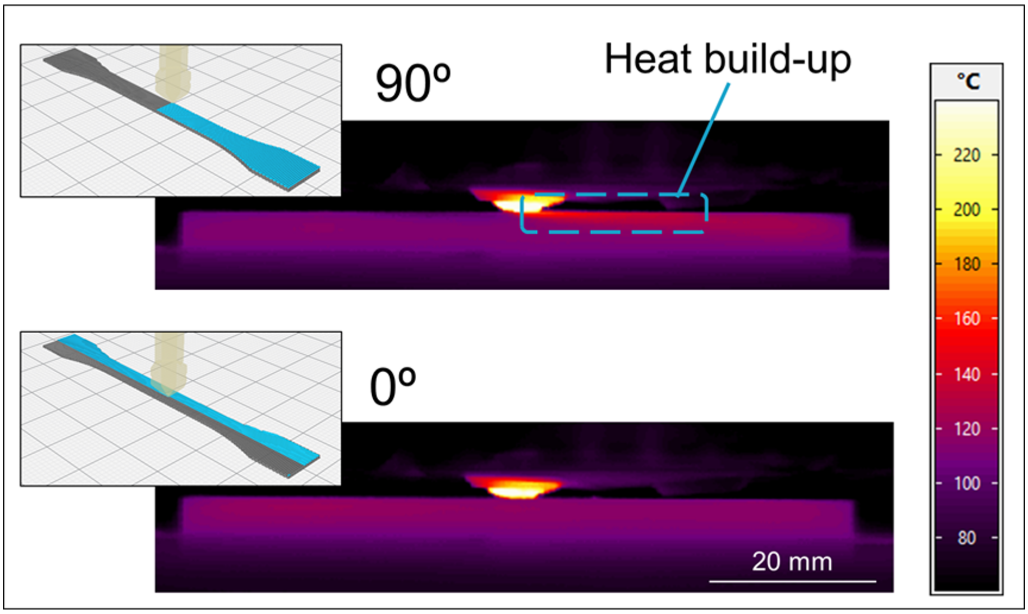

Figure 33: Thermographic measurements during the deposition of 90 ° and 0 ° layers.

5.2.2.2 Nozzle temperature, T_{ext} and bed temperature, T_{bed}

Lower T_{ext} and lower T_{bed} had a very similar effect and C11 (T_{ext} = 240°C, 112.0 MPa) and C14 (T_{bed} = 100°C, 112.3 MPa) lead to very similar results in the tensile tests. In both cases, the tensile strength was about 4 % lower than for the optimised condition C_{opt1} (T_{ext} = 280°C and T_{bed} = 120°C, 117.1 MPa). As these parameters had only a very slight influence on the UTS, it is difficult to find evidences justifying this small influence on the results. However, there may be a worse interlayer bonding at lower bed and extrusion temperatures as has been found in other studies which will be referred to in more detail in the upcoming sections [45, 49].

In the overview of the fracture surfaces, it is visible that in general, the interlayer bonding seems to be worse between 90°/0° (bottom/top, marked with red lines) than between 0°/90° (bottom/top, marked with yellow dotted lines) layers (see Figure 34) which was already explained in Section 5.2.2.1. Further individual details on the influence of each of the two parameters are addressed in the upcoming sections.

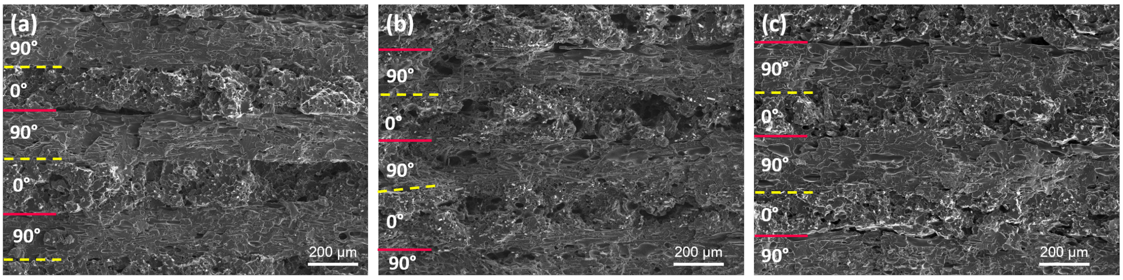

Figure 34: SEM overview of fracture surfaces from selected tensile test specimens printed at condition C11 (T_{ext} = 240°C and T_{bed} = 120°C) (a), C15 (T_{ext} = 280°C and T_{bed} = 120°C) (b) and C14 (T_{ext} = 280°C and T_{bed} = 100°C) (c). 90°/0° (bottom/top) interfaces are marked with red lines, 0°/90° (bottom/top) interfaces are marked with yellow dotted lines.

5.2.2.2.1 Nozzle temperature, T_{ext}

The results of the thermographic analysis reveal that a higher nozzle temperature does not change the thermal gradients within the deposited roads during the printing process but rather lead to a shift of the whole distribution curve to higher temperatures. Therefore, at higher nozzle temperatures, the roads are not only printed at a higher temperature but also stay at an elevated temperature for longer after being deposited and have therefore more time to fill gaps before solidifying.

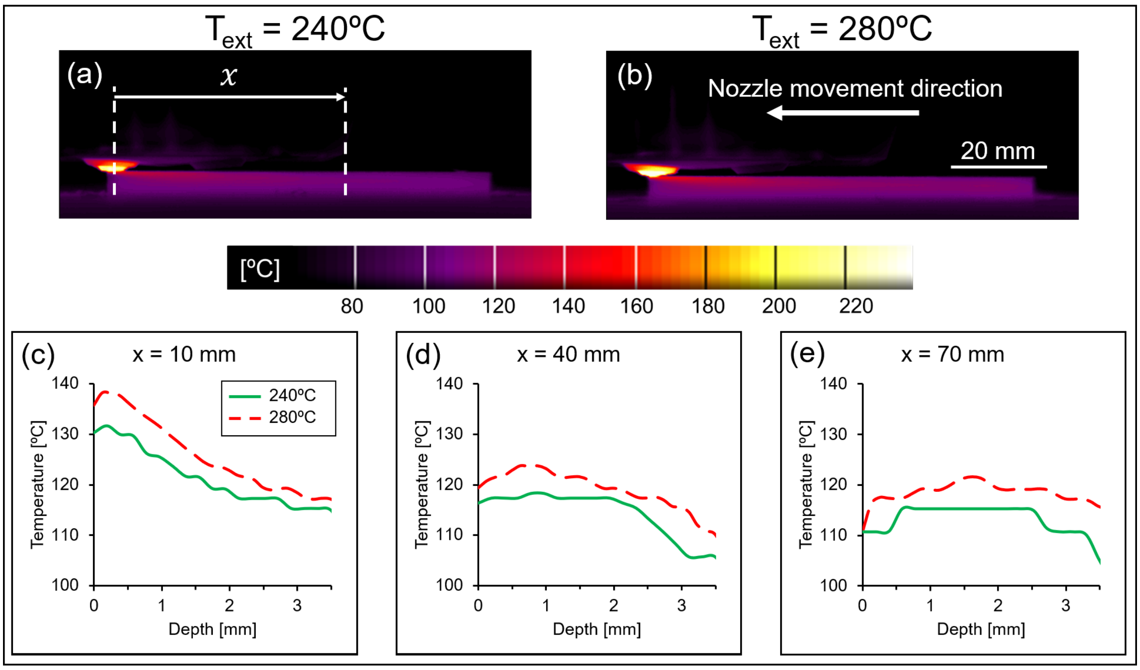

Figure 35: Top: Thermographs during the printing process of C11 (T_{ext} = 240°C, a) and C15 (T_{ext} = 280°C, b); Bottom: Temperature over depth at x = 10 mm (c), x = 40 mm (d) and x = 70 mm (e) distance from the nozzle.

Similar conclusions were drawn by Ding *et al.* [49] who found that for PEEK and PEI, the tensile strength decreases when the nozzle temperature is increased from 360°C to 380°C (PEEK)/ 390°C (PEI) but increases and reaches the highest values when further increasing the nozzle temperature to 420°C. The authors suggest that the high tensile strength for printing with nozzle temperatures of 420°C is due to a fuller melting of the polymer and therefore a better interlayer bonding. Micrographs of the fracture surfaces revealed the presence of large pores in the samples printed at 370°C as opposed to more abundant but smaller pores in those printed at 380°C and 390°C [49]. In the samples printed at 420°C, both, the amount as well as the size of pores was smaller [49]. Ding *et al.* [49] therefore concluded that the many small pores at 380/390°C represent more possible starting points for cracks and therefore a lower tensile strength while the vanishing of pores at higher temperature led to a much higher tensile strength [49].

Wang *et al.* [45] found that for PEEK, CF-PEEK and GF-PEEK, the tensile strength increased when increasing the nozzle temperature from 400°C to 440°C. Correspondingly, they state that it is easier to tell apart the single layers from each other at lower nozzle temperatures because the bonding is worse. The authors suggest that the interlayer bonding is better at higher nozzle temperatures due to better fluidity and formability of the material. They also observed better adhesion between the fibres and the matrix when the nozzle temperature was higher. Wang *et al.* [45] found pores in the fracture surface but attributed them mostly to fibres pulling out rather than to the FFF process [45].

Furthermore, Skaskevich *et al.* [50] showed that an increase of the nozzle temperature from 240°C to 265°C leads to a higher tensile strength in PA-samples which were produced using FFF.

5.2.2.2.2 Bed temperature, T_{bed}

The bed temperature is the only investigated parameter which is independent from the other varied process parameters as it is not directly related to the nozzle temperature or its position. This might be responsible for its absence in all of the statistically significant two- and three-way interactions. The similarity between the effect of the bed temperature and that of the nozzle temperature is also present in the results of the thermographic analysis (see Figure 36). Again, the curves are shifted to higher temperatures when the bed temperature is increased. However, in the case of the bed temperature, the effect is stronger, which seems reasonable since the bed transfers heat to the whole area of sample from below while the nozzle is a much more local heat source. If the bed temperature is higher, the polymer remains for longer at a higher temperature. Therefore, the polymer remains for longer at optimal sintering conditions. Consequently, the deposited roads have more time to flow and bond with the previous layers, as well as with the adjacent roads before solidifying.

In addition to the temperatures being higher in general, also the shape of the cooling curves changes when altering the bed temperature (unlike in the case of the different nozzle temperatures seen in the previous section). When the bed temperature is higher, not only the initial temperature of the deposited road is higher but it also cools down slower. This can also be seen in Figure 36 and especially notable in the right hand side of the diagrams. This effect helps additionally to keep the polymer at better sintering conditions than when using lower bed temperatures.

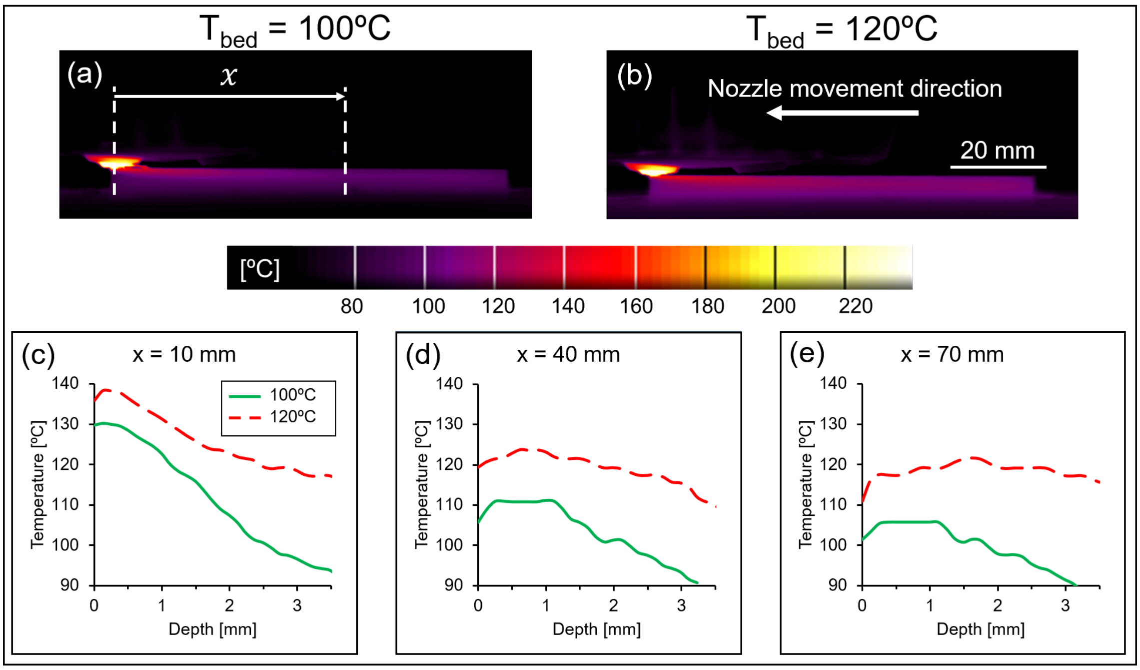

Figure 36: Top: Thermographs during the printing process of C14 (T_{bed} = 100°C, a) and C15 (T_{bed} = 120°C, b); Bottom: Temperature over depth at x = 10 mm (c), x = 40 mm (d) and x = 70 mm (e) distance from the nozzle.

A decreased pore size as well as an increased interlayer bonding was reported by Wang *et al.* [45] for PEEK, CF-PEEK and GF-PEEK when increasing the bed temperature from 240°C to 280°C. The concomitant increasing tensile strength, which was found was associated directly with those microstructure improvements [45]. At lower bed temperatures, Wang *et al.* [45] observed delamination and warpage during the printing process due to bad adhesion [45].

5.2.3 Two-/Three-way interactions

Several two- and three-way interactions have been found but more research would be necessary to understand and explain them thoroughly.

For example, the combination of an increased nozzle temperature together with a faster printing speed correlates with a higher UTS according to the statistical analysis. A possible explanation could be that a faster printing speed implies less time for the polymer to cool down before the next layer is deposited. If the nozzle temperature is high enough, the polymer might never go below a critical temperature that is necessary for the deposited road to chemically bond with adjacent roads. If on the other hand, the nozzle temperature is so low that the polymer of the deposited road never remains above that critical temperature for long enough to bond, the effect is irrelevant.

5.2.4 Printing bed material study

In addition to the CPO, a printing bed material study was conducted. The results of the comparison of the different printing bed materials are displayed in Table 17.

Table 17: Printing parameters of the tested conditions.

Condition	Printing bed material	UTS
		R_m [MPa]
C15	Glass	117.1 ± 6.1
C20	Aluminium	83.0 ± 4.9
C21	Al + 1 PI tape layer	83.2 ± 9.0
C22	Al + 2 PI tape layers	87.2 ± 4.0
C23	Al + 3 PI tape layers	86.6 ± 4.4
C24	Al + 4 PI tape layers	84.0 ± 9.0

The table shows that the tensile strength of the samples printed on glass (117.1 MPa) was 41 % higher than of those printed on aluminium (83.0 MPa). Adding PI tape layers on the aluminium neither increased nor decreased the mechanical performance in comparison to the bare aluminium sample.

During the printing, there is no difference in the temperature distribution when using different printing bed materials since the temperature of the printing bed (120°C) and the nozzle (280°C) remain constant. This was also verified by the thermographic measurements (Figure 37).

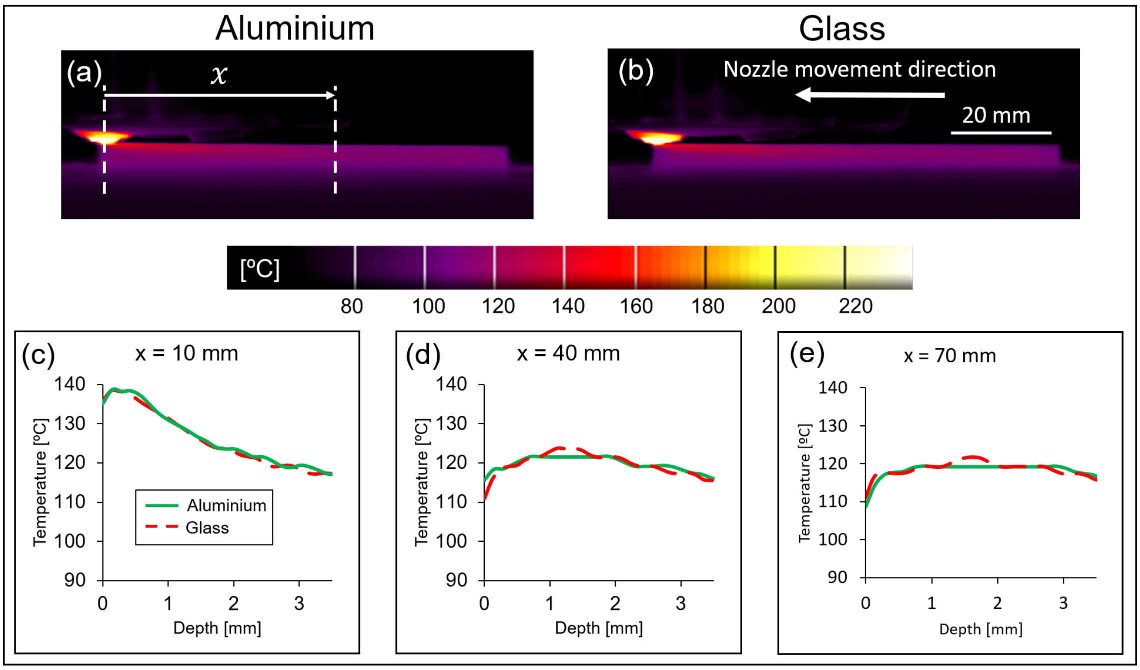

Figure 37: Thermographic measurements during the printing process on glass and aluminium (Top) and Temperature between point A and B at different distances X from the nozzle (Bottom).

However, after printing, the samples printed on aluminium on average cool down 36 % faster than those printed on glass (cf. Figure 38). This is because the thermal conductivity of aluminium (228 W/mK) is significantly higher than the one of glass (2 W/mK) [51]. The faster cooling may have led to higher residual stresses in the part and therefore to lower mechanical properties. Nevertheless, more evidence is required to be able to properly describe this phenomenon.

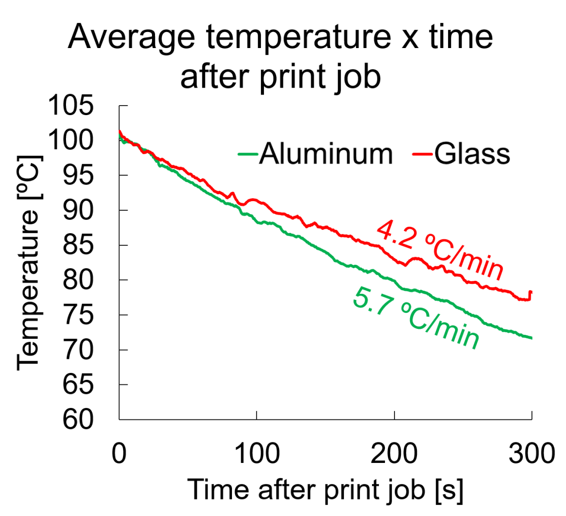

Figure 38: Temperature evolution of samples after the printing process is finished.

In the SEM micrographs shown in Figure 39, a worse interlayer bonding in the samples printed on aluminium (a) compared to those printed on glass (b) is clearly visible. The interlayer bonding appears better in the first printed layers than in those printed later. This seems to correlate with temperature distribution within the layers. While the first layers are reheated by the ones deposited on top of them, the last layers do not experience this effect. Therefore, the first layers were kept above a certain temperature threshold for a longer interval than the last ones (Figure 33).

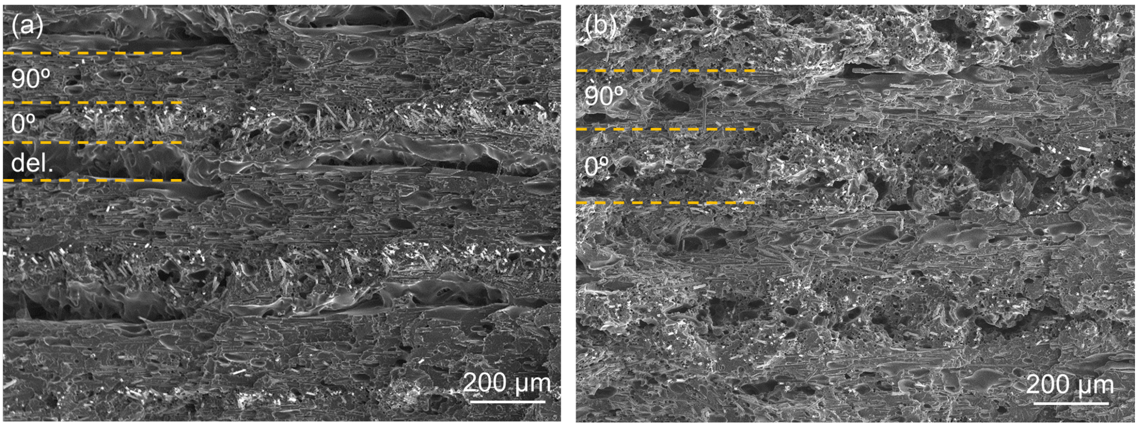

Figure 39: SEM pictures of selected specimen fracture surfaces printed on aluminium (a) and glass (b). The dashed yellow lines represent layer boundaries; del. marks delamination.

Another issue is the orientation of the roads: the delamination is especially pronounced in the 90°/0° (bottom/top) interfaces (Figure 33 and Figure 40). This can be explained by the nozzle movement patterns. The 90° roads are significantly shorter than the 0° roads and therefore, the hot nozzle stays close to one place for longer and thus enhances reheating of the bonding area more. Thermographic measurements confirmed a higher heat build-up when printing the 90° layer compared to the deposition of the 0° layers (see Figure 33 in Section 5.2.2.1).

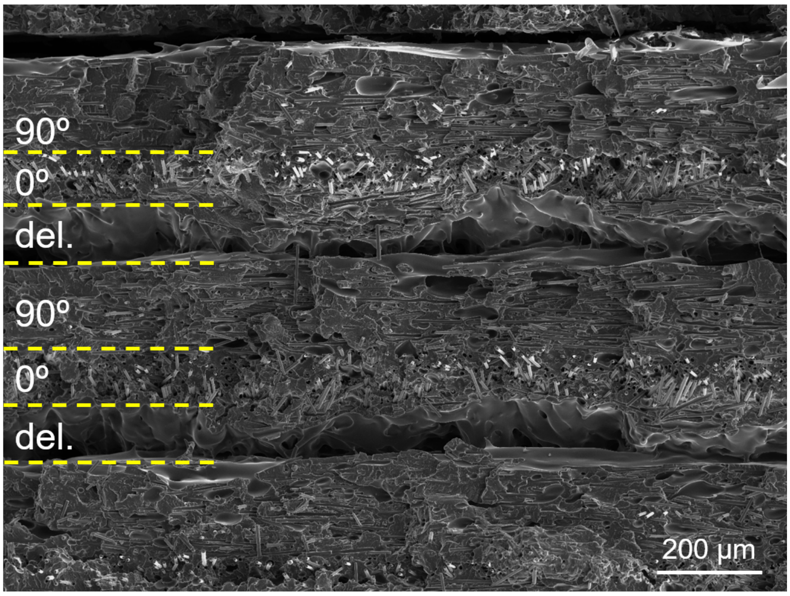

Figure 40: SEM micrograph of a sample with especially pronounced delamination in the 90°/0° (bottom/top) interfaces.

5.3 Coating layer optimisation - OFAT

In Figure 41, the top view of an untested CLO sample is shown. The results of the coating layer optimisation are displayed in Table 18.

Figure 41: Top view of an untested CLO sample.

Table 18: Results of the tested coating layer optimisation conditions with 12.5 mm overlap; A-M = Adhesive failure at the Ti-6Al-4V/PA interface, A-P = Adhesive failure at the PA/PA-CF interface, NT = Net-tension failure within the composite part (PA-CF); dominant failure type is in bold letters.

Condition	Printing Speed	Nozzle temperature	Bed temperature	Coating layer height	ULSS	Failure type
	v [mm/s]	T_{ext} [°C]	T_{bed} [°C]	h [mm]	R_m [MPa]	
C1	5	280	150	0.1	3.4 ± 1.4	A-M, **A-P**
C2	20	280	150	0.1	6.2 ± 1.3	A-M, **A-P**
C3	50	280	150	0.1	8.4 ± 0.7	NT, **A-M, A-P**
C4	50	240	150	0.1	5.4 ± 1.3	**A-M**
C5	50	260	150	0.1	8.6 ± 1.3	NT, **A-M, A-P**
C6	50	260	120	0.1	Untested	-
C7	50	260	100	0.1	Untested	-
C8	50	260	140	0.1	7.8 ± 0.8	**NT**
C9	50	260	150	0.2	8.7 ± 1.3	**NT**
C10	50	260	150	0.3	8.0 ± 2.6	NT, **A-M**

Three different types of failure could be distinguished for the coating layer optimisation samples:

- Adhesive failure between the metallic substrate (Ti-6Al-4V) and the coating layer (PA) (A-M)
- Adhesive failure between the coating layer (PA) and the composite part (PA-CF) (A-P)
- Net-tension (adherend) failure within the composite part (PA-CF) (NT)

For some samples, also mixed failure types occurred but a predominant type could always be identified. Figure 42 shows a graphic representation of those. The net-tension failure occurred when the joint area was stronger than the composite part. Therefore, the stronger the interface was, the more likely it was to fail in net-tension. In order to be able to properly compare the strength of the joint area, the net-tension failure was avoided. As the printing parameters of the composite part were already optimised to guarantee a strong polymer there, additionally, the overlap length L was reduced from 12.5 mm to 6mm. Based on what is known for adhesive joints, the reduced overlap length promotes an adhesive failure due to smaller stress peaks which are produced by the load transfer in the joint area [52].

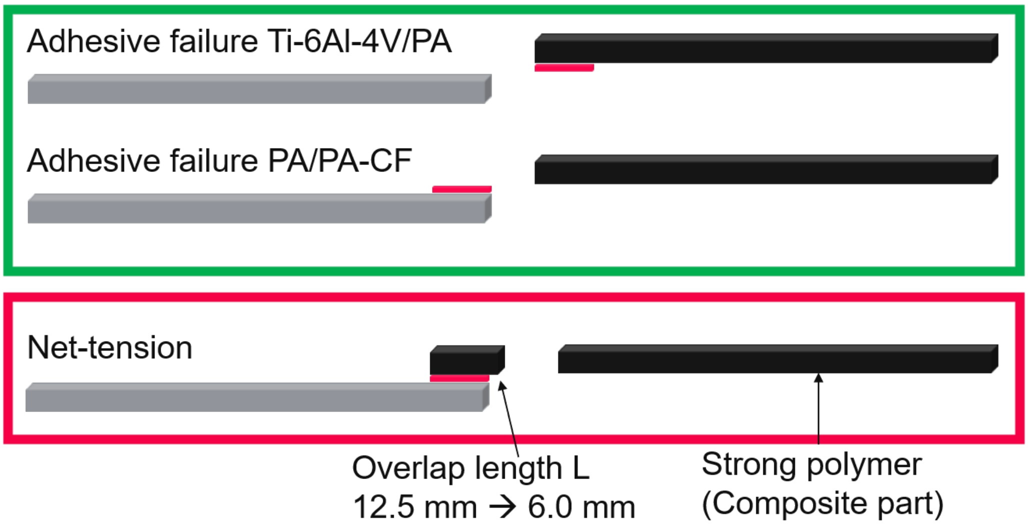

Figure 42: Schematic representation of the different types of failure which occurred for the coating layer optimisation samples.

As opposed to the UTS results of the composite part optimisation, the results of the ANOVA performed on the coating layer optimisation samples show that for the coating layer, the printing speed is the only parameter of statistical significance concerning its influence on the ULSS (see Table 19) in the studied range of process parameters. However, even with considering the optimised printing parameters for the PA-CF, net-tension failure still occurred for conditions C3, C5, C8, C9 and C10. Therefore, there corresponding ULSS values were capped around 8 MPa which is in the range of the maximum load the PA-CF can withstand before failing. Hence, the ANOVA results (Table 19) for those samples are not representative since the difference of the tested conditions could not be properly assessed as the interfacial area was not successfully tested.

Table 19: ANOVA results for the coating layer optimisation samples printed with an overlap length of 12.5 mm.

Parameter	Level 1	Level 2	Level 3	F	P-value
Printing speed [mm/s]	5	20	50	9.04	0.015
Nozzle temperature [°C]	240	260	280	4.81	0.056
Bed temperature [°C]	140	150	-	0.67	0.458
Coating Layer height [mm]	0.1	0.2	0.3	0.07	0.927

Thus, conditions for which a net-tension was obtained were reprinted and retested at the reduced overlap length of 6 mm, which allowed them to fail at lower loads (below the maximum load that the composite could withstand) and therefore promoted adhesive failure. As the influence of the printing speed could already be evaluated in the previous experiments, this parameter was not considered in these following experiments anymore.

In the case of the bed temperature, 100°C, 120°C and 150°C should have been tested at 12.5 mm overlap; however, the only condition which could be successfully printed was the one with T_{bed} = 150°C, while the coating layer samples printed at lower temperatures failed before they could be mechanically tested (see Figure 43). Therefore, another condition with T_{bed} = 140°C was tested and was successfully printed.

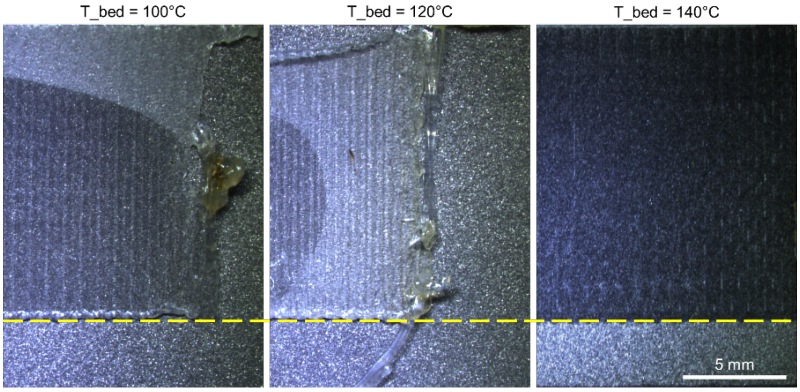

Figure 43: Failure in the coating layer of samples printed at T_{bed} = 100°C and 120°C in comparison to a successful one printed at T_{bed} = 140°C.

However, net-tension failure occurred in both cases. Consequently, the bed temperature was tested again at 6 mm overlap (C13 and C14), at which both conditions reached a very similar ULSS. The following tests were performed at T_{bed} = 150°C. This was already discussed for the CPO in Section 5.2.2.2 and was also found in other studies [45].

The results of the tested coating layer optimisation conditions with 6 mm overlap are displayed in Table 20.

Table 20: Results of the tested coating layer optimisation conditions with 6 mm overlap; A-M = Adhesive failure at the Ti-6Al-4V/PA interface, A-P = Adhesive failure at the PA/PA-CF interface, NT = Net-tension failure within the composite part (PA-CF).

Condition	Printing Speed	Nozzle temperature	Bed temperature	Coating layer height	ULSS	Failure type
	v [mm/s]	T_{ext} [°C]	T_{bed} [°C]	h [mm]	R_m [MPa]	
C11	50	280	150	0.1	9.7 $\pm$ 2.5	A-M
C12	50	260	150	0.1	6.9 $\pm$ 2.1	A-M
C13	50	280	140	0.1	9.7 $\pm$ 2.5	A-M
C14	50	280	150	0.2	14.8 $\pm$ 2.1	A-M
C15	50	280	150	0.3	17.8 $\pm$ 0.7	NT

According to the results of the ANOVA performed on these results, the layer height is the only statistically significant parameter in addition to the already assessed printing speed (see Table 21). A description of the general aspects found as well as an explanation of the effects of the significant printing parameters can be found below.

Table 21: ANOVA results for the addjoined samples printed with the reduced overlap length of 6 mm.

Parameter	Level 1	Level 2	Level 3	F	P-value
Nozzle temperature [°C]	260	280	-	1.82	0.234
Bed temperature [°C]	140	150	-	0.00	0.985
Coating Layer height [mm]	0.1	0.2	0.3	8.80	0.016

5.3.1 General aspects

Figure 44 shows a cross-sectional view of the interface between the metallic substrate and the coating layer. It can be observed that the PA of the coating layer enters the cavities and irregularities of the Ti-6Al-4V plate well. However, especially on the left side of the photo, a gap with a constant width of approx. 1.5 µm can be identified (marked by red arrows), which is in the same range as the average roughness of the sandblasted Ti-6Al-4V plates (see Section 5.1). This is probably a consequence of the sample preparation since the profile of the delaminated PA layer appears to mirror the surface profile of the Ti-6Al-4V plate. If it would be a consequence of poor wetting during the AddJoining process on the other hand, the PA profile would have to appear blunter. Another possibility is that the gap originates from the differential thermal shrinkage of both parts.

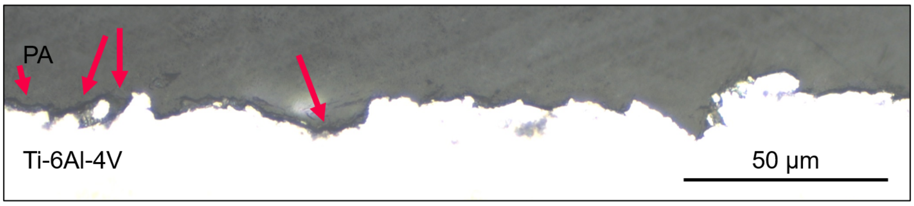

Figure 44: Cross-sectional view of the interface between the metallic substrate and the coating layer with red arrows marking a gap with a constant width of approximately 1.5 µm.

Even if the lap shear tests showed a high mechanical strength for the coating layer optimisation samples, pores are visible in the composite part. However, this is in agreement with the literature and was already discussed in Section 5.2.1.

In Figure 45, the fracture surface of a coating layer optimisation sample is shown from above. Therefore, the light grey part in the top of the image is the Ti-6Al-4V plate. From this view, one can see that many fibres are sticking out from the fracture surface of the composite part. They indicate the same fibre pull-out mechanism as in the CPO. According to the Cook-Gordon model for longitudinal splitting those fibre pull-outs are one of the three main occurring mechanisms and have already been discussed in Section 5.2.1 [36].

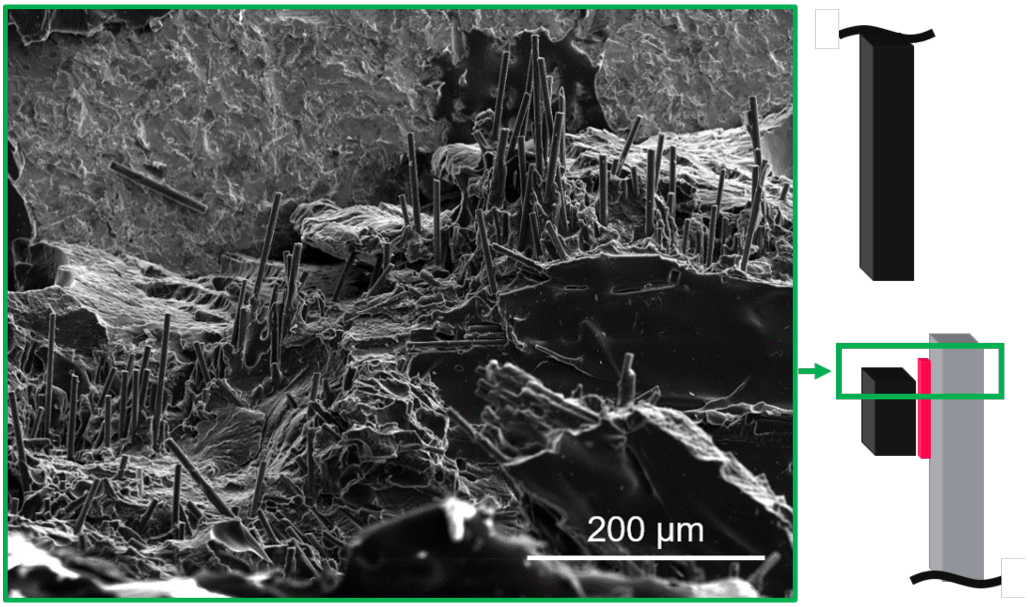

Figure 45: SEM micrograph showing a top view (green arrow shows point of view in the sketch) of a coating layer optimisation sample, fibres that stick out of the composite parts fracture surface can be identified.

Delamination between printed layers is found mostly between the coating layer and the first PA-CF layer and not between the following 15CF-PA layers (see Figure 46). This might be due to the discontinuity of the FFF process: due to software restrictions, the coating layer cools down after printing and is then heated up to 120°C again before the printing of the composite part starts.

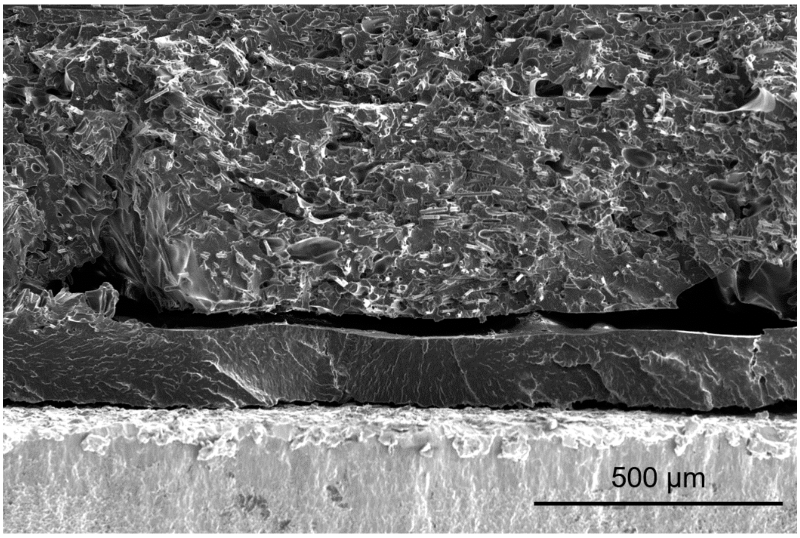

Figure 46: SEM micrograph showing of a fracture surface showing delamination predominantly between the coating layer and the composite part but also between the metallic substrate and the composite part.

Similar to the samples of the CPO, the CLO samples tested in lap shear showed mainly brittle behaviour, although evidence of a partially ductile fracture was also found when analysing the fracture surface microscopically. Figure 47 confirms that some crazing occurred at the coating layer. Due to the applied tension, some polymer chains orientated themselves in the same direction to be able to absorb the energy [53].

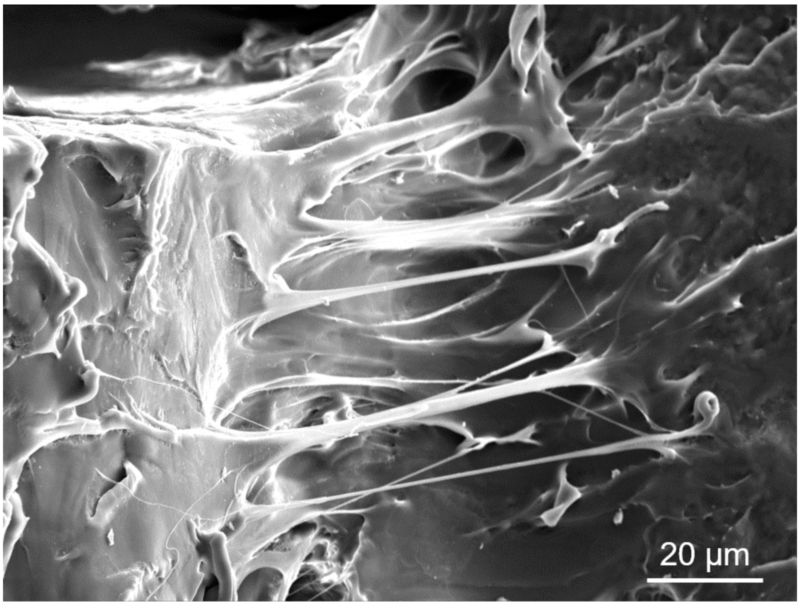

Figure 47: SEM micrograph showing traces of crazing indicating a partly ductile fracture.

In the case of an adhesive failure at the interface between the metallic substrate and the coating layer, cusps can be found on the surface of the Ti-6Al-4V plate (see Figure 48 and Figure 49). Cusps are the dominant fractographic feature of mode II (shear) fracture surfaces [36]. Figure 49(a) is taken with the BSE-detector and therefore shows more clearly the PA (dark) and the titanium (bright).

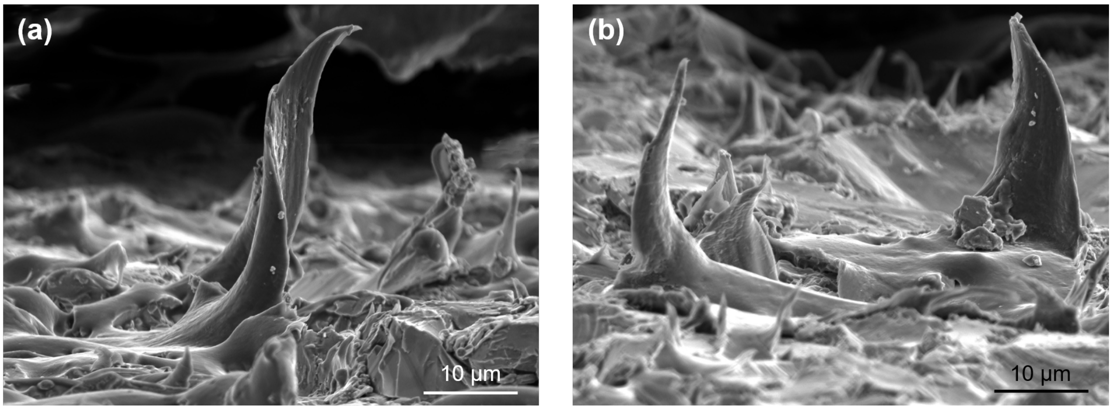

Figure 48: Both SEM micrographs show PA cusps remaining on the Ti-6Al-4V surface after fracture.

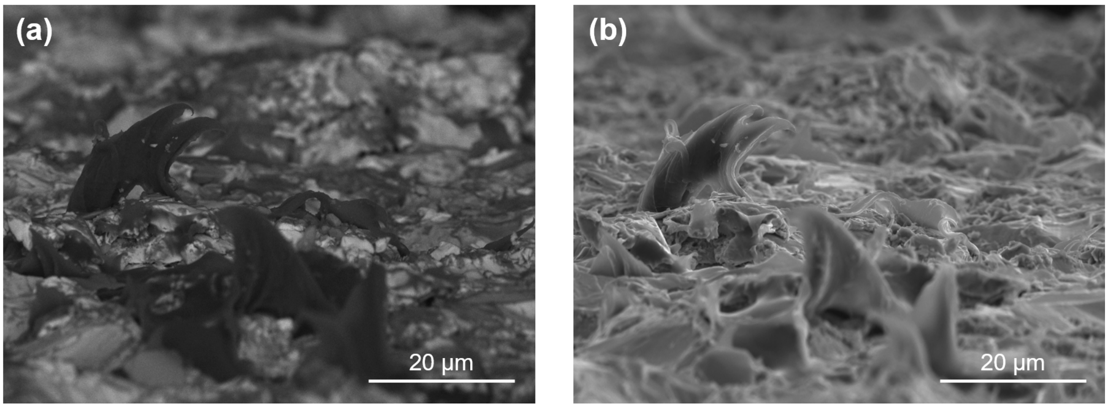

Figure 49: Both SEM micrographs show PA cusps remaining on the Ti-6Al-4V surface after fracture; (a) image taken with BSE-detector, (b) image taken with SE-detector.

Cusps were also found between the coating layer and the composite part after adhesive failure at that interface. Figure 50 shows remaining PA-CF cusps from the composite part after it detached from the coating layer.

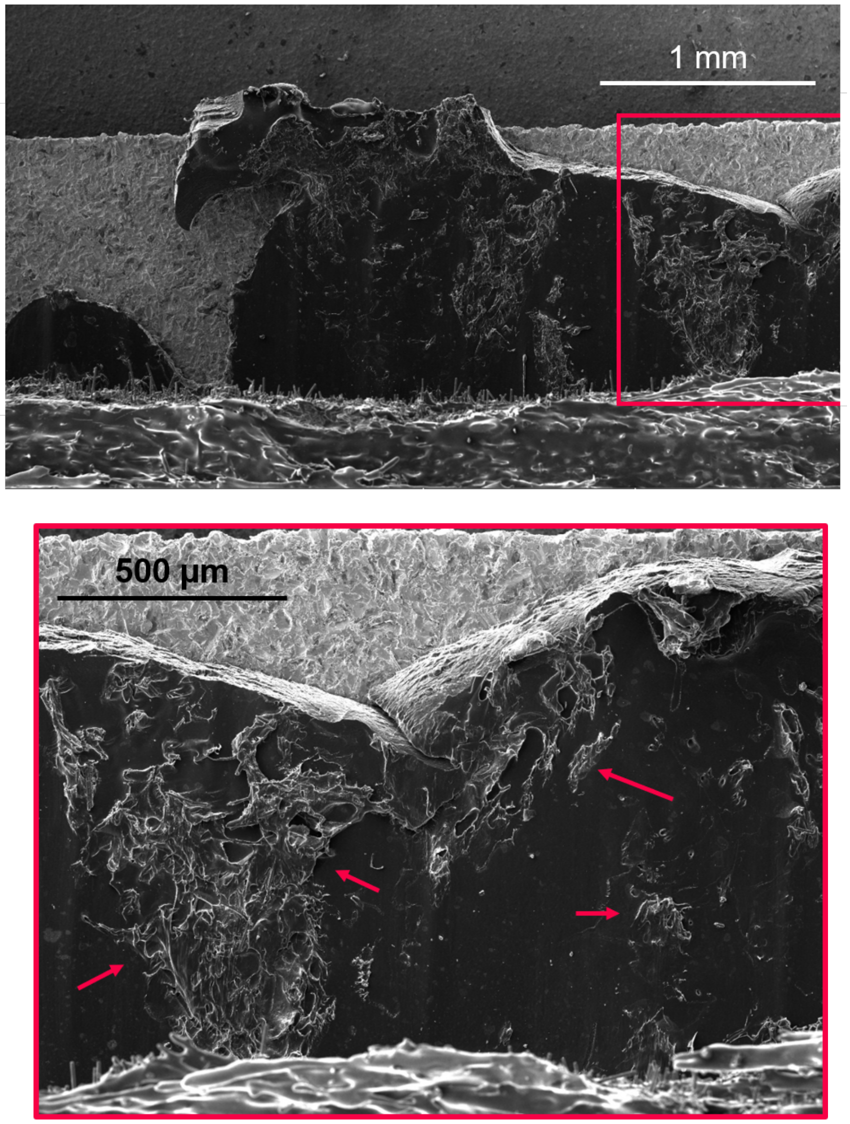

Figure 50: SEM micrograph showing a top view of a coating layer optimisation sample after failure including a closer view of the area marked with a red rectangle in the upper photo. PA-CF cusps are visible on the coating layer (red arrows).

5.3.2 Influence of the printing speed, *v* and the coating layer height, *h*

In an effort to link the printing speed and the coating layer height to the mechanical properties of the coating layer optimisation samples, the extrusion rate of the filament was calculated according to Equation 5.1.

$$Q = v * h * w \tag{5.1}$$

where

- Q [mm³/s] is the (volume) extrusion rate
- v [mm/s] is the printing speed
- h [mm] is the layer height
- w [mm] is the road width (= const. = 0.4 mm)

At small coating layer heights and/or slow printing speed, the extrusion rate becomes very slow. This might lead to errors in the extruder steps and therefore to an inconstant filament supply. At high extrusion rates on the other hand, this problem does not arise. Relevant tested conditions, the corresponding ULSS, fracture type and extrusion rate are displayed in Table 22. A clear tendency of a higher ULSS for higher extrusion rates can be identified: when increasing the printing speed from 5 mm/s to 50 mm/s, the ULSS of the samples increased by 185 %. Similarly, when the coating layer height was increased from 0.1 mm to 0.3 mm, the ULSS increased by another 84 %.

Table 22: Results of the relevant tested coating layer optimisation conditions concerning the relation printing speed and coating layer height to extrusion rate and fracture type. The bed temperature and the nozzle temperature are the same for all conditions displayed (T_{ext} = 150°C, T_{ext} = 280°C).

Condition	Printing speed	Coating layer height	ULSS	Dominant fracture type	Extrusion rate
	v [mm/s]	h [mm]	R_m [MPa]		r [mm^3/s]
C1	5	0.1	3.4 ± 1.4	Adhesive	0.2
C2	20	0.1	6.2 ± 1.3	Adhesive	0.8
C11	50	0.1	9.7 ± 2.5	Adhesive	2
C14	50	0.2	14.8 ± 2.1	Adhesive	4
C15	50	0.3	17.8 ± 0.7	Net-tension	6

In Figure 51, the fracture surface of a sample printed with a coating layer height of 0.1 mm is presented. The profile of the interface between the coating layer and the composite part appears generally uneven. This is probably a consequence of local under- and overextrusion which might have been due to the discussed low extrusion rate. As a result, in some areas the actual coating layer height is smaller than 0.1 mm (blue arrow). The local lack of material in those areas generally weakens the sample. In other areas (green arrows) the actual coating layer height is larger than 0.1 mm. In those areas, there is a local accumulation of material which can act as crack nucleation sites (see Figure 52) and hence, weaken the sample as well.

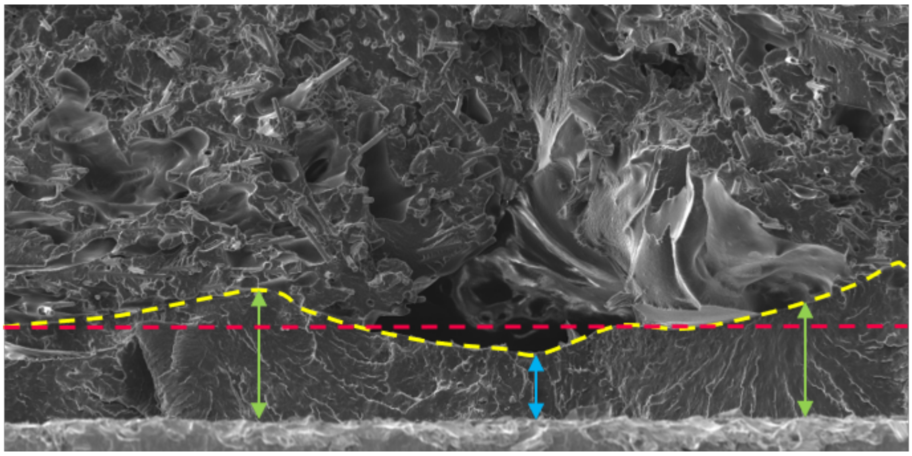

Figure 51: SEM micrograph of the fracture surface of a printed coating layer optimisation sample with a coating layer height of 0.1 mm; dashed red line represent a theoretical layer height of 0.1 mm; dashed yellow line shows the actual interface between coating layer and composite part; blue arrow indicates region of local underextrusion; green arrows indicate regions of local overextrusion.

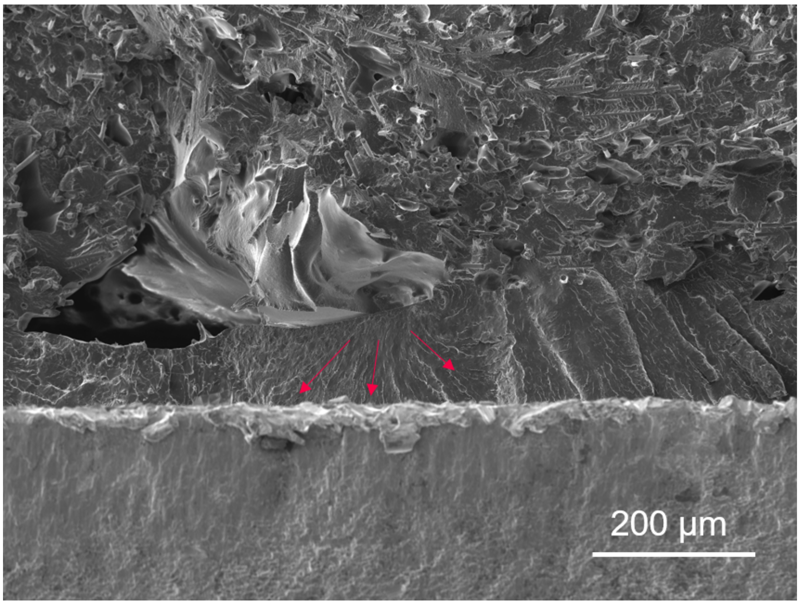

Figure 52: SEM micrograph of the fracture surface of a printed coating layer optimisation sample with a coating layer height of 0.1 mm; red arrows represent crack paths in a region of local overextrusion.

Further individual details of the coating layer height are addressed in the next section.

5.3.2.1 Coating layer height, *h*

A higher coating layer height leads to a higher ULSS. When increasing the coating layer height from 0.1 mm (C11) to 0.3 mm (C14), while all other parameters remain the same, the ultimate lap shear strength increases by 83.5 % from 9.7 ± 2.5 MPa to 17.8 ± 0.7 MPa (see Table 22). These results are contrarily to what is known about adhesive joints, where a thicker adhesive layer leads to failure at lower loads [52].

A possible explanation for this behaviour could be as follows. In the case of a set coating layer height of 0.3 mm, the inconstant (varying) coating layer height revealed itself as a wave-like profile that could be observed at the interface between the coating layer and the first layer of the composite part (see Figure 53). In the magnified view, fibres and pores of the composite part can be identified. While the fibres appear as white points or lines, the pores which were already discussed in Section 5.2.1 appear black.

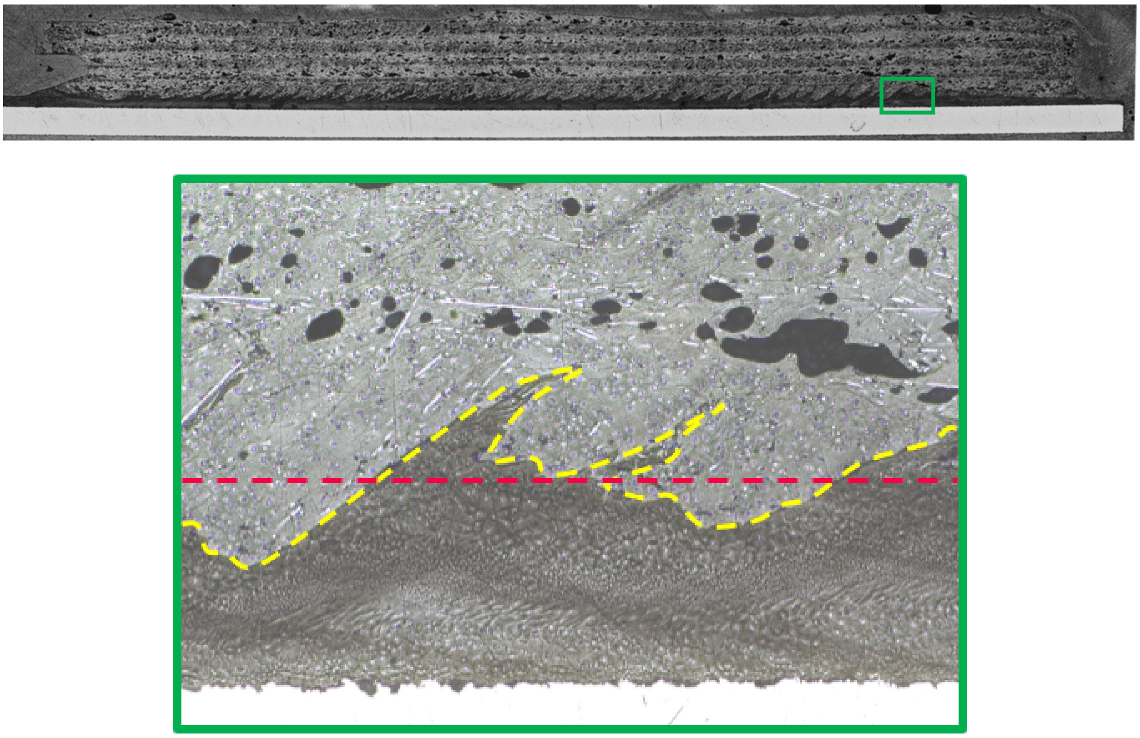

Figure 53: Cross-section of a printed coating layer optimisation sample with a coating layer height of 0.3 mm. The dashed red line represents a theoretical layer height of 0.3 mm; the dashed yellow line shows the actual interface between coating layer and composite part.

Due to the wave-like profile, it is suspected that the PA and the PA-CF polymers have been mixed during the FFF. This can be explained by the height settings during the discontinuous printing process: when the first PA-CF layer is printed, the printing bed uses the same z = 0 point as during the printing of the coating layer. Therefore, if the coating layer reaches a certain height (approx. 0.2 mm), the nozzle needs to move through the excess height when printing the first PA-CF layer. By doing so, the nozzle plows the excess material and mechanically mixes the coating layer with the first PA-CF layer. Therefore, setting the coating layer height to 0.3 mm does not lead to an actual coating layer height of 0.3 mm. This explanation also means that the observed results are less contradictory to what the literature suggests about the relationship between adhesive layer height and ULSS than previously suggested.

This material displacement and mix leads to a stronger interface. The wave-like structure also makes it harder for cracks to propagate along the interface. Thus, less delamination between the coating layer and the first PA-CF layer is observed as opposed to the samples with a coating layer height of 0.1 mm. This probably helps to promote the net-tension failure, which is predominantly observed for samples with a coating layer height of 0.3 mm.

Another reason for the higher ULSS at higher coating layer heights might be its higher resistance to secondary bending, which is a phenomenon that occurs in single-lap shear tests since the applied forces do not lie in the coating layer plane but eccentric to both sides of the coating layer [54]. As the material of the coating layer (PA) has the lowest stiffness of the three used materials, it was the most important one for accommodating the asymmetrical deformation, which resulted from the secondary bending effect. In this respect, plastic deformation of the coating layer took place. Proof could be found in the form of crazing in the fracture surfaces (see Figure 47). As a higher coating layer relates to more coating layer material that is able to undergo plastic deformation, more force

was needed until delamination occurred at the joint interface in the case of a large coating layer height. Therefore, more time was available for the formation of many crack nucleation points and net-tension failure was more likely to occur.
The different types of failure which were observed (A-M, A-P, NT) are promoted by different components of breaking which all happen at the same time but not to the same extent depending on the coating layer height. Figure 54 graphically represents the different mechanisms that take place. A net-tension failure is promoted by many crack nucleation points spread over the whole sample (green stars), as already mentioned in the previous paragraph. This was observed in all samples with a coating layer height of 0.3 mm and in some with a coating layer height of 0.2 mm. Both adhesive fracture types (A-M and A-P) can originate from crack nucleation points at the interface of the coating layer and the first layer printed with PA-CF (blue stars). One of those crack nucleation points at the interface can also be identified in the SEM micrograph in Figure 54(a). From there the cracks propagate radially through the coating layer (blue and orange arrows). However, there are no marks of the crack propagating through the composite part visible. This is due to the presence of fibres in the reinforced PA-CF, which act as scattering points for the crack. Therefore, in the reinforced polymer, the cracks still propagate but in a scattered manner. This makes following the crack path into the composite part much more difficult. Analogously A-M and A-P can also or additionally originate from the interface of the metallic substrate and the coating layer (purple stars and arrows).

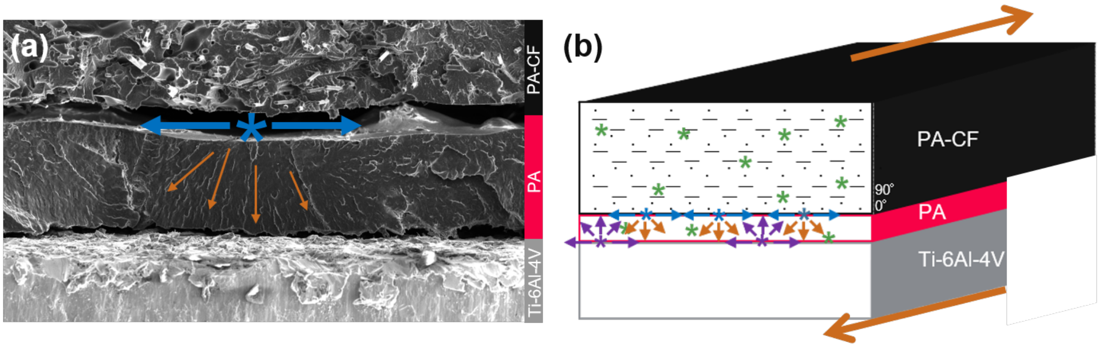

Figure 54: (a) SEM micrograph of the fracture surface of a sample with a coating layer height of 0.1 mm and a mixed failure type (A-M, A-P); (b) Schematic representation of the different components of breaking which influence the type of failure; the large orange arrows represent the direction of the lap-shear test force; stars represent crack nucleation points, small arrows represent crack propagation.

In Figure 55, scarps are visible in the coating layer, which indicate that from both sides, cracks propagated radially through the coating layer starting at the PA/PA-CF interface and met in the middle building a crack front. This indicates that several crack nucleation sites were present and active in a given sample.

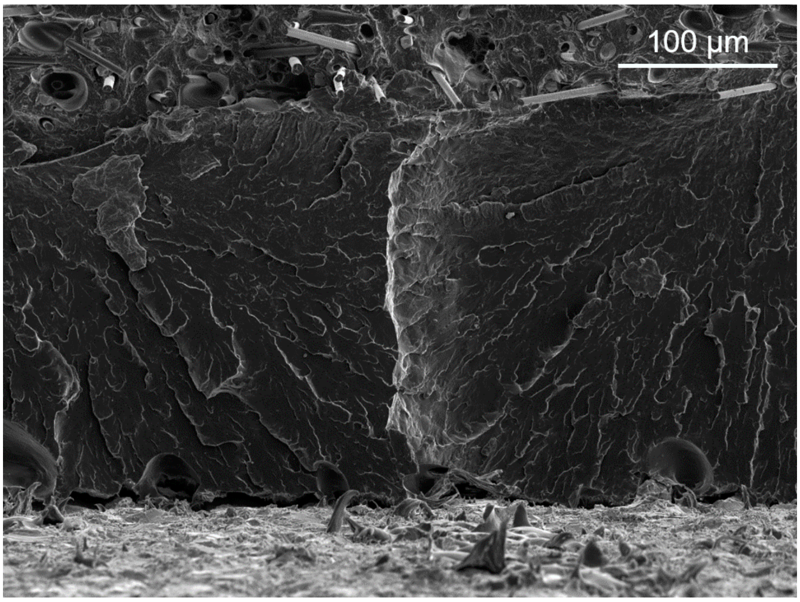

Figure 55: SEM micrograph of white scarps indicating crack propagation in the coating layer and coming from both sides producing a crack front in the middle.

If the interface bonding is weak, the horizontal component of the crack propagation along the interface is faster and more efficient (blue arrows in Figure 54). This leads to a delamination at that interface and therefore also promotes an adhesive failure at that PA/PA-CF interface (A-P). This situation was observed for many samples with a coating layer height of 0.1 mm and for some samples with a coating layer height of 0.2 mm.

An adhesive failure between the metallic substrate and the coating layer (A-M) was only observed for samples with a coating layer height of 0.1 mm. In those samples, the vertical crack propagation can be identified by the presence of scarps (white marks of crack propagation) which are marked in Figure 54 with orange arrows [36]. As opposed to the horizontal crack propagation (blue arrows), this vertical propagation has a more local impact on the detachment of the coating layer from the substrate. Therefore, more crack nucleation points might be needed than in the case of the adhesive failure between the coating layer and the composite part (A-P). Cracks nucleating from inside the coating layer and spreading radially from the nucleation point probably promote adhesive failure at both interfaces to a similar extent.

In analogy to what was said before about the crack nucleation at the PA/PA-CF interface, the horizontal crack propagation component of cracks nucleating at the Ti/PA interface probably promotes an adhesive failure at that interface and their vertical crack propagation component probably promotes an adhesive failure at the PA/PA-CF interface.

6 Conclusions

In this study, the FFF of PA-CF could be fully optimised, while the initial steps towards the process optimisation for the AddJoining of Ti-6Al-4V/PA/PA-CF were established.

Regarding the FFF optimisation, ultimate tensile strength (UTS) values of 117 MPa could consistently be achieved, which was 13.5 % higher than the value presented in the manufacturer datasheet. Among the tested process parameters, the layer height had the highest influence on the mean value of the UTS. Process temperatures also played a statistically-significant role on the mechanical performance of the printed part. Regarding the printing bed material, the UTS of the samples printed on glass was 41 % higher than of those printed on aluminium, where a worse interlayer bonding was found.

As for the AddJoining, an ultimate lap shear strength (ULSS) of 17.8 MPa could consistently be achieved using an OFAT approach. In the study, it was established that the coating layer height as well as its printing speed had a statistically-significant influence on the ULSS, according to the ANOVA analysis. It was concluded that both, higher layer heights and printing speeds led to a better mechanical performance of the hybrid joints under the specific load type promoted by the lap shear test. Higher layers appeared to accommodate more effectively the secondary bending during the test, while higher printing speeds resulted in higher extrusion rates, which suppressed occasional crack-nucleating inhomogeneities caused by step errors in the extrusion gears.

7 Outlook

Especially the interface between the metallic substrate and the coating layer plays an important role and can still be improved in order to achieve a stronger joint area. Further studies concerning this interface should consider different surface preparation methods of the metallic substrate and investigate new material combinations.

Based on the CLO results, a DoE of addjoined specimens would deepen the knowledge about the influence of the different process parameters. In this study, the highest printing speed, coating layer height and printing bed temperature lead to the best results. Therefore, it would be interesting to evaluate the effect of using even higher values for these parameters.

Besides the direct printing parameters, the surrounding environment may affect the process significantly. If the ambient temperature would be kept constant at an elevated level, the polymer would cool and solidify slower which might positively influence the mechanical performance. Additionally, a controlled air circulation within the printing chamber could ensure a homogeneous distribution of the temperature and therefore help to avoid inhomogeneous cooling rates.

Another important aspect which may still be optimised is the continuity of the process. In this study, the printing of the coating layer and the printing of the composite part were two separate processes. If the composite part could be printed directly after finishing the coating layer, chances are that a stronger interface between both can be obtained.

Furthermore, different post-treatment methods should be considered to improve the AddJoining process. An adequate heat treatment for example may promote better adhesion due to the reliquidification of the polymer which can help increase the bonding between the layers. Due to the strong material-dependence of corrosion and oxidation properties of metals and e.g. water absorption properties of polymers, also natural ageing should be considered.

Lastly, there is a wide range of possible mechanical tests and the potential of AddJoining should also be optimised using different tests, e.g. bending testing, in order to understand the adhesion mechanisms even better and close the existing knowledge gap.

References

[1] Climate Change, 2016. URL `https://www.un.org/en/sections/issues-depth/climate-change/`.

[2] Efthimios Zervas and Christos Lazarou. Influence of European passenger cars weight to exhaust CO_2 emissions. *Energy Policy*, 36(1):248–257, 2008. ISSN 03014215. doi: 10.1016/j.enpol.2007.09.009.

[3] R. Falck, S. M. Goushegir, J. F. dos Santos, and S. T. Amancio-Filho. AddJoining: A novel additive manufacturing approach for layered metal-polymer hybrid structures. *Materials Letters*, 217:211–214, 2018. ISSN 0167577X. doi: 10.1016/j.matlet.2018.01.021.

[4] Rielson Falck, Jorge F. Dos Santos, and Sergio T. Amancio-Filho. Microstructure and Mechanical Performance of Additively Manufactured Aluminum 2024-T3/Acrylonitrile Butadiene Styrene Hybrid Joints Using an AddJoining Technique. *Materials (Basel, Switzerland)*, 12(6), 2019. ISSN 1996-1944. doi: 10.3390/ma12060864.

[5] Arthur Lepoivre, Nicolas Boyard, Arthur Levy, and Vincent Sobotka. Heat Transfer and Adhesion Study for the FFF Additive Manufacturing Process. *Procedia Manufacturing*, 47: 948–955, 2020. doi: 10.1016/j.promfg.2020.04.291.

[6] Charoula Kousiatza and Dimitris Karalekas. In-situ monitoring of strain and temperature distributions during fused deposition modeling process. *Materials & Design*, 97:400–406, 2016. ISSN 02641275. doi: 10.1016/j.matdes.2016.02.099.

[7] Sang Yoon Park, Won Jong Choi, Heung Soap Choi, Hyuk Kwon, and Sang Hwan Kim. Recent Trends in Surface Treatment Technologies for Airframe Adhesive Bonding Processing: A Review (1995–2008). *The Journal of Adhesion*, 86(2):192–221, 2010. ISSN 0021-8464. doi: 10.1080/00218460903418345.

[8] Gerd Habenicht. *Kleben: Grundlagen, Technologien, Anwendungen : mit 37 Tabellen*. Springer, Berlin, 5., erw. und aktualisierte aufl. edition, 2006. ISBN 9781280619908.

[9] M. C. van der Leeden and G. Frens. Surface Properties of Plastic Materials in Relation to Their Adhering Performance. *Advanced Engineering Materials*, 4(5): 280–289, 2002. ISSN 14381656. doi: 10.1002/1527-2648(20020503)4:5{\textless}280::AID-ADEM280{\textgreater}3.0.CO;2-Z.

[10] Fang Deng, Xu-Biao Luo, Lin Ding, and Sheng-Lian Luo. Application of Nanomaterials and Nanotechnology in the Reutilization of Metal Ion From Wastewater. In *Nanomaterials for the Removal of Pollutants and Resource Reutilization*, volume 110, pages 149–178. Elsevier, 2019. ISBN 9780128148372. doi: 10.1016/B978-0-12-814837-2.00005-6.

[11] Matt Joseph. *Media Blasting & Metal Preparation: A Complete Guide*. CarTech Inc, North Branch, 2016. ISBN 9781613253519.

[12] Q. Sun, G. M. Rizvi, C. T. Bellehumeur, and P. Gu. Effect of processing conditions on the bonding quality of FDM polymer filaments. *Rapid Prototyping Journal*, 14(2):72–80, 2008. ISSN 1355-2546. doi: 10.1108/13552540810862028.

[13] S. F. Costa, F. M. Duarte, and J. A. Covas. Thermal conditions affecting heat transfer in FDM/FFE: a contribution towards the numerical modelling of the process. *Virtual and Physical Prototyping*, 10(1):35–46, 2015. ISSN 1745-2759. doi: 10.1080/17452759.2014.984042.

[14] António Pais. Numerical and Experimental Analysis of the Heat Exchanges in the FDM Technology. Instituto Superior Técnico, Universidade de Lisboa, Portugal, 2018.

[15] Martin Spoerk, Joamin Gonzalez-Gutierrez, Janak Sapkota, Stephan Schuschnigg, and Clemens Holzer. Effect of the printing bed temperature on the adhesion of parts produced by fused filament fabrication. *Plastics, Rubber and Composites*, 47(1):17–24, 2018. ISSN 1465-8011. doi: 10.1080/14658011.2017.1399531.

[16] Yogesh Nandwani. *Characterization of Structural Adhesives Using Lap Shear and Pin and Collar Tests*. PhD thesis, University of Waterloo, Waterloo, Ontario, Canada, 2015. URL `https://uwspace.uwaterloo.ca/bitstream/handle/10012/9799/Nandwani_Yogesh.pdf;sequence=3`.

[17] Ultimaker. Technisches Datenblatt Nylon, 2017. URL `https://asset.conrad.com/media10/add/160267/c1/-/de/001528695DS01/datenblatt-1528695-ultimaker-filament-pa-polyamid-285-mm-transparent-750-g.pdf`.

[18] Hans Domininghaus, Peter Elsner, Peter Eyerer, and Thomas Hirth. *Kunststoffe: Eigenschaften und Anwendungen*. VDI-Buch. Springer, Berlin and Heidelberg, 8., neu bearb. und erw. aufl. edition, 2012. ISBN 9783642161728. doi: 10.1007/978-3-642-16173-5.

[19] Ultimaker filament pa (polyamid) 2.85 mm transparent 750 g kaufen, 17.01.2021. URL `https://www.conrad.de/de/p/ultimaker-filament-pa-polyamid-2-85-mm-transparent-750-g-1528695.html#productHighlights`.

[20] Hyun-Seok Cho, Mayukhee Das, Heli Wang, Huyen N. Dinh, and J. W. van Zee. The Contamination Mechanism and Behavior of Amide Bond Containing Organic Contaminant on PEMFC. *Journal of The Electrochemical Society*, 162(4):F427–F435, 2015. ISSN 0013-4651. doi: 10.1149/2.0631504jes.

[21] BASF. BASF Ultrafuse PAHT CF 15, 03.10.2020. URL `https://ultimaker.com/de/materials/basf-ultrafuse-paht-cf-15`.

[22] Nekoda van de Werken, Halil Tekinalp, Pouria Khanbolouki, Soydan Ozcan, Andrew Williams, and Mehran Tehrani. Additively manufactured carbon fiber-reinforced composites: State of the art and perspective. *Additive Manufacturing*, 31:100962, 2020. ISSN 22148604. doi: 10.1016/j.addma.2019.100962.

[23] Peng Wang, Bin Zou, Shouling Ding, Chuanzhen Huang, Zhenyu Shi, Yongsheng Ma, and Peng Yao. Preparation of short CF/GF reinforced PEEK composite filaments and their comprehensive properties evaluation for FDM-3D printing. *Composites Part B: Engineering*, 198:108175, 2020. ISSN 13598368. doi: 10.1016/j.compositesb.2020.108175.

[24] Zhenzhen Quan, Zachary Larimore, Amanda Wu, Jianyong Yu, Xiaohong Qin, Mark Mirotznik, Jonghwan Suhr, Joon-Hyung Byun, Youngseok Oh, and Tsu-Wei Chou. Microstructural design and additive manufacturing and characterization of 3D orthogonal

short carbon fiber/acrylonitrile-butadiene-styrene preform and composite. *Composites Science and Technology*, 126:139–148, 2016. ISSN 02663538. doi: 10.1016/j.compscitech.2016.02.021.

[25] Rafael Thiago Luiz Ferreira, Igor Cardoso Amatte, Thiago Assis Dutra, and Daniel Bürger. Experimental characterization and micrography of 3D printed PLA and PLA reinforced with short carbon fibers. *Composites Part B: Engineering*, 124:88–100, 2017. ISSN 13598368. doi: 10.1016/j.compositesb.2017.05.013.

[26] Elena Verdejo de Toro, Juana Coello Sobrino, Alberto Matínez Martínez, and Valentín Miguel Eguía. Analysis of the influence of the variables of the Fused Deposition Modeling (FDM) process on the mechanical properties of a carbon fiber-reinforced polyamide. *Procedia Manufacturing*, 2019.

[27] Ian J. Polmear. *Light alloys: From traditional alloys to nanocrystals*. Elsevier Butterworth-Heinemann, Amsterdam, 4. ed., repr edition, 2007. ISBN 9780750663717.

[28] Christoph Leyens and Manfred Peters. *Titanium and Titanium Alloys*. Wiley, 2003. ISBN 9783527305346. doi: 10.1002/3527602119.

[29] Smiths Metal Centres. Ti-6Al-4V (Grade 5) Technical Datasheet, 2018. URL `https://www.smithmetal.com/pdf/titanium/ti-6al-4v-grade-5.pdf`.

[30] Birhan Sefer, Joan Josep Roa, Antonio Mateo, Robert Pederson, and Marta-Lena Antti. Evaluation of the Bulk and Alpha-Case Layer Properties in Ti-6Al-4V at Micro-And Nano-Metric Length Scale. In Vasisht Venkatesh, Adam L. Pilchak, John E. Allison, Sreeramamurthy Ankem, Rodney Boyer, Julie Christodoulou, Hamish L. Fraser, M. Ashraf Imam, Yoji Kosaka, Henry J. Rack, Amit Chatterjee, and Andy Woodfield, editors, *Proceedings of the 13th World Conference on Titanium*, volume 213, pages 1619–1624. John Wiley & Sons, Inc, Hoboken, NJ, USA, 2016. ISBN 9781119296126. doi: 10.1002/9781119296126.ch271.

[31] 3D Universe. Ultimaker Print Core Red CC (0.6mm), 17.01.2021. URL `https://shop3duniverse.com/products/ultimaker-print-core-cc-0-6mm`.

[32] ISO. BS EN ISO 527-2:2012: Plastics –Determination of Tensile Properties, Part 2: Test Conditions for Moulding and Extrusion Plastics, 2012. URL `https://www.iso.org/standard/56046.html`.

[33] Goerg H. Michler. *Kompakte Einführung in die Elektronenmikroskopie*. Springer Fachmedien Wiesbaden, Wiesbaden, 2019. ISBN 978-3-658-26687-5. doi: 10.1007/978-3-658-26688-2.

[34] M. Atapour, A. Pilchak, G. S. Frankel, J. C. Williams, M. H. Fathi, and M. Shamanian. Corrosion Behavior of Ti-6Al-4V with Different Thermomechanical Treatments and Microstructures. *CORROSION*, 66(6):065004–065004–9, 2010. ISSN 0010-9312. doi: 10.5006/1.3452400.

[35] Robert Pederson. *Microstructure and Phase Transformation of Ti-6Al-4V*. Licentiate thesis, Lulea University of Technology, Lulea, May 2002. URL `https://www.diva-portal.org/smash/get/diva2:991369/FULLTEXT01.pdf`.

[36] E. S. Greenhalgh. *Failure analysis and fractography of polymer composites*. Woodhead Publishing in materials. Woodhead Pub, Cambridge, 2009. ISBN 978-1-84569-217-9.

[37] Fracture of Glassy Polymers - Cavitation and Crazing. URL `http://polymerdatabase.com/polymer%20physics/Crazing.html`.

[38] Yunyun Ma, Chun Yan, Haibing Xu, Dong Liu, Pengcheng Shi, Yingdan Zhu, and Junlong Liu. Enhanced interfacial properties of carbon fiber reinforced polyamide 6 composites by grafting graphene oxide onto fiber surface. *Applied Surface Science*, 452:286–298, 2018. ISSN 0169-4332. doi: 10.1016/j.apsusc.2018.04.274.

[39] S. Tiwari and J. Bijwe. Surface Treatment of Carbon Fibers - A Review. *Procedia Technology*, 14:505–512, 2014. ISSN 22120173. doi: 10.1016/j.protcy.2014.08.064.

[40] Tao Zhang, Yueqing Zhao, Hongfu Li, and Boming Zhang. Effect of polyurethane sizing on carbon fibers surface and interfacial adhesion of fiber/polyamide 6 composites. *Journal of Applied Polymer Science*, 135(16):46111, 2018. ISSN 00218995. doi: 10.1002/app.46111.

[41] Tao Zhang, Yue Xu, Hongfu Li, and Boming Zhang. Interfacial adhesion between carbon fibers and nylon 6: Effect of fiber surface chemistry and grafting of nano-SiO_2. *Composites Part A: Applied Science and Manufacturing*, 121:157–168, 2019. ISSN 1359835X. doi: 10.1016/j.compositesa.2019.03.029.

[42] Lin Sang, YuKai Wang, Guangyi Chen, Jicai Liang, and Zhiyong Wei. A comparative study of the crystalline structure and mechanical properties of carbon fiber/polyamide 6 composites enhanced with/without silane treatment. *RSC Advances*, 6(109):107739–107747, 2016. doi: 10.1039/C6RA18394H.

[43] Yu Zhao, Yuansong Chen, and Yongjun Zhou. Novel mechanical models of tensile strength and elastic property of FDM AM PLA materials: Experimental and theoretical analyses. *Materials & Design*, 181:108089, 2019. ISSN 02641275. doi: 10.1016/j.matdes.2019.108089.

[44] S. Garzon-Hernandez, D. Garcia-Gonzalez, A. Jérusalem, and A. Arias. Design of FDM 3D printed polymers: An experimental-modelling methodology for the prediction of mechanical properties. *Materials & Design*, 188:108414, 2020. ISSN 02641275. doi: 10.1016/j.matdes.2019.108414.

[45] Peng Wang, Bin Zou, Shouling Ding, Lei LI, and Chuanzhen Huang. Effects of FDM-3D printing parameters on mechanical properties and microstructure of CF/PEEK and GF/PEEK. *Chinese Journal of Aeronautics*, 2020. ISSN 10009361. doi: 10.1016/j.cja.2020.05.040.

[46] Junior Nomani, Daniel Wilson, Mariana Paulino, and Mazher Iqbal Mohammed. Effect of layer thickness and cross-section geometry on the tensile and compression properties of 3D printed ABS. *Materials Today Communications*, 22:100626, 2020. ISSN 2352-4928. doi: 10.1016/j.mtcomm.2019.100626.

[47] Vladimir E Kuznetsov, Alexey N Solonin, Oleg D. Urzhumtsev, Richard Schielling, and Azamat G Tavitov. Strength of PLA Components Fabricated with Fused Deposition Technology using a Desktop 3D Printer as a Function of Geometrical Parameters of the Process. *Journal of Material Science & Engineering*, 07(01), 2018. doi: 10.4172/2169-0022.1000429.

[48] Kejian Wang. Die Swell of Complex Polymeric Systems. In Juan de Vicente, editor, *Viscoelasticity - From Theory to Biological Applications*. InTech, 2012. ISBN 978-953-51-0841-2. doi: 10.5772/50137.

[49] Shouling Ding, Bin Zou, Peng Wang, and Hongjian Ding. Effects of nozzle temperature and building orientation on mechanical properties and microstructure of PEEK and PEI printed by 3D-FDM. *Polymer Testing*, 78:105948, 2019. ISSN 01429418. doi: 10.1016/j.polymertesting.2019.105948.

[50] Aliaksandr Skaskevich, Ammar Sudan, and Dzhendo Dzhendov. Influence of technological parameters of FDM-print on the strength characteristics of samples of polyamide. *International scientific journal "Machines. Technologies. Materials"*, Vol. 14 Issue 5:210–212, 2020. URL `https://stumejournals.com/journals/mtm/2020/5/210.full.pdf`.

[51] Erhard Hornbogen, Gunther Eggeler, and Ewald Werner. *Werkstoffe: Aufbau und Eigenschaften von Keramik-, Metall-, Polymer- und Verbundwerkstoffen*. Springer, 12., aktualisierte auflage edition, 2019. ISBN 9783662588475.

[52] Philipp Weißgraeber, Julian Felger, Andreas Talmon l'Armée, and Wilfried Becker. Crack initiation in single lap joints: effects of geometrical and material properties. *International Journal of Fracture*, 192(2):155–166, 2015. ISSN 0376-9429. doi: 10.1007/s10704-015-9992-6.

[53] Dr. C. C. Hsiao. Crazing in polymeric and composite systems, 1990. URL `https://apps.dtic.mil/dtic/tr/fulltext/u2/a235525.pdf`.

[54] Rielson Miler Moreira Falck. *A new additive manufacturing technique for layered metal-composite hybrid structures: A new additive manufacturing technique for layered metal-composite hybrid structures*. PhD thesis, Technische Universität Hamburg, 2020. URL `https://tore.tuhh.de/handle/11420/7476.4`.

List of Tables

List of Figures

Annexes

I Datasheet of the reinforced polymer (PA-CF)

Table 23: Datasheet of the reinforced polymer (PA-CF). Reproduced from [21].

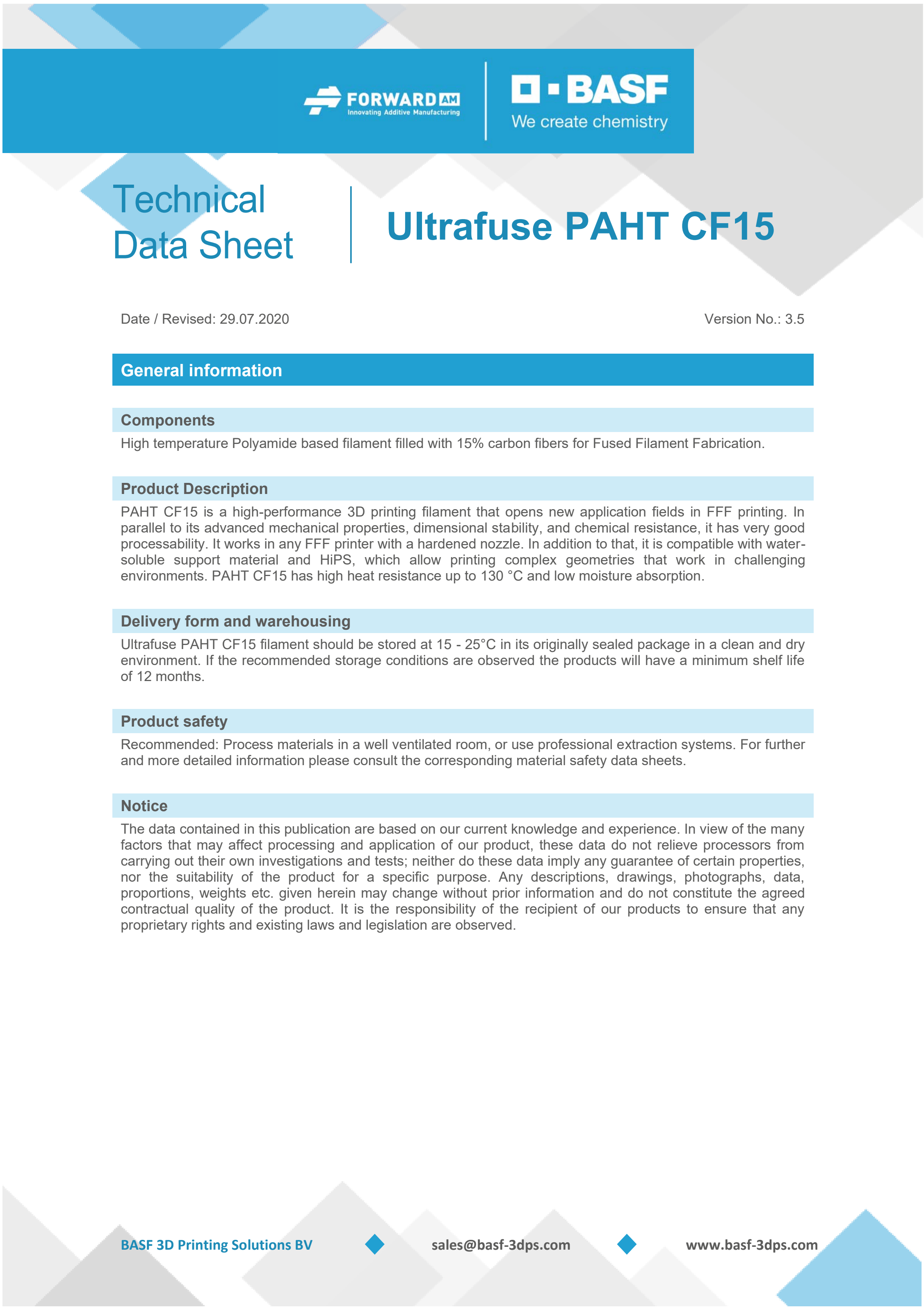

FORWARD AM
Innovating Additive Manufacturing

BASF
We create chemistry

Technical Data Sheet

Ultrafuse PAHT CF15

Date / Revised: 29.07.2020 Version No.: 3.5

General information

Components

High temperature Polyamide based filament filled with 15% carbon fibers for Fused Filament Fabrication.

Product Description

PAHT CF15 is a high-performance 3D printing filament that opens new application fields in FFF printing. In parallel to its advanced mechanical properties, dimensional stability, and chemical resistance, it has very good processability. It works in any FFF printer with a hardened nozzle. In addition to that, it is compatible with water-soluble support material and HiPS, which allow printing complex geometries that work in challenging environments. PAHT CF15 has high heat resistance up to 130 °C and low moisture absorption.

Delivery form and warehousing

Ultrafuse PAHT CF15 filament should be stored at 15 - 25°C in its originally sealed package in a clean and dry environment. If the recommended storage conditions are observed the products will have a minimum shelf life of 12 months.

Product safety

Recommended: Process materials in a well ventilated room, or use professional extraction systems. For further and more detailed information please consult the corresponding material safety data sheets.

Notice

The data contained in this publication are based on our current knowledge and experience. In view of the many factors that may affect processing and application of our product, these data do not relieve processors from carrying out their own investigations and tests; neither do these data imply any guarantee of certain properties, nor the suitability of the product for a specific purpose. Any descriptions, drawings, photographs, data, proportions, weights etc. given herein may change without prior information and do not constitute the agreed contractual quality of the product. It is the responsibility of the recipient of our products to ensure that any proprietary rights and existing laws and legislation are observed.

BASF 3D Printing Solutions BV ◆ sales@basf-3dps.com ◆ www.basf-3dps.com

Table 24: Datasheet of the reinforced polymer (PA-CF). Reproduced from [21].

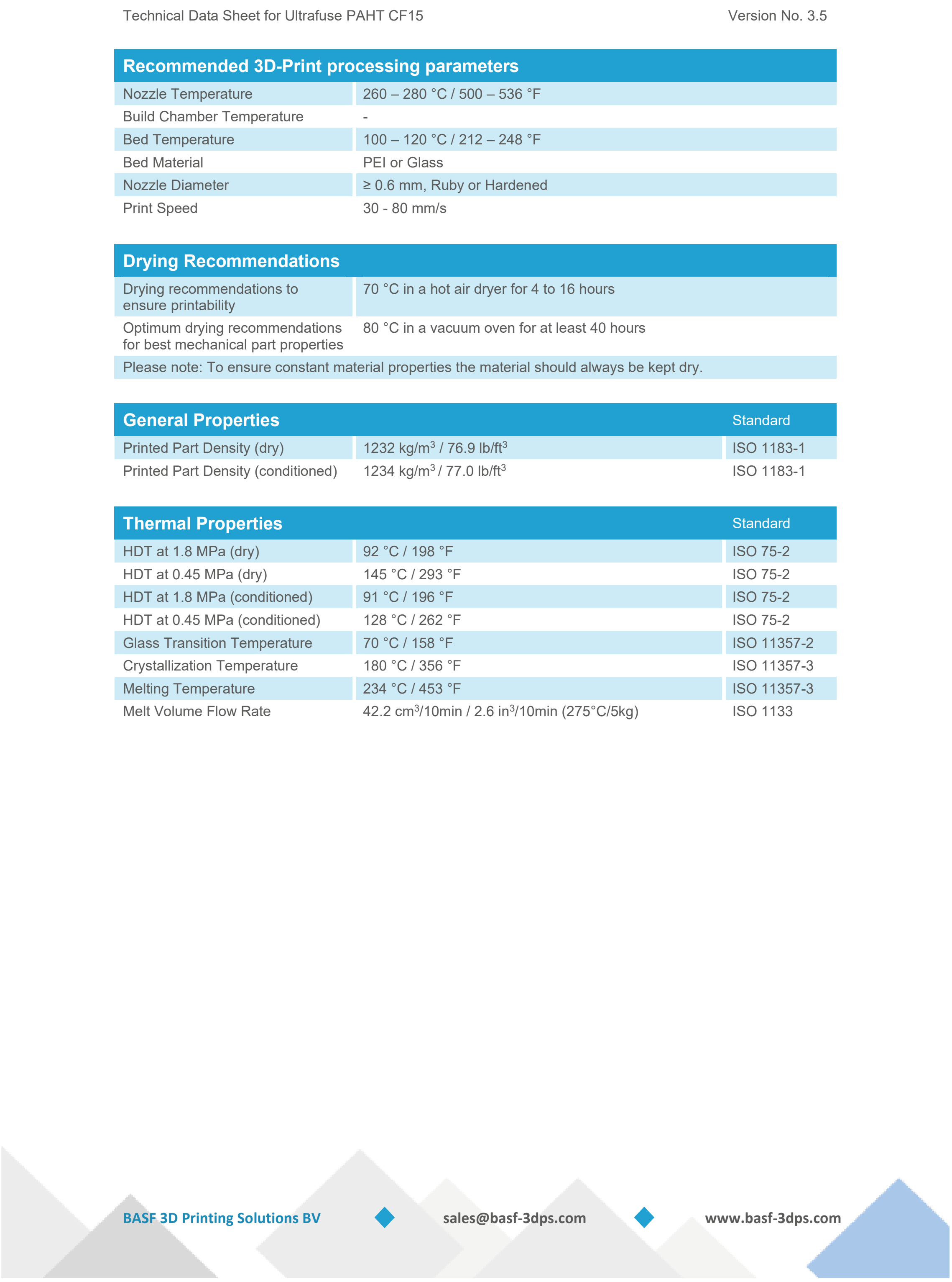

Technical Data Sheet for Ultrafuse PAHT CF15 Version No. 3.5

Recommended 3D-Print processing parameters	
Nozzle Temperature	260 – 280 °C / 500 – 536 °F
Build Chamber Temperature	-
Bed Temperature	100 – 120 °C / 212 – 248 °F
Bed Material	PEI or Glass
Nozzle Diameter	≥ 0.6 mm, Ruby or Hardened
Print Speed	30 - 80 mm/s

Drying Recommendations	
Drying recommendations to ensure printability	70 °C in a hot air dryer for 4 to 16 hours
Optimum drying recommendations for best mechanical part properties	80 °C in a vacuum oven for at least 40 hours
Please note: To ensure constant material properties the material should always be kept dry.	

General Properties		Standard
Printed Part Density (dry)	1232 kg/m^3 / 76.9 lb/ft^3	ISO 1183-1
Printed Part Density (conditioned)	1234 kg/m^3 / 77.0 lb/ft^3	ISO 1183-1

Thermal Properties		Standard
HDT at 1.8 MPa (dry)	92 °C / 198 °F	ISO 75-2
HDT at 0.45 MPa (dry)	145 °C / 293 °F	ISO 75-2
HDT at 1.8 MPa (conditioned)	91 °C / 196 °F	ISO 75-2
HDT at 0.45 MPa (conditioned)	128 °C / 262 °F	ISO 75-2
Glass Transition Temperature	70 °C / 158 °F	ISO 11357-2
Crystallization Temperature	180 °C / 356 °F	ISO 11357-3
Melting Temperature	234 °C / 453 °F	ISO 11357-3
Melt Volume Flow Rate	42.2 cm^3/10min / 2.6 in^3/10min (275°C/5kg)	ISO 1133

BASF 3D Printing Solutions BV ◆ sales@basf-3dps.com ◆ www.basf-3dps.com

Table 25: Datasheet of the reinforced polymer (PA-CF). Reproduced from [21].

Technical Data Sheet for Ultrafuse PAHT CF15 Version No. 3.5

Mechanical Properties | Dried Specimen

Print direction	Standard	XY	XZ	ZX
		Flat	On its edge	Upright
Tensile strength	ISO 527	103.2 MPa / 15.0 ksi	-	18.2 MPa / 2.6 ksi
Elongation at Break	ISO 527	1.8 %	-	0.5 %
Young's Modulus	ISO 527	8386 MPa / 1216 ksi	-	3532 MPa / 512 ksi
Flexural Strength	ISO 178	160.7 MPa / 23.3 ksi	171.8 MPa / 24.9 ksi	50.8 MPa / 7.4 ksi
Flexural Modulus	ISO 178	8258 MPa / 1198 ksi	7669 MPa / 1112 ksi	2715 MPa / 394 ksi
Flexural Strain at Break	ISO 178	2.4 %	2.8 %	1.8 %
Impact Strength Charpy (notched)	ISO 179-2	4.8 kJ/m²	3.9 kJ/m²	1.3 kJ/m²
Impact Strength Charpy (unnotched)	ISO 179-2	20.6 kJ/m²	19.3 kJ/m²	2.9 kJ/m²
Impact Strength Izod (notched)	ISO 180	4.9 kJ/m²	5.1 kJ/m²	-
Impact Strength Izod (unnotched)	ISO 180	16.4 kJ/m²	18.1 kJ/m²	2.9 kJ/m²

Electrical Properties

Volume resistivity	IEC 62631-3-1	3.2E+07 Ωcm	-	1.6E+05 Ωcm
Surface resistivity	IEC 62631-3-2	9.7E+05 Ω	-	1.8E+06 Ω

BASF 3D Printing Solutions BV ◆ **sales@basf-3dps.com** ◆ **www.basf-3dps.com**

II Datasheet of the unreinforced polymer (PA)

Table 26: Datasheet of the unreinforced polymer (PA). Reproduced from [17].

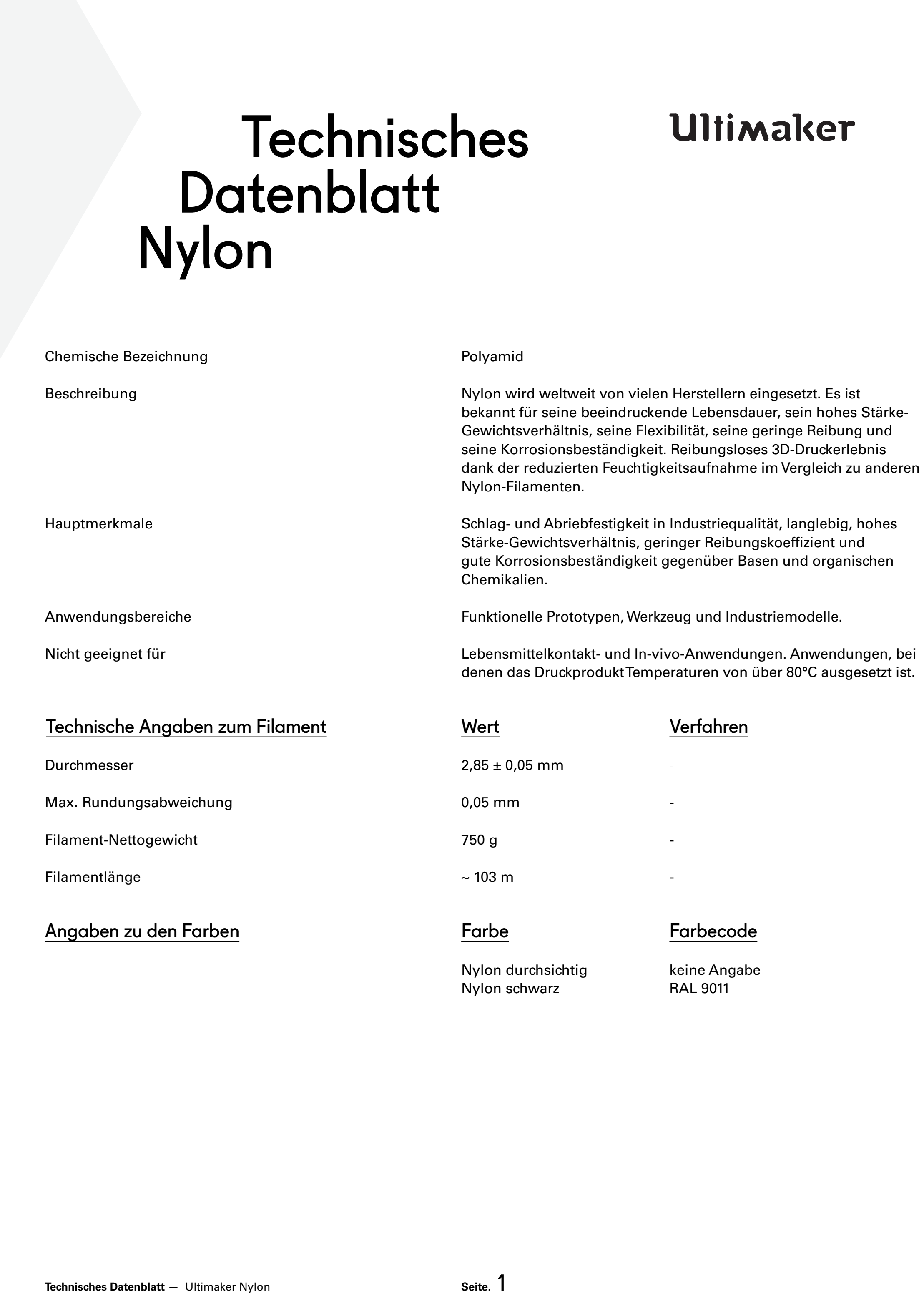

Ultimaker

Technisches
Datenblatt
Nylon

Chemische Bezeichnung	Polyamid
Beschreibung	Nylon wird weltweit von vielen Herstellern eingesetzt. Es ist bekannt für seine beeindruckende Lebensdauer, sein hohes Stärke-Gewichtsverhältnis, seine Flexibilität, seine geringe Reibung und seine Korrosionsbeständigkeit. Reibungsloses 3D-Druckerlebnis dank der reduzierten Feuchtigkeitsaufnahme im Vergleich zu anderen Nylon-Filamenten.
Hauptmerkmale	Schlag- und Abriebfestigkeit in Industriequalität, langlebig, hohes Stärke-Gewichtsverhältnis, geringer Reibungskoeffizient und gute Korrosionsbeständigkeit gegenüber Basen und organischen Chemikalien.
Anwendungsbereiche	Funktionelle Prototypen, Werkzeug und Industriemodelle.
Nicht geeignet für	Lebensmittelkontakt- und In-vivo-Anwendungen. Anwendungen, bei denen das Druckprodukt Temperaturen von über 80°C ausgesetzt ist.

Technische Angaben zum Filament	Wert	Verfahren
Durchmesser	2,85 ± 0,05 mm	-
Max. Rundungsabweichung	0,05 mm	-
Filament-Nettogewicht	750 g	-
Filamentlänge	~ 103 m	-

Angaben zu den Farben	Farbe	Farbecode
	Nylon durchsichtig	keine Angabe
	Nylon schwarz	RAL 9011

Technisches Datenblatt — Ultimaker Nylon **Seite.** 1

Table 27: Datasheet of the unreinforced polymer (PA). Reproduced from [17].

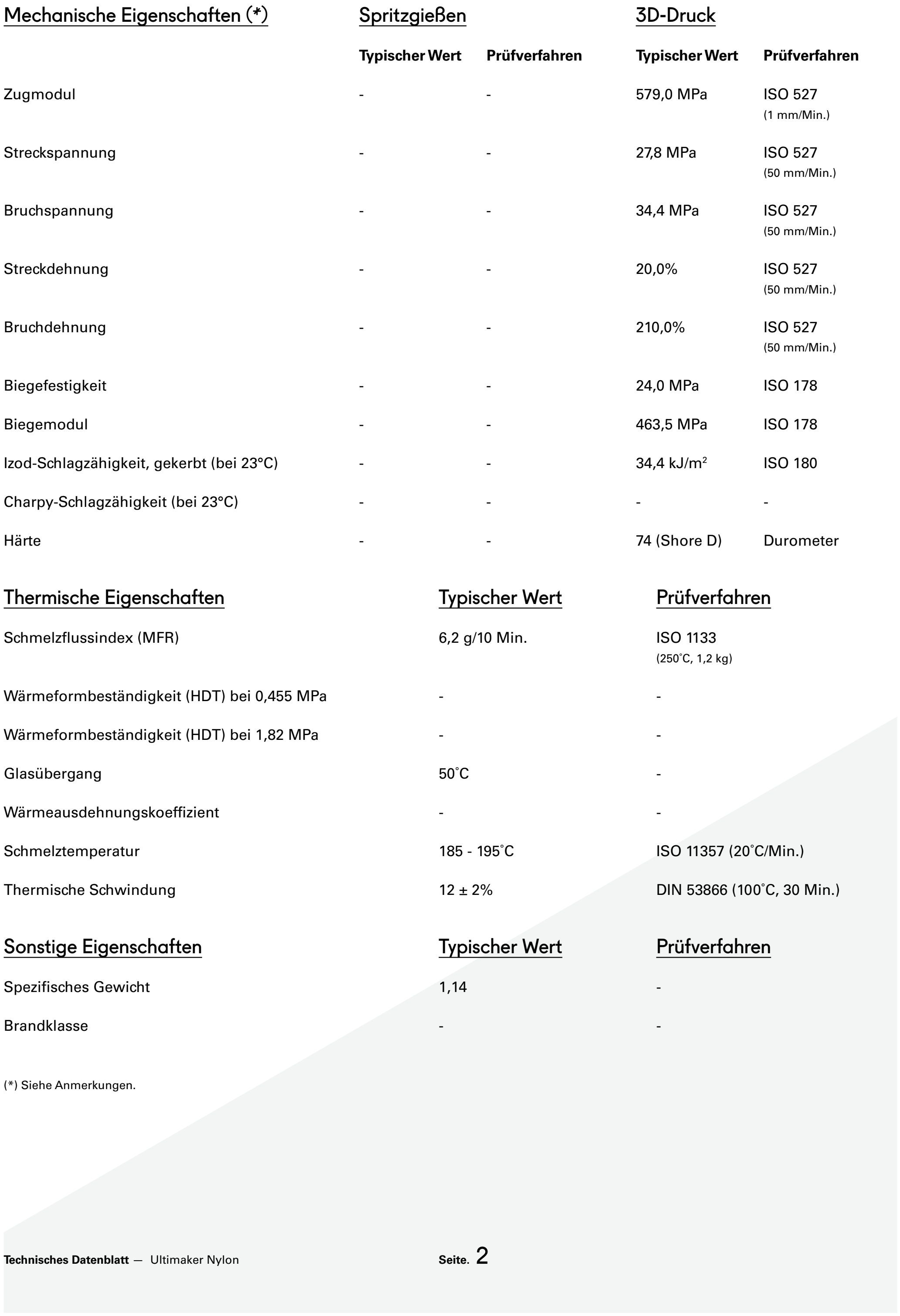

Mechanische Eigenschaften (*)	Spritzgießen		3D-Druck	
	Typischer Wert	**Prüfverfahren**	**Typischer Wert**	**Prüfverfahren**
Zugmodul	-	-	579,0 MPa	ISO 527 (1 mm/Min.)
Streckspannung	-	-	27,8 MPa	ISO 527 (50 mm/Min.)
Bruchspannung	-	-	34,4 MPa	ISO 527 (50 mm/Min.)
Streckdehnung	-	-	20,0%	ISO 527 (50 mm/Min.)
Bruchdehnung	-	-	210,0%	ISO 527 (50 mm/Min.)
Biegefestigkeit	-	-	24,0 MPa	ISO 178
Biegemodul	-	-	463,5 MPa	ISO 178
Izod-Schlagzähigkeit, gekerbt (bei 23°C)	-	-	34,4 kJ/m^2	ISO 180
Charpy-Schlagzähigkeit (bei 23°C)	-	-	-	-
Härte	-	-	74 (Shore D)	Durometer

Thermische Eigenschaften	Typischer Wert	Prüfverfahren
Schmelzflussindex (MFR)	6,2 g/10 Min.	ISO 1133 (250˚C, 1,2 kg)
Wärmeformbeständigkeit (HDT) bei 0,455 MPa	-	-
Wärmeformbeständigkeit (HDT) bei 1,82 MPa	-	-
Glasübergang	50˚C	-
Wärmeausdehnungskoeffizient	-	-
Schmelztemperatur	185 - 195˚C	ISO 11357 (20˚C/Min.)
Thermische Schwindung	12 ± 2%	DIN 53866 (100˚C, 30 Min.)

Sonstige Eigenschaften	Typischer Wert	Prüfverfahren
Spezifisches Gewicht	1,14	-
Brandklasse	-	-

(*) Siehe Anmerkungen.

Technisches Datenblatt — Ultimaker Nylon **Seite.** 2

III Data sheet of Ti-6Al-4V

Table 28: Data sheet of Ti-6Al-4V. Reproduced from [29].

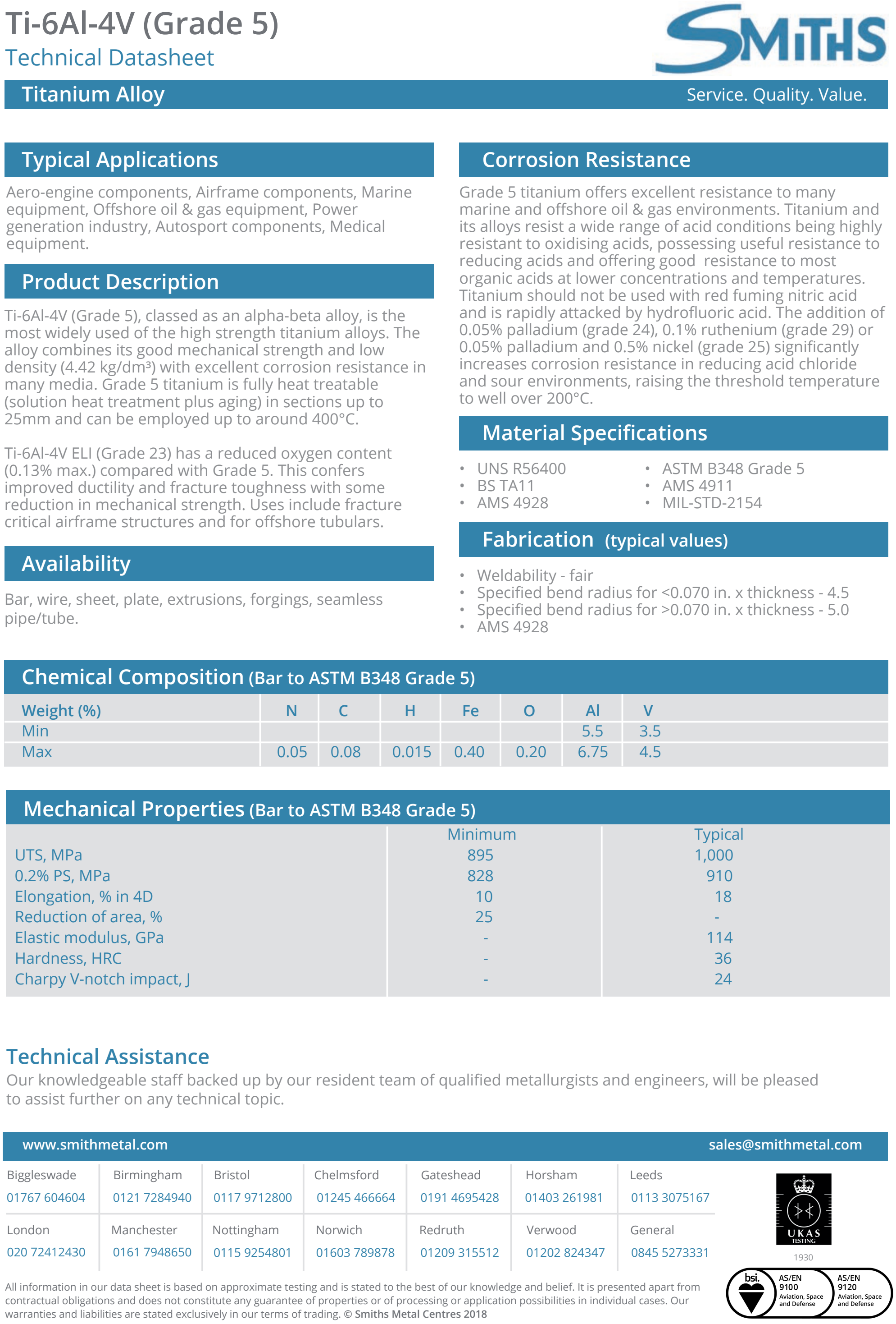

Ti-6Al-4V (Grade 5)

Technical Datasheet

SMITHS

Titanium Alloy Service. Quality. Value.

Typical Applications

Aero-engine components, Airframe components, Marine equipment, Offshore oil & gas equipment, Power generation industry, Autosport components, Medical equipment.

Product Description

Ti-6Al-4V (Grade 5), classed as an alpha-beta alloy, is the most widely used of the high strength titanium alloys. The alloy combines its good mechanical strength and low density (4.42 kg/dm³) with excellent corrosion resistance in many media. Grade 5 titanium is fully heat treatable (solution heat treatment plus aging) in sections up to 25mm and can be employed up to around 400°C.

Ti-6Al-4V ELI (Grade 23) has a reduced oxygen content (0.13% max.) compared with Grade 5. This confers improved ductility and fracture toughness with some reduction in mechanical strength. Uses include fracture critical airframe structures and for offshore tubulars.

Availability

Bar, wire, sheet, plate, extrusions, forgings, seamless pipe/tube.

Corrosion Resistance

Grade 5 titanium offers excellent resistance to many marine and offshore oil & gas environments. Titanium and its alloys resist a wide range of acid conditions being highly resistant to oxidising acids, possessing useful resistance to reducing acids and offering good resistance to most organic acids at lower concentrations and temperatures. Titanium should not be used with red fuming nitric acid and is rapidly attacked by hydrofluoric acid. The addition of 0.05% palladium (grade 24), 0.1% ruthenium (grade 29) or 0.05% palladium and 0.5% nickel (grade 25) significantly increases corrosion resistance in reducing acid chloride and sour environments, raising the threshold temperature to well over 200°C.

Material Specifications

- UNS R56400
- BS TA11
- AMS 4928
- ASTM B348 Grade 5
- AMS 4911
- MIL-STD-2154

Fabrication (typical values)

- Weldability - fair
- Specified bend radius for <0.070 in. x thickness - 4.5
- Specified bend radius for >0.070 in. x thickness - 5.0
- AMS 4928

Chemical Composition (Bar to ASTM B348 Grade 5)

Weight (%)	N	C	H	Fe	O	Al	V
Min						5.5	3.5
Max	0.05	0.08	0.015	0.40	0.20	6.75	4.5

Mechanical Properties (Bar to ASTM B348 Grade 5)

	Minimum	Typical
UTS, MPa	895	1,000
0.2% PS, MPa	828	910
Elongation, % in 4D	10	18
Reduction of area, %	25	-
Elastic modulus, GPa	-	114
Hardness, HRC	-	36
Charpy V-notch impact, J	-	24

Technical Assistance

Our knowledgeable staff backed up by our resident team of qualified metallurgists and engineers, will be pleased to assist further on any technical topic.

www.smithmetal.com sales@smithmetal.com

Biggleswade	Birmingham	Bristol	Chelmsford	Gateshead	Horsham	Leeds
01767 604604	0121 7284940	0117 9712800	01245 466664	0191 4695428	01403 261981	0113 3075167
London	Manchester	Nottingham	Norwich	Redruth	Verwood	General
020 72412430	0161 7948650	0115 9254801	01603 789878	01209 315512	01202 824347	0845 5273331

UKAS TESTING 1930

bsi. AS/EN 9100 Aviation, Space and Defense AS/EN 9120 Aviation, Space and Defense

Appendix

I Force displacement curves CPO

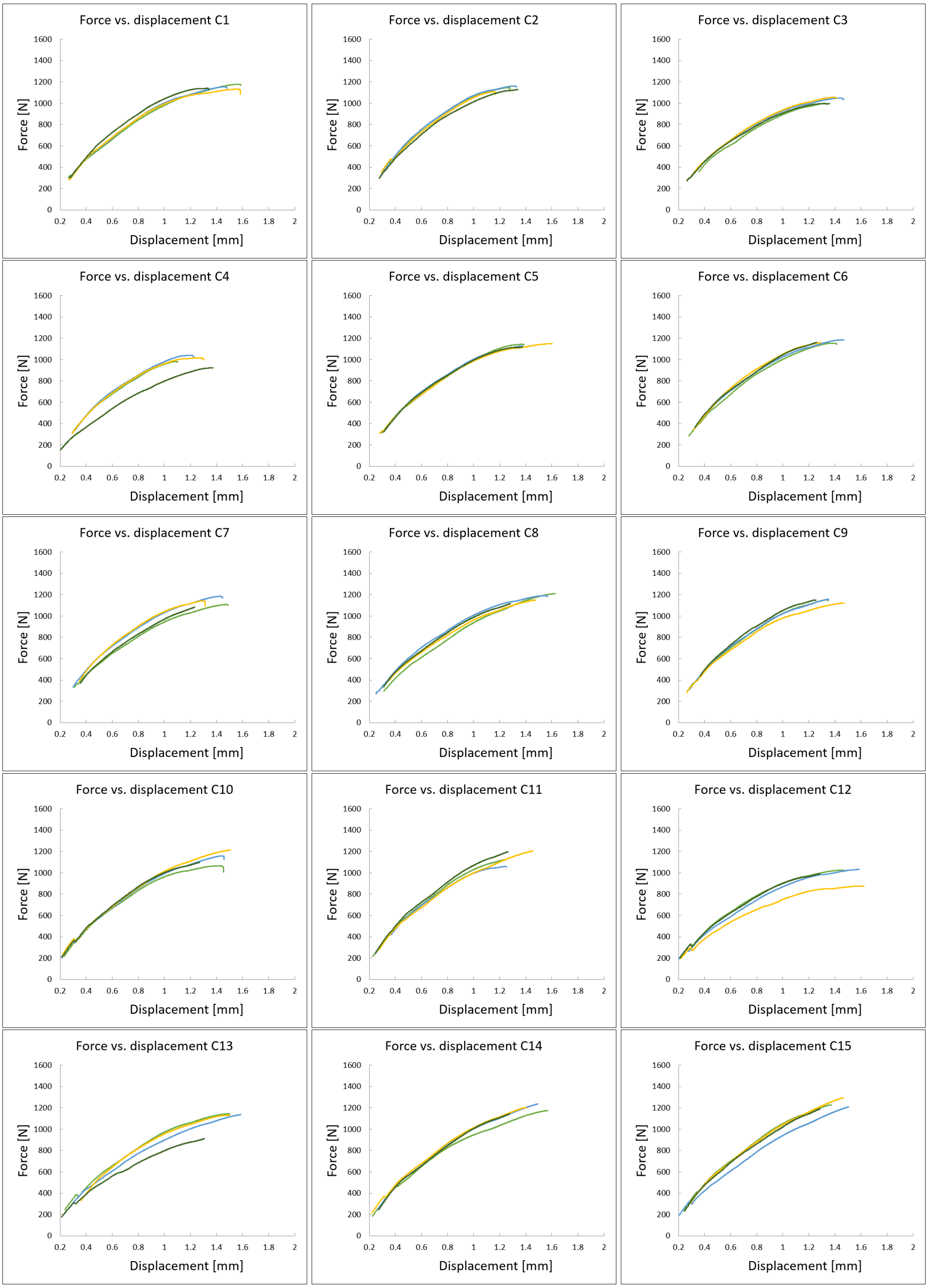

Figure 56: Force displacements curves of the CPO samples of conditions C1 to C15.

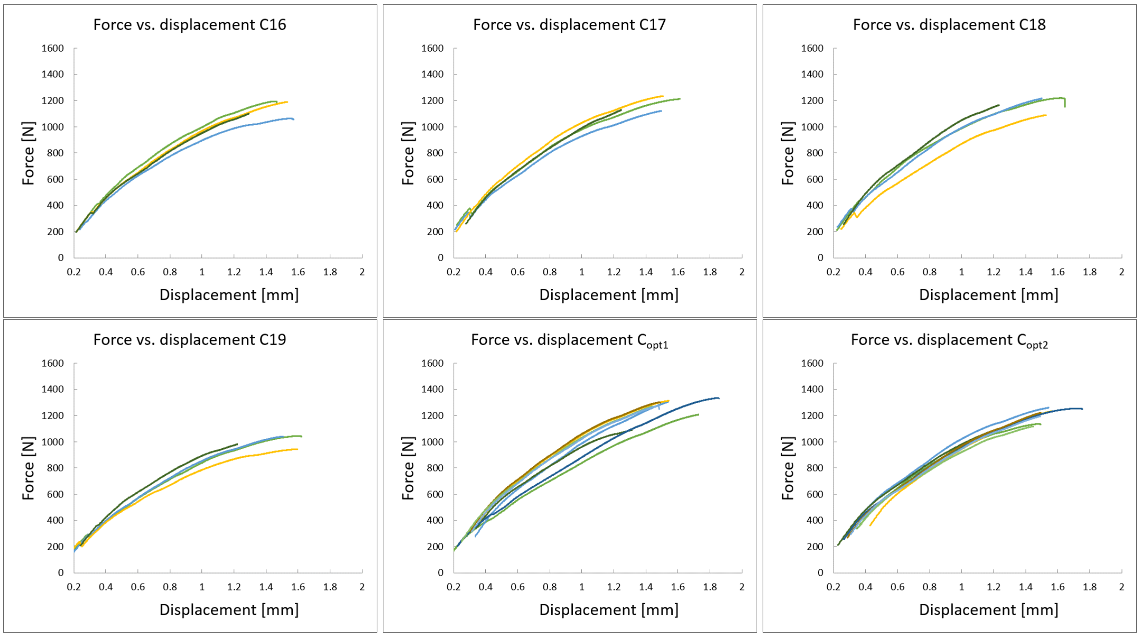

Figure 57: Force displacements curves of the CPO samples of conditions C16 to C19, C_{opt1} and C_{opt2}.